②

AD-A238 935

DTIC
ELECTE
JUL 2 1991
S   D
C

Final Report

MICRODESIGNING OF LIGHTWEIGHT/HIGH STRENGTH   #5

CERAMIC MATERIALS   Prepared for

I. A. Aksay, Principal Investigator   July 31, 1989

REPORT DOCUMENTATION PAGE

Form Approved
OMB No. 0704-0188

1a. REPORT SECURITY CLASSIFICATION	1b. RESTRICTIVE MARKINGS
Unclassified	

2a. SECURITY CLASSIFICATION AUTHORITY	3. DISTRIBUTION/AVAILABILITY OF REPORT
	Approved for public release;
2b. DECLASSIFICATION/DOWNGRADING SCHEDULE	Distribution unlimited

4. PERFORMING ORGANIZATION REPORT NUMBER(S)	5. MONITORING ORGANIZATION REPORT NUMBER(S)

6a. NAME OF PERFORMING ORGANIZATION	6b. OFFICE SYMBOL (If applicable)	7a. NAME OF MONITORING ORGANIZATION
University of Washington		AFOSR/NC

6c. ADDRESS (City, State, and ZIP Code)	7b. ADDRESS (City, State, and ZIP Code)
Seattle, WA 98195	Bldg. 410
	Bolling AFB, DC 20332-6448

8a. NAME OF FUNDING/SPONSORING ORGANIZATION	8b. OFFICE SYMBOL (If applicable)	9. PROCUREMENT INSTRUMENT IDENTIFICATION NUMBER
AFOSR	NC	Grant No. AFOSR-87-0114

8c. ADDRESS (City, State, and ZIP Code)	10. SOURCE OF FUNDING NUMBERS			
Bldg. 410	PROGRAM ELEMENT NO.	PROJECT NO.	TASK NO.	WORK UNIT ACCESSION NO.
Bolling AFB, DC 20332-6448	61102F	2303	A3	

11. TITLE (Include Security Classification)
Microdesigning of
Lightweight/High Strength Ceramics Materials

12. PERSONAL AUTHOR(S)
I. A. Aksay, G. C. Stangle, D. M. Dabbs, M. Sarikaya

13a. TYPE OF REPORT	13b. TIME COVERED	14. DATE OF REPORT (Year, Month, Day)	15. PAGE COUNT
Final	FROM 1/1/89 TO ___	July 31, 1989	145

16. SUPPLEMENTARY NOTATION

17. COSATI CODES			18. SUBJECT TERMS (Continue on reverse if necessary and identify by block number)
FIELD	GROUP	SUB-GROUP	Ceramics, Composite Materials, Colloidal Processing

19. ABSTRACT (Continue on reverse if necessary and identify by block number)

This interim report describes the results of research conducted under Grant No. AFOSR-87-0114, which deals primarily with the processing and characterization of complex ceramic matrix composite systems. Particular emphasis was placed on developing processing schemes for whisker-reinforced ceramic matrix composites. Additional studies are being conducted on boron carbide-aluminum ceramic/metal composites. Further, theoretical studies have been made to provide the foundation for developing a more fundamental understanding of colloidal systems.

91-04777

20. DISTRIBUTION/AVAILABILITY OF ABSTRACT	21. ABSTRACT SECURITY CLASSIFICATION
☐ UNCLASSIFIED/UNLIMITED ☒ SAME AS RPT ☒ DTIC USERS	Unclassified

22a. NAME OF RESPONSIBLE INDIVIDUAL	22b. TELEPHONE (Include Area Code)	22c. OFFICE SYMBOL
Donald R. Ulrich	(202) 767-4963	NC

DD Form 1473, JUN 86 Previous editions are obsolete. SECURITY CLASSIFICATION OF THIS PAGE

91 7 11 071

MICRODESIGNING OF LIGHTWEIGHT/HIGH STRENGTH CERAMIC MATERIALS

I. A. Aksay, Principal Investigator

July 31, 1989

Department of Materials Science and Engineering

Advanced Materials Technology Program, The Washington Techology Center

University of Washington

Seattle, Washington 98195

Accession For

BTIS GRA&I

BTIC TAB

Unannounced

Justification

By

Distribution/

Availability Codes

Dist   Avail and/or   Special

A-1   .7,

Contents

Contents

Preface

This is the fifth research progress and forecast report for the Air Force Office of Scientific Research (AFOSR) research grant No. AFOSR-87-0114, entitled *Microdesigning of Lightweight/ High Strength Ceramics Materials*. This report summarizes research accomplishments during the period 1 January 1989 to 30 June 1989.

This research program is concerned primarily with the processing and characterization of complex ceramic matrix composite systems. Emphasis is placed on developing processing schemes for whisker-reinforced ceramic matrix composites. Additional studies dealt with boron carbide-aluminum ceramic/metal composites. In each case, material purity and microstructural features can significantly affect the macroscopic properties of the material. Special techniques are being developed to allow for the efficient design of microstructural features during processing: this work comprises the first section of this report entitled "Fundamental Studies in Processing." This section deals with the colloidal dispersion, consolidation, and sintering of ceramic powders and ceramic-forming gels and polymers, in an effort to identify key processing parameters that affect the microstructure of the composite material. The second section describes experimental results in the fabrication, mechanical testing, and high resolution electron microscopy analysis of B_4C-Al composites, as well as two new classes of ceramic-based materials, so that the relationship between microstructure, composition and mechanical properties may be determined. The final section describes the results of the significant theoretical effort made in our group. Theoretical models of particle-particle interaction, particle-polymer interaction, and colloidal suspension stability have been developed, based upon statistical mechanics and interparticle potential analysis; results have been very encouraging and provide the foundation for developing a more fundamental understanding of colloidal systems in various situations. Microscopic and continuum mechanics modelling of mechanical behavior and fluid mechanics of ceramic suspensions and gels are being undertaken, and initial results are encouraging.

1. Fundamental Studies in Processing

This chapter is concerned with general processing studies. Each of the following topics seeks to address the difficulties encountered when advanced techniques of materials fabrication are used. Examples include the use of submicron powders to make highly dense materials, making suitable gels for coatings, monoliths, and fibers, and the manufacture of composites. Within the topics described below, a model system is usually defined and studied to determine the difficulties of the approach and to find the techniques to best counter these difficulties. The latter point implies that an understanding of the physics and chemistry is achieved within the area of interest, and this understanding is then transferred to real systems for better materials processing. Materials with controllable microstructures and properties result.

1.1. Charge Stabilization of Colloidal Particles

Investigators: J. Liu, M. Sarikaya, and W. Y. Shih

As reported in past reports on this project, it was observed that the microstructure of the particle reflects its size. However, the structures observed are counter to current models derived from thermodynamics. The goal in this project is to understand the mechanism of colloidal particle formation and to determine the factor controlling particle size. The approach used gold particles formed by reducing gold chloride with sodium citrate in water. The reduction process is halted at intermediate steps and the resultant suspensions examined by transmission electron microscopy (TEM). It was observed that the nuclei begin to aggregate early in the process, but then redisperse. This is a result of the charge density of the growing particle: initially the charge density is too low to prevent aggregation, but as the particles grow the charge is eventually sufficient to cause redispersion. Fusion of the aggregated particles is prevented by surfactant coating. The size of the final particles is determined by the balance of the total Coulombic energy of the system and the total surface tension. The minimization of the total

energy leads to our prediction that the particle size will depend on the concentration of gold and citrate in solution according to the formula: $R \sim [C_{gold}\backslash C_{citrate}]^{0.67}$ This is in excellent agreement with our experiments. With these results, a method has now been determined by which the particle size can be controlled within a precipitate/surfactant suspension.

1.2. The Mechanical Properties of Colloidal Gels

Investigators: W.-H. Shih, J. Liu, W. Y. Shih, and S. I. Kim

Past and present projects in this program have been and are using gels to form stable suspensions of colloidal particles. These gels can be used to make a variety of forms: tapes, fibers, coatings, and monoliths. However, not enough is known about the structure and properties of these types of gels. The objective in this portion of the project is to establish the structure-property relationship in colloidal gels so that the application of these materials can be optimized. The procedure used couples in-situ measurements on the evolution of a silica gel from the initial suspension with theoretical modelling efforts using Monte Carlo simulations of cluster-cluster aggregation. The model has been enhanced to permit restructuring to occur within the aggregation. As shown previously, the concentration of particles near a hard wall is proportional to the pressure exerted by the network. A scaling theory was developed to account for the self-similar nature of the aggregates. The average cluster size is related to the overall concentration of particles. The physical properties are related to the concentration in a power law fashion in the regime where the scaling behavior applies; however, self-similarity is destroyed by shear or compression and the properties are then dependent on an exponential restructuring process. Experimental studies revealed that the gels undergo a "crossover" during formation from a strong-link regime to a weak-link regime as the concentration of the particles is varied; this was predicted by the scaling model. It was also observed that the scaling model does fail when the gel is subjected to shear. When physically deformed by shear or compression, the gel exhibits the exponential behavior characteristic of network restructuring. Finally, it was found that the fractal dimension deduced from the rheological data was in good agreement with the results from quasi-elastic light scattering (QELS), corroborating the modelling studies.

1.3. Synthesis of Silicon Nitride Whisker-Reinforced Mullite Matrix Composites

Investigators: S. Sundaresan, S. Kanzaki, and S. I. Kim

In this project, the goal is to form a fully dense whisker reinforced ceramic matrix composite. Mullite matrices were used because of past experience within this group and success with the processing of mullite monoliths from powder and from gel. Silicon nitride as a whisker material was chosen because (i) the thermal expansion coefficient is close to that of mullite, minimizing thermal mismatch and (ii) the chemical compatibility of the two materials serves to minimize the reaction between the two during high temperature processing. The processing technique involves the pressure casting of a stable colloidal suspension consisting of the silicon nitride whiskers, colloidal silica, and colloidal boehmite (aluminum monohydroxide). The suspension was partially gelled to prevent whisker settling and then pressure cast. In this technique, silica coats the surface of the whiskers; as has been noted by other group members, the presence of silica during sintering aids in the densification of the matrix. Also, the silica coating will improve the stability of the whisker in the initial gel. Two suspensions of 5 and 10 percent by volume whiskers were prepared, filtered under pressure, and then sintered in air under ambient pressure. Between 1200° and 1300°C, only 85% of the theoretical density could be achieved. Microscopic examination revealed the presence of voids apparently caused by bubble entrapment in the gel. Currently, studies to reduce the amount of these bubbles and develop the optimal heat treatment for producing the composite are underway; hot pressing will be used in addition to pressureless sintering. It is anticipated that this composite will be a successful ceramic-ceramic composite and will be stable at high temperatures.

1.4. Smooth Surface Magnesium Oxide Substrates

Investigators: H. Nakagawa and M. Yasrebi

Magnesium oxide substrates are useful in optical and electronic applications. In our group, substrates have been used to support thin film superconducting ceramics. More generally, the interest in MgO lies in the fact that it hydrates very easily; this single fact has limited the use of MgO materials because of the types of liquids that can be used as suspending medium in the initial powder suspension: all are organic and all are restricted by stringent safety consid-

erations. Methods were developed whereby MgO materials can be made using water as the suspending medium. The approach was quite simple and was based on previous work in this group on α-alumina, barium titanate, and zirconia: first, the powder particles were coated with an organic surfactant (poly(methacrylic acid), PMAA) and then the particles were dispersed in water. It was found that the PMAA sufficiently slows the hydration of the MgO powder to allow casting. However, the suspension is sensitive to aging; this requires that the suspension be used almost immediately. The goal is to find a surfactant which will slow the hydration rate of MgO to the extent that aging becomes an insignificant factor in the processing of these materials. It is anticipated that this technique is generally applicable to other ceramic systems; other projects within this group are now using the same approach to simplify materials processing. In addition to the aqueous systems, tape casting of MgO suspensions in MEK with oxidized fish oil and poly(vinylbutyral) as processing aids has been done. Sintered densities were about 98% of theoretical; these materials were principally used as substrates for superconducting oxides.

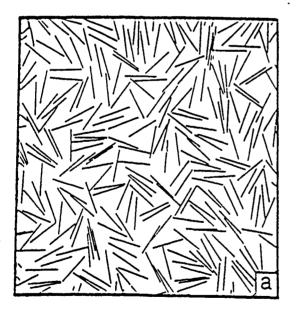## 1.5. Phase Separation and Ordering in Systems of Macroscopic Rod-like Particles

Investigator: L. A. Chick

High concentrations of whiskers or short fibers are required to achieve desired mechanical properties in some composite materials. Previous empirical studies have shown that the maximum attainable concentration of short fibers is inversely proportional to the aspect ratio of the fibers. Comparison to a geometrically-based theory, however, reveals that fibers pack more densely than would be expected for random distributions. It is the contention of this group that the higher-than-expected packing fractions are attributable to partial alignment of the fibers. Alignment and clustering are demonstrated in a two-dimensional model system of chopped graphite fibers which are excited by the application of sonic waves. The packing behavior of these fibers is compared to the liquid crystal phase transitions of rod-like polymer molecules which exhibit spontaneous alignment to achieve a thermodynamic equilibrium state. (See also Fig. 1.) The model of Flory and Ronca[1] was applied to predict the formation of ordered domains in monolayers of the rod-like particles. A preliminary phase diagram was also constructed. A higher degree of orientation would lead to an improved ceramics fabrication process by allowing higher fiber packing fraction and a greater degree of anisotropy to be achieved.

References

1. P. J. Flory and G. Ronca, *Melec. Cryst. and Liquid Cryst.*, **54**, 289 (1979).
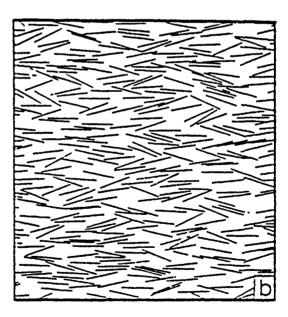
Figure 1. Computer-generated rod configurations for an axial ratio of 25: a) Randomly oriented phase at maximum (equilibrium) rod concentration (area fraction of 0.158). b) Normally distributed aligned phase in equilibrium with the random phase (area fraction of 0.192; standard deviation of 12.5°).

2. Designing, Processing, and Characterizing B₄C-Al Cermets and High Temperature Cermet Systems

The primary focus of the research on ceramic-metal ("cermet") materials has been the processing and the microstructural and mechanical property characterization of B_4C-Al composites. The objective of the first portion of this work has been to study the effect of controlled modifications in the microstructure upon the elastic and fracture properties of the B_4C-Al cermet. Special emphasis has been given to the response of the tailored microstructure to static and dynamic loading (in collaboration with Los Alamos National Laboratory). The goal of this second portion of the work has been to use high resolution TEM imaging techniques to correlate the structure, the composition, and the mechanical properties of the phases and interphases in the B-C-Al ternary system. During the current period, two new projects have been initiated. The first of these is the fabrication of B_4C-Al/Al laminates, where the objective is to increase cermet mechanical properties using the mechanical advantages of these types of microstructures. The second project is the design and preliminary processing of high temperature (> 1000°C) cermets. In this case, the objective is to develop a fully dense cermet (between a metal and a ceramic phase, each of which is known to have high temperature stability) which would have adequate strength (> 500 MPa) and toughness (> 15 MPa-M$^{1/2}$). In addition to these projects, previously initiated ceramic/polymer (cerpoly) material processing studies have significantly progressed. In the following sections, the progress of the last six months is described.

2.1. Processing and Heat Treatment of B₄C-Al Composites for Static and Dynamic Properties

Investigators: D. L. Milius and G. H. Kim

The objectives of this research are to determine the effects of microstructural features, interface, and metallic phase on the static and dynamic mechanical properties of boron carbide-aluminum composites. Previous research has resulted in the establishment of the processing

variables that yield controlled microstructures of the cermet where both phases form t ree-dimensional continuous networks.[1-3] Static fracture toughness (> 10 MPa-m$^{1/2}$) and .acture strength (> 620 MPa) can now be routinely achieved in samples which contain Al up to 35 vol. %. The advantages of the B$_4$C-Al system are its low density (~ 2.7 g/cc) and high hardness (> 2000 KHN), which can be further improved by the modification in the microstructure and the metal phase. These advantages form the basis for the potential application of B$_4$C-Al cermets in the armor/antiarmor field. Within this current period, microstructural modifications have been developed to further improve mechanical properties beyond those achieved by using the well established processing technique and to make correlations between microstructural variables and mechanical properties so a full control of the potential use of B$_4$C-Al cermets can be realized. Microstructural parameters under study include: (i) contiguity, continuity, and volume fraction of constitutent phases; (ii) ceramic/metal interface characteristics (second phases and segregation); (iii) laminated B$_4$C-Al/Al structures; and (iv) characteristics of the metal (Al) phase. Studies on parameters (i) through (iii) have been reported earlier or elsewhere in this report. Within the current period, emphasis was given to designing microstructures and avoiding the formation of deleterious ceramic reaction products. During the next half-year portion of this project, it is planned to measure properties and establish the correlation with the microstructural variables. Since characteristics of the metallic phase can be modified by heat treatment (such as aging) and alloying, this will constitute one of the future studies in this important area.

References

1. D. C. Halverson, A. J. Pyzik, and I. A. Aksay, "Processing and Microstructural Characterization of B$_4$C-Al Cermets," *Ceram. Eng. Sci. Proc.*, **6**, *7-8*, 736-744 (1985).

2. A. J. Pyzik, I. A. Aksay, and M. Sarikaya, "Microdesigning of Ceramic-Metal Composites," in *Ceramic Microstructures, '86* edited by J. A. Pask and A. G. Evans, pp. 45-54 (Plenum, New York, 1988).

3. D. C. Halverson, A. J. Pyzik, and I. A. Aksay, "Processing B$_4$C-Al Composites," *J. Am. Ceram.*, **72**, *5*, 775-780 (1989).

2.2. Properties and Characterization of Ceramic-Metal Interfaces

Investigator: G. H. Kim

The objective of this work is to understand the role of ceramic-metal interfaces for the improvement of strength and toughness.[1,2] The properties of B_4C-Al composites were measured after introducing a thin amorphous layer on the surface of the sintered B_4C by gas-phase reaction. Properties were correlated to different interfacial layer thicknesses and interfacial phase structure. Characterization of the oxidized sample indicated the existence of oxidized B_4C/B_4C grain boundaries resulting in intergranular cracking. A reaction between the B_4C and Al phases seemed to cause the depletion of the oxidized amorphous layer after infiltration. During the cooling of aluminum, additional cracking took place on the weakly oxidized layer along the grain boundaries. Characterization of the nitrided sample indicated no evidence of grain boundary attack by the nitrided layer. Microcracks were not observed even after six hours of nitridization. Crystallization of this amorphous phase was attempted at half the decomposition temperature of BN. Very fine crystallites in the amorphous matrix were observed and determined to be $(BN)_{0.26}C_{0.74}$ by electron diffraction and electron energy loss spectroscopy techniques. Since interfaces with the amorphous layer are expected to have lower strength and incomplete infiltration of the Al phase, additional studies are required to determine the effect of hardness of the metallic phase on impact resistance of ceramic-metal composites.

References

1. *Interfaces in Metal-Matrix Composites*, A. G. Metcalfe (ed.) Vol. 1, Academic Press (1971).

2. "Guide to Selecting Eng. Materials," *Adv. Mater. and Processing* Vol. 4, No. 1, ASM International (1989).

2.3. Fabrication of Ceramic-Metal Laminated Composites Using Tape Casting

Investigators: M. Yasrebi, R. S. Parikh, and J. E. Webb

A processing methodology was developed for the fabrication of ceramic-metal composites using tape casting. Such lamination techniques offer a unique opportunity to achieve a high

degree of control over the microstructure, and thus to study microstrucure-property relationships. Flat tapes of B_4C were produced using an emulsion-based binder system and partially sintering the tapes. The tapes were stacked with alternate layers of Al foil in order to obtain a laminated structure. Al was infiltrated into the porous B_4C tapes. The microstructure was examined and tested for mechanical strength and toughness. Limited past work with laminated structures of ceramic-metal composite materials has demonstrated enhancement of mechanical properties. Moreover, the present approach can eliminate difficulty in processing thick samples due to sluggish infiltration kinetics. B_4C tapes that were 74% dense and 80 μm thick were laminated with 50 μm thick Al alloy of 1100. The result is a composite of 80 μm thick B_4C and 30 mm thick Al. Mechanical testing showed strength of average 400 MPa and toughness of average 9.2 $(MPa\text{-}m^{1/2})$. The results obtained so far indicate the feasibility of the technique. (See Fig. 2.) However, the thickness of Al and B_4C need to be optimized for best results.
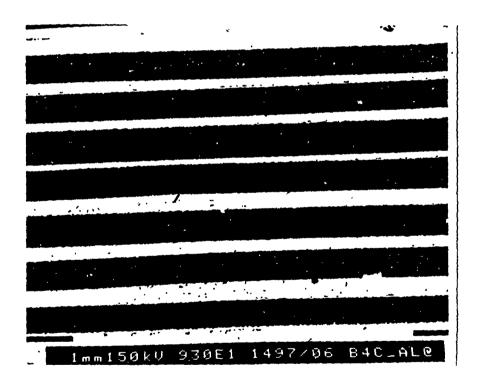

Figure 2. Optical micrograph of a B_4C-Al laminate.

2.4. Development of High Temperature (> 1000°C) Cermets

Investigator: D. L. Milius

The objective of this project is to develop a cermet system that would be used for structural application having a good combination of mechanical properties at temperatures above 1000°C and meet requirements of fracture toughness (> 15 MPa-M$^{1/2}$) and fracture strength (> 500 MPa). There are composites, in the monolithic and composite form, which satisfy only one of the above requirements.[1] What is needed is a processing methodology for a cermet material which fulfills both requirements in addition to being easily processed. The research steps involved in the project include the (i) design, (ii) processing, (iii) high temperature mechanical testing, and (iv) microstructural characterization.

Within this period of the project, several ceramic and metallic systems have been used to process cermets. The ceramics included SiC, mullite and B_4C, and the metallic alloys included Ni-based and Co-based superalloys.[2] Major problems encountered have included (i) difficulty in processing fully dense materials and (ii) excessive reaction products. In order to understand the compatibility of the metallic and ceramic systems, wetting experiments are underway which would lead to control of reaction products. Both HIPing and hot isostatic pressing are being used to achieve higher densities and to reduce reaction times.

References

1. (i) *Ceramics for High Performance Application,* edited by J. J. Burke, A. E. Gorun, and R. N. Katz, (Brook Hill Publ. Co., 1974); (ii) *Ceramics for High Performance Applications,* edited by J. J. Burke, E. N. Lenoe, and R. N. Katz (Brook Hill Publ. Co., 1978).

2. "Guide to Selecting Eng. Materials," *Adv. Mater. and Processing,* 4, 1 ASM International (1989).

2.5. Fabrication of Ceramic/Polymer Composites

Investigator: G. C. Stangle

The objective of this project is to fabricate a new class of materials that consist of ceramic powder (at > 50 v/o) and a high-temperature (> 350°C) polymeric material. The resulting

composite should be lightweight, tough and have uses at elevated temperatures. Laminated structures were prepared by (i) producing partially sintered ceramic tapes and polymeric tapes, (ii) making an alternating stack of the two tapes, and (iii) applying heat and/or pressure to cause adhesion of the layers with one another and to achieve infiltration of the porous ceramic layer with the polymeric material. Techniques have been successfully developed for preparing these B_4C ($\geq$ 2.5 μm) and polymer ($\geq$ 30 μm) tapes. Systematic lamination studies are currently in progress, focusing on the following key parameters: tape thicknesses, polymer type, thermal history and applied pressure during heating. Preliminary results indicate that a narrow processing temperature range (at $\sim$ 500°C) is available: temperatures must be high enough so that softening of the polymer for infiltration of the ceramic tape may occur, but low enough that a significant amount of polymer degradation does not occur. These materials may compete favorably for practical end uses with ceramic/metal composites, filled polymer composites and possibly some ceramic materials, with respect to hardness, low density, toughness, and upper use temperatures.

3 Theoretical Studies

The goal of the theoretical studies is to provide a fundamental understanding of various phenomena that occur in the various stages of colloidal processing, namely, dispersion, consolidation, and sintering, and as a result, to help design better procedures to process ceramic materials to meet specific needs. During the past few years, the theoretical program has grown significantly. Studies have been extended from monodisperse to bimodal systems, from equilibrium calculations to nonequilibrium ones, from electrostatically stabilized systems to sterically stabilized ones, from bulk properties to interfaces. Process modelling studies are also included. The results of the reporting period described here continue this trend of increasing our understanding of the colloidal processing of ceramics. Each project is summarized briefly in the following paragraphs.

3.1. The Size and Size Distribution of Colloidally Grown Nanometer-Sized Particles

Investigators: W. Y. Shih, J. Liu, and W.-H. Shih

Colloidally grown gold particles can be very small (0 ~ 100Å in diameter) and uniform in size. Understanding the controlling mechanism of size and size distribution of colloidally grown gold particles can therefore help in designing better processing routes for growing fine and uniform-sized ceramic powders. In this work, the size and the size distribution of colloidally grown gold particles were predicted using a statistical mechanics simulation method. The total interfacial energy was taken to be a function of the mean particle radius, a, and the standard deviation, σ, of the particle size distribution. The total interfacial energy was then minimized with respect to a and σ. The mean particle radius a was calculated to be proportional to $(V_g / N_c)^{2/3}$, where V_g is the volume concentration of gold and N_c is the number concentration of citrate, in agreement with experiments. The normalized standard deviation, $\bar{\sigma} \equiv (\sigma / a)$ was found to be about 15% for any symmetric distribution, again, in agreement with experiments.

The effect of citrate is very much like a charged surfactant since it will adsorb on the particle surface and give rise to the surface charge on the particles. Therefore, these calculations suggest that in the growth of ceramic particles, one may include a charged surfactant in the solution to produce fine and uniform-sized ceramic particles.

3.2. Polymer Adsorption: Energy Dependence of the Adsorbed Layer Thickness

Investigators: W. Y. Shih and W.-H. Shih

Polymers and polyelectrolytes are increasingly used in ceramic processing. Very often the polymers and the polyelectrolytes adsorb or the particle surface. The adsorption of the polymers and polyelectrolytes on the particle surface changes the suspension behavior, such as lowering the viscosity and so forth. It is important to know how the adsorption of polymers and polyelectrolytes changes with the suspension condition, such as the pH and salt concentration, which change the interaction between monomers as well as the interaction between monomers and the particle surface. Developing an understanding of the relationship between the thickness of the adsorbed layer change and monomer-monomer interaction as well as the monomer-wall interaction is the focus of this investigation. Monte Carlo simulations were used to study the adsorption behavior of polymers with a lattice model in which the polymer chains can (i) move as a whole, (ii) wiggle, and (iii) undergo reptation. The monomer-monomer interactions are considered up to the second-nearest-neighbor distance to mimic the screen Coulomb repulsion of polyelectrolytes at high salt concentrations. The monomer-wall interaction is taken up to the nearest-neighbor distance. At saturation, it was found that the farthest extension of the adsorbed layer H_m is independent of both the monomer-monomer interaction and monomer-wall interaction, which agrees with our experiments. It was also shown that, at saturation, adsorption amount, Γ, which is defined as the total amount adsorbed per unit area decreases (i) with increasing monomer-monomer repulsion and (ii) with decreasing monomer-wall attraction. Finally, the root-mean-square thickness, H, at saturation, is (i) independent of the monomer-monomer interaction, but (ii) increases with decreasing wall-monomer attraction.

This result implies that the onset of the forces between two adsorbed layers, which should take place at about $2H_m$, should be independent of pH since in the suspension both the monomer-monomer interaction and the monomer-wall interaction is controlled by pH, which is in agreement with the experiments. However, the adsorption amount Γ and the root-mean-square thickness H should change with pH, which also agrees with our experiments.

3.3. Interactions Between Two Polymer-Coated Surfaces

Investigators: R. Kikuchi and J. F. Aguilera-Granja

This is an extension of the work described in the previous section in that it moves the theoretical effort closer to a fundamental description of microscopic process taking place between two surface-modified colloidal particles. The statistical method of the CVM was used in order to study the different conformations of the polymers in between two plates, as well as the probability of bridging of the polymers as a function of the molecular weight. The calculation for the force between the two surfaces was done for different values of the van der Waals-type interaction. The results show that for the polydisperse polymer system there is a repulsion between the two surfaces for all the energy values (bigger than the critical value). Results indicate a different behavior than the mono-disperse calculation of the force obtained when the "SF" theory is used. The "SF" theory predicts attraction for the two plates. This should be compared with the results of de Gennes, who proved that in the mean field approximation the calculation gives an exact cancellation. These results enhance the understanding of the role that polymers play in modifying particle-particle interactions, leading to better control of the properties of the colloid particles covered by polymer layers.

3.4. Stability of a Binary Colloidal Suspension and its Effect on Colloidal Processing

Investigators: W. Y. Shih, W.-H. Shih, and J. Liu

With the increasing use of smaller particles in colloidal processing, the traditional Furnas model of packing may not be enough to predict the green density under various suspension conditions. The interaction between particles must be taken into account. In this work, the stability of the binary colloidal fluid phase was related to the green density in colloidal processing. In particular, the effect of the interparticle interactions on the stability of the colloidal fluid was studied. The stability of the binary colloidal fluid phase was studied by first constructing the colloidal crystal-fluid phase diagrams in the repulsive regime and then by clustering studies using Monte Carlo simulations in the attractive regime. The phase diagrams in the repulsive regime were constructed by comparing the free energy of the solid phases to that of the fluid phase. The free energies are calculated variationally using Gibbs-Bogolyubov inequality. In the repulsive regime, it was found that the freezing density has a maximum with respect to the number fraction X of the larger particles, which means that mixing enhances the stability

of the fluid phase. When the diameter ratio of the effective hard spheres is smaller than 0.7, the fluid phase is stable in most of the phase space except small regions near the pure cases. The maximum of the freezing density sharpens when the difference in the diameters of the two species is greater. In the attractive regime, the cluster size of the attractive species was shown to have a peak as the concentration of the second species is increased, which means that mixing reduces the stability of the fluid phase. Thus, the enhanced stability of the fluid phase in the repulsive regime implies that mixing will give improved (higher) green density in the repulsive regime. The clustering phenomenon in the attractive regime reduces the stability of the fluid phase and implies that mixing in the repulsive regime will reduce the green density.

3.5. Rheology of Concentrated Colloidal Suspensions

Investigator: G. C. Stangle

Colloidal processing of ceramics requires highly concentrated yet sufficiently fluid suspensions in order to facilitate fabrication of objects of complex, near-net-shape with high green density. The rheological behavior of concentrated colloidal suspensions depends on a complex array of interacting factors: volume fraction, particle size, interparticle interactions, etc. A simulation package was thus developed for the rheology of concentrated colloidal suspension, based upon molecular dynamics calculations. Especially important is the specific inclusion of many-body hydrodynamic and thermodynamic interactions. The Brownian Dynamics algorithm of Ermak and McCammon[1] was combined with the many-body mobility matrices of Mazur and van Saarloos[2] (and Jeffrey and Onishi[3]), using the Smoluchowski approach for obtaining both the stochastic and thermodynamic contributions to Brownian motion. Interparticle interactions were accounted for in customary ways (e.g., hard- or soft-sphere, DLVO, etc.). Macroscopic transport properties were calculated by standard statistical mechanics averaging schemes (see, e.g., Zwanzig,[4] Barnes, et al.[5]) The code has been written, entered and verified for a shear rate of 0.1 sec^{-1}, particle radius of 5 μm, and volume fractions of 42 vol %, 30 vol %, and 20 vol %. Comparison with published experimental data indicates that preliminary results are accurate to within 20% for shear viscosity values. Parameters important to suspension rheology will be elucidated independently by conducting parametric studies. During the next reporting period, experimental studies will be designed to verify predictions. Processing could then be improved.

References

1. D. L. Ermak and J. A. McCannon, "Brownian Dynamics with Hydrodynamic Interactions," *J. Chem. Phys.*, **69**, 1352-1360 (1978).

2. P. Mazur and W. van Saarloos, "Many-Sphere Hydrodynamic Interactions and Mobilities in a Suspension," *Physica*, **115A**, 21-57 (1982).

3. D. J. Jeffrey and Y. Onishi, "Calculation of the Resistance and Mobility Functions for Two Unequal Rigid Spheres in Low-Reynolds-Number Flow," *J. Fluid Mech.*, **139**, 261-290 (1984).

4. R. Zwanzig, "Time-Correlation Functions and Transport Coefficients in Statistical Mechanics," *Ann. Rev. Phys. Chem.*, **16**, 67-102 (1965).

5. II. A. Barnes, M. F. Edwards and L. V. Woodcock, "Applications of Computer Simulations to Dense Suspension Rheology," *Chem. Eng. Sci.*, **42**, 591-608 (1987).

3.6. Fractal Colloidal Aggregates with Finite Interparticle Interactions: Energy Dependence of the Fractal Dimensions

Investigators: J. Liu, M. Sarikaya, W. Y. Shih

The stucture of the colloidal aggregates affects the properties of the suspension such as the viscosity. It is important to know how the interparticle interaction energy controls the structure of the aggregates in order to contol the suspension properties. It was shown that the interaction between gold particles coated with a surfactant can be described by a modified DLVO theory, and that the adsorbed surfactant layer serves as a wall to keep gold particles separated. The adsorbed surfactant amount changes with the added surfactant concentration, resulting in different effective surface charges on the gold particles and hence different attraction energies at the closest separation, i.e., 15 Å. The observed different fractal dimensions at different surfactant concentration can be correlated with the attraction energy at 15 Å separation. When the attraction energy E at 15 Å separation is larger than $4\,k_BT$ where k_B is the Boltzmann constant and T is the temperature, the fractal dimension has a value 1.75 which is the result of the irreversible diffusion-limited-cluster-aggregation model (DLCA). When $E \leq$

4 k_BT, the fractal dimension D increases rapidly with decreasing E. The D-vs.-E cur ˄ (Fig. 3) resembles very much that of the computer simulations of a reversible aggregation of Shih, et al.,[1] suggesting that reversible aggregation in colloids can be represented by the model of Shih, et al.[1]

References

W. Y. Shih, R. Kikuchi, and I. A. Aksay, "Reversible-Growth Model: Cluster-Cluster Aggregation with Finite Binding Energies," *Phys. Rev. A*, 36 5015-5019 (1987).

3.7. Fiber Spinning Simulations

Investigator: G. C. Stangle

A ceramic fiber spinning process has been developed in this laboratory that allows a ceramic suspension or precursor salt solutions to be tranformed into a ceramic fiber. As many as seven processing variables must be controlled in this process, resulting in a time-consuming optimization process. (See Fig. 4.) Thus, a computer model was developed to simulate the fiber spinning process in order to help identify proper spinning conditions. Use was made of the appropriate forms of momentum, mass, and energy balance equations. Various constitutive models for spinning fluid were employed. Parametric study of important process variables were conducted. A systematic study was undertaken in which nearly 500 simulations were completed. Important synergistic phenomena between the viscoelastic properties of the spinning fluid, extrusion conditions, and drying conditions were elucidated, making clear the directions which the experimental study should take. That is: fibers should be dry spun, with $T_\infty \geq 75°C$, and $V_\infty \geq 10$ cm/sec (T_∞ is ambient temperature, and V_∞ is velocity of ambient relative to velocity of fiber). Such experimental studies are in progress.

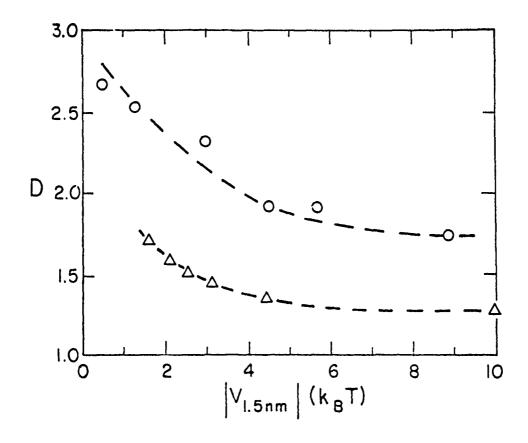Figure 3. Fractal dimension D versus $|V_{1.5\,nm}|$ for the gold aggregates (0) where $|V_{1.5\,nm}|$ is the magnitude of the attraction energy between gold particles at the average closest distance 1.5 nm. Also plotted is the D versus $\bar{E}$ (Δ) where E is nearest-neighbor attraction energy from the computer simulations of Shih, et al.[1] in two dimensions. Although the computer simulations of Ref. 1 were done in two dimensions, the resemblance of the two curves to each other is remarkable, suggesting that the reversible aggregation process in colloids can be represented by the model of Shih et al.
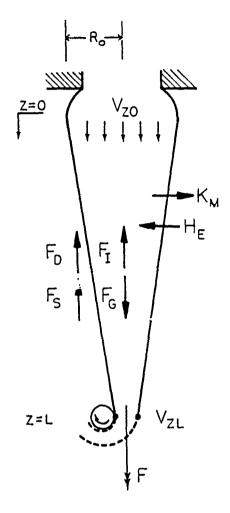
Figure 4. Schematic representation of the fiber spinning process. The local fiber radius, R, local velocity, V_z, are noted. Also included in the model are the forces acting on the fiber (inertial or viscous, F_I, drag, F_D, surface tension, F_S, and gravitational, F_G), and the heat and mass transfer processes occuring during this dynamic process.

3 Theoretical Studies

4. Personnel

I. A. Aksay, Professor
S. Kanzaki, Visiting Scientist
R. Kikuchi, Research Professor
II. Nakagawa, Visiting Scientist
M. Sarikaya, Assistant Professor
S. Sundaresan, Visiting Professor
G. Tomandl, Visiting Professor

D. M. Dabbs, Research Manager
W. Y. Shih, Research Scientist
W.-II. Shih, Research Scientist
G. C. Stangle, Research Scientist
M. Yasrebi, Research Scientist

J. F. Aguilera-Granja, Research Associate
J. Javadpour, Research Associate
D. L. Milius, Research Engineer
R. S. Parikh, Research Associate

L. A. Chick, Research Assistant
G. II. Kim, Research Assistant
S. I. Kim, Research Assistant
J. Liu, Research Assistant
J. E. Webb, Research Assistant

5. Technical Communications

5.1 Publications

The following is a list of publications that either (i) appeared in print, (ii) were accepted for publication, (iii) were submitted for publication, or (iv) were prepared for publication, during the reporting period covered in this report.

Note: Publications belonging to categories (i) or (ii) are reproduced in full as appendices to this report; the appendix number (e.g., Appendix V) follows the citation below. The abstracts of those in categories (iii) and (iv) are given in Appendix XIII.

1. Kim. G. H., M. Sarikaya, D. L. Milius, and I. A. Aksay, "Microstructural and Fractographic Characteriza'.on of B_4C-Al Cermets Tested Under Dynamic and Static Loading," in *Proc. of 48th EMSA*, G. W. Bailey (ed.), San Francisco Press (1989). [Appendix I]

2. Shih, W. Y., W.-H. Shih, and I. A. Aksay, "The Stability of Binary Charged Colloidal Crystals," *J. Chem. Phys.*, **90**, 4506 (1989). [Appendix II]

3. Shih, W. Y., W.-H. Shih, and I. A. Aksay, "Monte Carlo Simulations of Adsorption of Di-Block Copolymers," in *Processing Science of Advanced Ceramics*, I. A. Aksay, G. L. McVay and D. R. Ulrich, eds., Materials Research Scoeity, Pittsburgh, PA (1989). [Appendix III]

4. Shih, W. Y., W.-H. Shih, and I. A. Aksay, "Density Profiles of Semi-Dilute Polymer Solutions Near a Hard Wall: Monte Carlo Simulation," in *Processing Science of*

Advanced Ceramics, I. A. Aksay, G. L. McVay and D. R. Ulrich, eds., M terials Research Society, Pittsburgh, PA (1989). [Appendix IV]

5. Aguilera-Granja, F., and R. Kikuchi, "New Simulation of Polymers on Surfaces," in *Processing Science of Advanced Ceramics,* I. A. Aksay, G. L. McVay and D. R. Ulrich, eds., Materials Research Society, Pittsburgh, PA (1989). [Appendix V]

6. Shih, W. Y., W.-H. Shih, and J. Liu, and I. A. Aksay, "Stability of a Binary Colloidal Suspension and Its Effect on a Colloidal Processing," in *Processing Science of Advanced Ceramics,* I. A. Aksay, G. L. McVay and D. R. Ulrich, eds., Materials Research Society, Pittsburgh, PA (1989). [Appendix VI]

7. J. Liu, W.-H. Shih, W. Y. Shih, S. I. Kim, M. Sarikaya, and I. A. Aksay, "Mechanical Properties of Colloidal Gels," in *Processing Science of Advanced Ceramics,* I. A. Aksay, G. L. McVay, and D. R. Ulrich, eds., Materials Research Society, Pittsburgh, PA (1989). [Appendix VII]

8. Stangle, G. C., D.-J. Rhee, and I. A. Aksay, "Removal of Processing Aids from Ceramic/Polymer Composites," in *Processing Science of Advanced Ceramics,* I. A. Aksay, G. L. McVay, and D. R. Ulrich, eds., Materials Research Society, Pittsburgh, PA (1989). [Appendix VIII]

9. Aksay, I. A. and G. C. Stangle, "Powder Processing -- Science and Technology," *Proc. Symp. on Fine Ceramics Arita '88,* pp. 41-55 (1989). [Appendix IX]

10. Aksay, I. A., G. C. Stangle, and M. Sarikaya, "Processing with Nanometer-Sized Colloids," *Proc. 2nd Intl. Conf. on Ceramic Powder Processing Science,* October 12-14, 1988, Berchtesgaden, Bavaria, FRG (1989). [Appendix X]

11. Chick, L. A., C. Viney, and I. A. Aksay, " Liquid Crystal-Like Phase Separation in Systems of Macroscopic Rods," in *Rigid Rod Polymers,* Materials Research Society, Pittsburgh, PA, (1989). [Appendix XI]

5. Technical Communications   23

12. Chick, L. A., C. Viney, and I. A. Aksay, "Phase Separation and Clustering in Systems of Rod-like Particles," in *Processing Science of Advanced Ceramics,* I. A. Aksay, G. L. McVay, and D. R. Ulrich, eds., Materials Research Society, Pittsburgh, PA (1989). [Appendix XII]

13. Laoui, T., M. Sarikaya, D. L. Milius, and I. A. Aksay, "Phase Identification in B-C-Al Ternary System," *J. Am. Ceram. Soc.* (to be submitted, 1989). [Appendix XIII-1]

14. Kim, G. H., M. Sarikaya, D. L. Milius, and I. A. Aksay, "Microstructural and Fractographic Characterization of B_4C-Al Cermets," *J. Am. Ceram. Soc.* (to be submitted, 1989). [Appendix XIII-2]

15. Pyzik, A. J. and I. A. Aksay, "Relations Between Microstructure and Some Mechanical Properties in the B_4C-Al Composites," in *Ultrastructure Processing of Ceramics,* D. Uhlman, D. R. Ulrich, eds., John Wiley (in preparation, 1989). [Appendix XIII-3]

16. Pyzik, A. J. and I. A. Aksay, "Microdesigning of B_4C/Al Cermets," (in preparation, 1989). [Appendix XIII-4]

17. Stangle, G. C. and I. A. Aksay, "Simulataneous Momentum, Heat and Mass Transfer with Chemical Reaction in a Disordered Porous Medium: Application to Binder Removal from a Ceramic Gree Body," *Chem. Eng. Sci.* (submitted, 1989). [Appendix XIII-5]

18. Stangle, G. C and I. A. Aksay, "Spinnability Criteria for Ceramic Precursor Fluids," *J. Am. Ceram. Soc.* (to be submitted, 1989). [Appendix XIII-6]

5. Technical Communications

APPENDIX I

MICROSTRUCTURAL AND FRACTOGRAPHIC CHARACTERIZATION OF B₄C-AL CERMETS TESTED UNDER DYNAMIC AND STATIC LOADING

Gyeung Ho Kim, Mehmet Sarikaya, D. L. Milius, and I. A. Aksay

Department of Materials Science and Engineering, and the Washington Technology Center, University of Washington, Seattle, WA 98195

Cermets are designed to optimize the mechanical properties of ceramics (hard and strong component) and metals (ductile and tough component) into one system. However, the processing of such systems is a problem in obtaining fully dense composite without deleterious reaction products. In the lightweight (2.65 g/cc) B_4C-Al cermet, many of the processing problems have been circumvented.[1] It is now possible to process fully dense B_4C-Al cermet with tailored microstructures and achieve unique combination of mechanical properties (fracture strength of over 600 MPa and fracture toughness of 12 MPa-m$^{1/2}$).[2] In this paper, microstructure and fractography of B_4C-Al cermets, tested under dynamic and static loading conditions, are described.

The cermet is prepared by infiltration of Al at 1150°C into partially sintered B_4C compact under vacuum to full density. Fracture surface replicas were prepared by using cellulose acetate and thin-film carbon deposition. Samples were observed with a Philips 300G at 100 kV. A typical microstructure of a statically loaded sample is shown in Figure 1 where microtwins are observed in B_4C region and dislocations are present in the Al region. The mechanical twins which develop in B_4C during deformation (Figure 2) form on $\{01\bar{1}1\}$ planes. Under this loading condition, the thickness of the twins is several tens of nanometers and have lengths extending up to several microns.

It is noted that there is a considerable increase in fracture toughness (30%) under dynamic loading. Both the bulk microstructures and fracture surfaces were studied to assess the effect of loading rate (Figure 3). Although no appreciable increase in the dislocation density was observed in Al, fine voids were observed in samples tested under dynamic conditions which form along the boundaries of twins (Figure 3b). Longer twins without microvoids were observed in statically loaded samples (Figure 3a). This indicates that the microcracks nucleated along the twins. This hypothesis is supported by the observation that transgranular fracture takes place in B_4C under static loading where cracks nucleate and grow at twin boundaries (Figure 3c). In the dynamic loading case, fast movement of stress wave does not allow nucleated cracks to grow to critical size. Instead, crack propagates along the grain boundaries of B_4C (Figure 3d). The latter is a more tortuous crack path, requiring more energy absorption during failure, and therefore, causing an increase in fracture toughness.

1. D. C. Halverson, A. J. Pyzik, and I. A. Aksay, *Cer. Eng. Soc. Proc.*, **6**, 736-744 (1985).
2. A. J. Pyzik, I. A. Aksay, and M. Sarikaya, in *Ceramic Microstructures, Role of Interfaces*, J. A. Pask and A. G. Evans (eds.), Univ. of California Press (1988).
3. This work was supported by AFOSR under grant No. AFOSR-87-0114.

Figure 1. (a) BF and (b) DF (TEM) image from a B$_4$C-Al sample

Figure 3. BF images from statically ((a) and (c)) and dynamically ((b) and (d)) loaded samples; thin foil ((a) and (b)) and replicas ((c) and (d)).
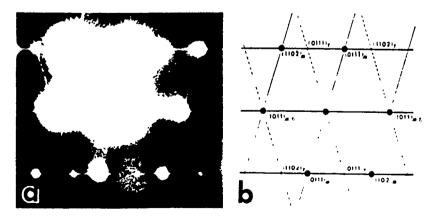
Figure 2. (a) SAD pattern and its analysis (b). Note the streaks due to {01$\bar{1}$1} twins.

APPENDIX II

The stability of binary charged colloidal crystals

Wan Y. Shih, Wei-Heng Shih, and Ilhan A. Aksay

Department of Materials Science and Engineering, and Advanced Materials Technology Program,
Washington Technology Center, University of Washington, FB-10, Seattle, Washington 98195

The stability of a binary disordered substitutional colloidal crystal has been examined against the formation of a colloidal liquid. Phase diagrams are constructed by comparing the free energy of the liquid phase to that of the solid phases. The calculations show that the freezing density has a maximum as a function of the number fraction. The maximum in the freezing density becomes more pronounced when the particle diameter ratio differs more from unity. If the particles have very different diameters, the binary colloidal crystals are unstable against the colloidal fluid. The freezing density rises almost vertically when the number fraction differs from 0 or 1 by less than 6%. The pronounced stability of the liquid phase for particles with more different sizes may explain the formation of colloidal glasses as opposed to the formation of disordered substitutional colloidal crystals with particles of more similar diameters. The Hume–Rothery rule for a binary metallic alloy also applies to a binary charged colloid if the diameter ratio is taken from the diameters of the effective hard spheres which are determined by the interparticle interactions but not those of the bare particles.

INTRODUCTION

Partly because of the practical importance of the study of colloidal systems to modern colloidal processing, and partly because of the availabi'' ·· of uniformly sized particles which make many studies possible, interest has increased in the study of colloidal systems. A charged colloidal system at low densities is very much like a liquid metal. The particles constitute the "ions" and the ions (including the counter ions dissolved from the particles and the stray ions in the solution) constitute the "electrons." The difference is, of course, that the size and the charge of a colloidal particle is about 1000 times larger than those of its atomic counterpart. Of particular interest are uniformly sized particles which can freeze into colloidal crystals when a high enough density is reached.[1] Face-centered-cubic (fcc) and body-centered-cubic (bcc) are the two stable crystalline structures.[2]

When particles of two different sizes are mixed together, the situation becomes more complicated because there are now two more parameters to change, namely, the particle diameter ratio and the number fraction. Experimentally, it is found that when the diameters of the two species are somewhat similar, one forms a homogeneous crystalline solid solution for all number fractions which is characterized both by a finite shear modulus and by Bragg diffraction, similar to a disordered substitutional alloy. The mixtures of polystyrene spheres of radii 545 and 445 Å are such examples.[1] The diameter ratio in these mixtures is about 0.817.

When the diameter ratio of the two species differs more from unity, one may form a colloidal glass or a crystalline colloidal compound depending on how long the system is allowed to reach equilibrium. For example, mixtures of polystyrene spheres[1,4] of radii 1100 and 545 Å have been found to form one homogeneous disordered solid (colloidal glass) characterized by a finite shear modulus but no Bragg diffraction when the number fraction is more than 5% from either end of the phase diagram; crystallinity is retained in the small regions (<5%) near the pure cases. Similar disordered colloidal solids can also be formed with larger colloidal particles. Liniger and Raj[5] reported that polystyrene spheres of 5 and 7 μ diameters formed disordered solids when the volume fraction of the 7μ particles is from 10% to 90% and ordered solids otherwise in an air-water interface. The diameter ratio for these mixtures is about 0.7. However, for particles in the micron size, the order–disorder transition cannot be studied with a further decreased diameter ratio because of differential settling.[5]

The formation of colloidal glasses was observed on a shorter time scale. If a colloidal mixture is allowed to equilibrate fully, a colloidal compound may be formed that has a complex crystalline structure similar to that of an intermetallic compound. For example, the above mentioned colloidal glasses formed with polystyrene particles of radii 1100 and 545 Å were reported to transform into colloidal compounds a year or so later.[3,4] Under suitable conditions, Hachisu and Yoshimura[6,7] were able to identify four different compound structures ($NaZn_{13}$, AlB_2, $CaCu_5$, and $MgCu_2$) with binary polystyrene spheres with individual particle diameters ranging from 2000 to 8000 Å. The exact crystalline structure depends on a number of parameters such as the particle diameter ratio, the number fraction, and the number densities. However, the equilibration of a colloidal mixture may take years, as mentioned in Refs. 3 and 4. Equilibrium is thus not always reachable within the laboratory time frame. Instead, what one often finds in a colloidal mixture may be only short-time phenomena and may be metastable. In light of this, we feel it is probably of more practical importance to discuss the "metastable" phenomena, i.e., the formation of a colloidal glass, than to discuss the stability of various colloidal compounds. Although the formation of various colloidal compounds at equilibrium is also interesting, we will not consider it in this paper.

For the atomic analog of a binary colloid, namely a bina-

ry metallic system, the Hume-Rothery rule[8] says that a substitutional alloy can not be formed when the diameters of the two atomic species differ more than 15%. Furthermore, the immiscibility of the two species in the crystalline form is usually accompanied by the formation of deep eutectics,[9] i.e., with fractional concentrations at which the liquid is stable to an especially low temperature. It is also known that the glass forming trend in metallic alloys is often related to deep eutectics.[10]

The purpose of this paper is to establish binary colloidal phase diagrams which show the "stability" regions of the colloidal substitutional alloys relative to the colloidal liquid. From the stability of the crystalline substitutional alloys, we can address the miscibility in binary colloidal crystals. By correlating with the deep eutectics in the phase diagrams, we will be able to address the question concerning colloidal glass forming. However, we must point out that the binary colloidal phase diagrams we establish in this paper may not be those at equilibrium since we do not consider the formation of various compounds. Nevertheless, the "metastable" phase diagrams we calculate here are still meaningful since in the laboratory time frame many of the colloidal systems are not at equilibrium.

The phase boundaries between the liquid and the disordered substitutional colloidal alloys will be constructed by directly comparing the free energies of the liquid to those of the solids (for which we have considered both fcc and bcc disordered substitutional alloys). The "stable" phase will be the one with the lowest free energy. In general, one should draw a common tangent in order to establish the two-phase regions in the phase diagrams. However, neither the experiment nor the theory is accurate enough to allow this procedure. The free energies of various phases are calculated by means of a variational principle based on the Gibbs-Bogolyubov inequality. Einstein oscillators are used as the reference system of the solid phases, and a binary hard sphere mixture is used as the reference system for the liquid. This approach has been successfully applied to calculate the phase diagrams of monodisperse charged colloidal particles.[2]

We now turn to the body of the paper. Section II briefly describes the formalism. Section III gives the results and discussions, while some concluding remarks are given in Sec. IV.

MODEL

We consider a binary aqueous suspension of N_1 particles of radius a_1, charge Z_1, and N_2 particles of radius a_2, charge Z_2 with volume Ω. In the absence of added electrolytes, there will be $N_1 Z_1 + N_2 Z_2$ counter ions (H_3O^+ or OH^- depending on the system) in solutions to neutralize the charges on the colloidal particles. If the number density of the colloidal particles is not too high or the temperature is not too low, the effective interactions between the colloidal particles can be adequately treated within the Debye–Hückel approximation. In MKSA units, the interaction takes the form

$$U(r_{ij}) = \frac{Z_i Z_j e^2}{4\pi\epsilon_0 \epsilon r_{ij}} \left[\frac{e^{qa_i}}{1+qa_i} \right] \left[\frac{e^{qa_j}}{1+qa_j} \right] e^{-qr}. \quad (2.1)$$

Here r_{ij} is the separation between the centers of particle i and particle j, ϵ is the static dieletric constant of water, ϵ_0 is the permittivity of free space, e is the electronic charge, and q is the inverse screening length which satisfies

$$q^2 = \frac{e^2}{\epsilon_0 \epsilon k_B T} \sum_i n_i(z_i^2), \quad (2.2)$$

where k_B is the Boltzmann constant, T is the absolute temperature, z_i and n_i are the charge and the number density of the ith species of ions, respectively. The term in the brackets of Eq. (2.1) is the size correction which takes into account the fact that part of the volume of the suspension is not available for screening due to the finite sizes of the colloidal particles. This correction is important in determining the melting behavior of the colloidal suspensions.[11]

When the colloidal suspension is at equilibrium, its thermodynamic properties are determined by the Helmholtz free energy $F = E - TS$, where E is the total energy and S is the entropy. For a system of particles interacting via the potential Eq. (2.1), the free energy per particle takes the following form:

$$F = \frac{1}{2N} \sum_{\substack{i,j \\ i \neq j}}^{N} \frac{Z_i Z_j e^2}{4\pi\epsilon_0 \epsilon} \left(\frac{e^{qa_i}}{1+qa_i} \right) \left(\frac{e^{qa_j}}{1+qa_j} \right)$$

$$\times \left\langle \frac{1}{|r_i - r_j|} e^{-q|r_i - r_j|} \right\rangle + E_{kin} - TS, \quad (2.3)$$

where E_{kin} and S are the kinetic energy and the entropy per particle, $N = N_1 + N_2$ is the total number of particles in the system, $\langle\ \rangle$ denotes the thermal average over the canonical ensemble, and r_i is the position of particle i. Equation (2.3) includes only the part of the free energy that depends on the arrangement of the particles. These are the terms that are relevant in determining the structure of the colloidal suspension.

The free energy can be obtained from Eq. (2.3) by the use of a variational principle based on the Gibbs-Bogolyubov inequality which states as follows:

$$F \leqslant F_0 + \langle U - U_0 \rangle_0 \equiv F', \quad (2.4)$$

where F_0 is the free energy of the reference system and $\langle U - U_0 \rangle$ is the potential energy difference of the system of interest and the reference system. Since F is upper bounded by F', we can then approximate F to be the minimum of F' with respect to the appropriate variables, that is, $F \simeq F'(x_0, y_0)$ and

$$\left. \frac{\partial F'(x,y)}{\partial x} \right|_{x = x_0} = 0 \text{ and } \left. \frac{\partial F'(x,y)}{\partial y} \right|_{y = y_0} = 0, \quad (2.5)$$

where x and y are the appropriate variables. In the present calculation, we use Einstein oscillators as the reference system for the solid and binary hard sphere fluid as the reference system for the liquid. This procedure has been successfully applied for the monodisperse colloidal suspensions and the intermetallic alloys.[12] It is expected to work well in the present case.

Solid

It is convenient to choose an ensemble of Einstein oscillators to define the reference system: each particle of type 1

or 2 oscillates about a lattice point independently in a potential well with a frequency ω_1 and ω_2. In terms of the Einstein temperature $\theta_i = \hbar\omega_i/k_B$ ($i = 1,2$) and with random alloy

approximation, we may write the right-hand side of Eq. (2.4) as

$$F = E_{kin} - TS + \frac{1}{2} \sum_{R \neq 0} \sum_{i,j=1}^{2} \frac{e^2}{4\pi\epsilon_0\epsilon} x_i Z_i x_j Z_j \left(\frac{e^{qa_i}}{1+qa_i}\right)\left(\frac{e^{qa_j}}{1+qa_j}\right) f_{ij}(|\mathbf{R}|)$$

$$- \frac{e^2 q}{8\pi\epsilon\epsilon_0}\left(x_1 Z_1^2 \frac{e^{2qa_1}}{(1+qa_1)^2} + x_2 Z_2^2 \frac{e^{2qa_2}}{(1+qa_2)^2}\right) - \frac{ne^2}{2\epsilon\epsilon_0 q^2}\left[x_1 Z_1\left(\frac{e^{qa_1}}{(1+qa_1)}\right) + x_2 Z_2\left(\frac{e^{qa_2}}{(1+qa_2)}\right)\right]^2 \quad (2.6)$$

in which $x_i = N_i/N$, for $i = 1,2$, R is the lattice vector, N/Ω is the number density of the colloidal particles, and

$$E_{kin} = \frac{3}{2} k_B T, \quad (2.7)$$

$$TS = 3k_B T \sum_{i=1}^{2} x_i [1 - \ln(\theta_i/T)], \quad (2.8)$$

and

$$f_{ij}(r) = \frac{1}{2r}e^{(W_i + W_j)q^2}\left[e^{-qr}\left(1 - \text{erf}\left[(W_i + W_j)^{1/2}q\right.\right.\right.$$

$$\left.\left. - \frac{r}{2(W_i + W_j)^{1/2}}\right]\right)$$

$$\left. - e^{qr}\left(1 - \text{erf}(W_i + W_j)^{1/2}q + \frac{r}{2(W_i + W_j)^{1/2}}\right)\right], \quad (2.9)$$

where erf is the error function

$$\text{erf}(x) = \frac{2}{(\pi)^{1/2}}\int_0^x e^{-y^2} dy, \quad (2.10)$$

and $6W_i$ is the mean square displacement which takes the following form:

$$W_i = \frac{\hbar^2 \coth(\theta_i/2T)}{4M_i k_B \theta_i} \quad i = 1,2, \quad (2.11)$$

in which M_i is the mass of the particles of type i. Note that the anharmonic effect has been taken into account in Eq. (2.9). The right-hand side of Eq. (2.6) may then be minimized with respect to θ_1 and θ_2 to give the upper bound of the structure-dependent part of the free energy of the colloidal substitutional alloys. In the actual calculations, $r/2(W_i + W_j)^{1/2} \pm (W_i + W_j)^{1/2}q$ is much larger than unity and Eq. (2.9) reduces to

$$f_{ij}(r) \simeq e^{(W_i + W_j)q^2}\frac{e^{-qr}}{r}. \quad (2.12)$$

Liquid

For the reference system of the liquid phase we consider a binary hard sphere fluid where particles are interacting via the hard sphere potential,

$$U_0(r_{ij}) = \begin{cases} \infty & r_{ij} < \sigma_{ij} \\ 0 & r_{ij} \geq \sigma_{ij} \end{cases} \quad (2.13)$$

in which $\sigma_{ij} = (\sigma_i + \sigma_j)/2$, where σ_i, the effective hard sphere diameter of particle i, is not, in general, equal to a_i,

the actual diameter of a type-i particle. With this choice of the hard-sphere mixture as the reference system, the right-hand side of Eq. (2.6) can be written as

$$F = F_{hs}(\sigma_1, \sigma_2, x_1) - \frac{e^2 q}{8\pi\epsilon\epsilon_0}\left(x_1 Z_1^2 \frac{e^{2qa_1}}{(1+qa_1)^2}\right.$$

$$\left. + x_2 Z_2^2 \frac{e^{2qa_2}}{(1+qa_2)^2}\right)$$

$$+ \frac{ne^2}{8\pi\epsilon\epsilon_0}\sum_{i,j=1}^{2}\int dr\, 4\pi r^2 \frac{e^{-qr}}{r}\left(\frac{e^{qa_i}}{1+qa_i}\right)$$

$$\times\left(\frac{e^{qa_j}}{1+qa_j}\right)[g_{ij}(r) - 1]\, x_i x_j Z_i Z_j, \quad (2.14)$$

where F_{hs} is the Helmholtz free energy of a hard-sphere mixture of diameter σ_1 and σ_2. The functions $g_{ij}(r)$ are the appropriate pair distribution functions for the reference systems, normalized to equal unity in the limit of large r. The terms involving $g_{ij}(r)$ can be evaluated analytically in the Percus–Yevick approximation for arbitrary ratios of the hard sphere diameters; explicit expressions of the terms involving $g_{ij}(r)$ have been given by Lebowitz.[13] These may be combined with the approximate analytic formulas given by Umar et al.[14] for the free energy $F_{hs}(\theta_1, \sigma_2, x_1)$ of the hard sphere mixture (based on the equation of state derived from the Percus–Yevick hard-sphere partition function) to give a close-form expression for the structure-dependent part of the right-hand side of Eq. (2.6). This part may then be minimized with respect to σ_1 and σ_2 to obtain the upper bound of the structure-dependent part of the free energy of the binary colloidal liquids

RESULTS AND DISCUSSIONS

To test our theory for a binary colloid, we first calculate the freezing densities for the colloidal mixtures that were reported experimentally in Refs. 3 and 4. The resulting freezing densities as a function of the number fraction of the large particles are plotted in Figs. 1(a) and 1(b) where D stands for the total number density of the colloidal mixture and $x = x_1 = N_1/(N_1 + N_2)$ stands for the number fraction of the large spheres. Figure 1(a) is for the case where $Z_1 = 300$, $a_1 = 545$ A and $Z_2 = 245$, $a_2 = 445$ A. Figure 1(b) is for the case where $Z_1 = 600$, $a_1 = 1100$ A and $Z_2 = 300$, $a_2 = 545$ A. These values were taken from Ref. 3. Figure 1(a) shows that the mixtures of 545 and 445 A particles form disordered substitutional fcc alloy at higher densities for all values of x.

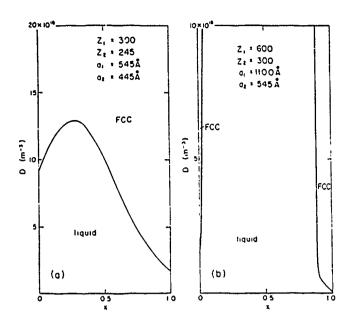FIG. 1. D–x phase diagrams of binary colloidal particles where D is the total number density and x is the number fraction of the large particles.

in qualitative agreement with the observation in Ref. 3. The actual diameter ratio is about 0.817 in these mixtures. However, the diameter ratio of the effective hard spheres is about 0.92. Note that there is a maximum in the freezing-density-vs-x curve indicating that the fluid phase can remain stable up to a higher density in the mixture than in the pure cases. We will show below that this maximum in the freezing density in the D–x plane actually corresponds to an azeotropic or a eutectic in the T–x phase diagram.

In Fig. 1(b), it is shown that mixtures of 1100 and 545 Å particles form no substitutional alloys in most of the phase space except for very small regions near $x = 0$ and $x = 1$ where the face-center-cubic (fcc) substitutional alloy is still stable. The small crystalline regions in Fig. 1(b) is in agreement with Ref. 3. The actual diameter ratio for these mixtures is about 0.5 while the diameter ratio of the effective hard spheres is about 0.75, both of which are smaller than those of the mixtures of Fig. 1(a).

The disappearance of the crystalline phase in Fig. 1(b) for an intermediate value of x up to very high densities signals a very pronounced maximum in the freezing densities as a function of x (or a very deep eutectic in the T–x phase diagram). Thus, the mixtures of 1100 and 545 Å particles should be more likely to form colloidal glasses than the mixtures of 545 and 445 Å particles. Indeed, this was the experimental observation.

To illustrate that a maximum in the freezing densities is equivalent to a minimum in the freezing temperature, we define an effective temperature $\tilde{T} = k_B T / (Z^2 e^2 / 4\pi \epsilon_{11} \epsilon a_1)$ where $Z = x_1 Z_1 + x_2 Z_2$ is the average charge and $a_1 = D^{-1/3}$ is the average nearest distance between particles. In Fig. 2 we plot the effective freezing temperature as a function of x for the mixtures of 545 and 445 Å particles in curve (a) and that for the mixtures of 1100 and 545 Å particles in curve (b). Curve (a) indeed shows a minimum in the effective freezing temperature which reflects the maximum
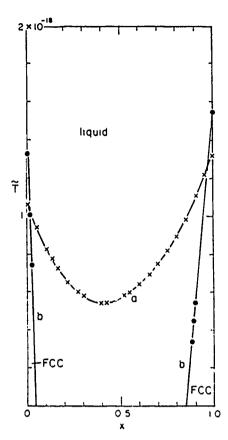

FIG. 2. $\tilde{T}$ – x phase diagrams of the binary colloidal particles in Fig. 1. $\tilde{T}$ is the effective temperature as defined in the text, and x is as in Fig. 1.

in the freezing density. In curve (b), again, the crystalline phase is unstable in most of the $\tilde{T} - x$ phase space except for small regions near $x = 0$ and $x = 1$ just as in the D–x phase diagram. The instability of the crystalline phase indicates a very deep minimum in the freezing temperature. In fact, the extrapolation of curve (b) shows that fluid mixtures are stable down to zero temperature for most values of x. Notice that the location of the minimum freezing temperature in Fig. 2(a), which is near $x = 0.4$, is not the same as that of the maximum freezing density in Fig. 1(a), which is near $x = 0.3$. The reason is that our $\tilde{T}$ is only approximate. If we were to use a different definition, such as $\tilde{T} = k_B T / E_{ave}$, where E_{ave} is the average energy per particle, we would have a more accurate representation of the effective temperature and hence a better agreement between Figs. 1(a) and 2(a) as to where the maximum freezing density and the minimum freezing temperature occur. Nonetheless, Figs. 1(a)–1(b) and Figs. 2(a)–2(b) show the correspondence between the freezing density and the effective freezing temperature. To relate the minima in the freezing temperatures that we have obtained to eutectics requires calculations of the miscibility at low temperatures (or high densities) for a eutectic is usually associated with not only an especially low melting point, but also with immiscibility in the solid phase. Shih and Stroud[15] have studied the miscibility of these colloidal mixtures in the liquid form and have shown that the mixtures do indeed phase separate at high densities. Phase separation begins at around $D = 13 \cdot 10^{18}$ m^{-3} for the mixtures of particles of 445 and 545 Å, which is near the maximum of the

freezing density in Fig. 1(a). For mixtures of particles of 545 and 1100 Å, phase separation begins at around $D = 1.6 \times 10^{18}$ m^{-3}, which is between the freezing densities of the pure cases. Although their predictions for phase separation are for liquid mixtures, the results are still appreciable when one considers phase separation between two solid phases (or between the solid and the liquid phases). The reason is that the excess free energy comes mostly from the mixing of the counter ions in the solutions because the ions outnumber the particles.[15] The structural part of the free energy is only a small portion of the total free energy. Thus, our maxima of the freezing densities (or minima in the freezing temperature) do relate to a eutectic, and the depth of the extrema does reflect the difficulty of mixing the particles. Comparing the diameter ratio for the mixtures of curves (a) and (b), one finds an analog of the Hume–Rothery rule in a binary colloid. However, one should note that the 15% difference in diameters for the miscibility margin relates more closely to the effective hard-sphere diameter ratio, which is 0.92 for curve (a) and 0.75 for curve (b), than to the actual particle diameter ratio, which is 0.817 for (a) and 0.5 for (b). This is reasonable since the atomic diameters used in the Hume–Rothery rule are also effective hard sphere diameters. Note that the interaction between these highly charged colloidal particles is repulsive and long ranged. Thus, what influences the interparticle arrangement would be the effective hard-sphere diameters which are determined by the range of the interparticle interactions but not by the actual particle diameters. This point may also be seen when one considers the low densities (typically a few volume per cent) of these colloidal crystals where the average nearest particle distance is about four or five times the actual particle diameters.

To illustrate this point more clearly, we plot the freezing densities of mixtures with actual particle diameter ratios ranging from 0.9 to 0.7 in Figs. 3(a)–3(d). For all the cases shown, the large particles have a radius $a_1 = 545$ Å and a surface charge $Z_1 = 300$. For the small particles, we use the linear-diameter-charge relationship proposed by Pincus[15][16] to determine the charge for particles of a given size: $a_2 = 491$ Å, $Z_2 = 270$ in Fig. 3(a); $a_2 = 445$ Å, $Z_2 = 245$ in Fig. 3(b); $a_2 = 409$ Å, $Z_2 = 225$ in Fig. 3(c); and $a_2 = 382$ Å, $Z_2 = 210$ in Fig. 3(d). The actual particle diameter ratio is 0.9 in Fig. 3(a), 0.817 in Fig. 3(b), 0.75 in Fig. 3(c) and 0.7 in Fig. 3(d), while the diameter ratio of the effective hard spheres is 0.96 in Fig. 3(a), 0.92 in Fig. 3(b), 0.89 in Fig. 3(c), and 0.86 in Fig. 3(d). One can see that as the particle diameter ratio decreased more from unity, the freezing curve in the D–x phase diagram began to show a maximum with respect to x. Note that there is indeed a weak maximum which occurs near $x = 0$ in curve (a) which may be better seen from the minimum in $\bar{T} - x$ plane when we plot the effective freezing temperature in Fig. 4. The maximum becomes more pronounced as the diameter ratio is progressively decreased. As a result, the disordered crystalline alloy phase shrinks to small regions near $x = 0$ and $x = 1$ for the small particle diameter ratio as is shown in Figs. 3(c)–3(d) and in Fig. 1(a). Note that the solubility of small spheres in the crystals of large spheres is always larger than the solubil-
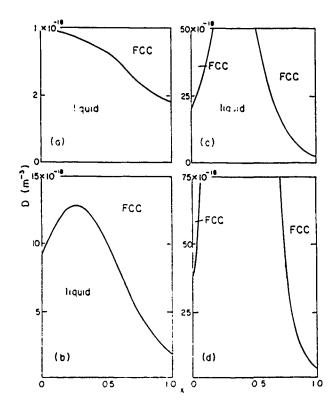

FIG. 3 D–x phase diagrams of binary colloidal particles with diameter ratio ranging 0.9 – 0.7 $a_1 = 545$ A, $Z_1 = 300$ for all cases, while $a_2 = 491$ A; $Z_2 = 270$ in (a): $a_2 = 445$ A, $Z_2 = 245$ in (b), $a_2 = 409$ A, $Z_2 = 225$ in (c); and $a_2 = 382$ A, $Z_2 = 210$ in (d).

ity of large spheres in the crystals of small spheres. This feature is also seen in the recent density-functional calculations of binary hard spheres.[17] Also note that the solid–liquid phase boundaries in Fig. 3(d) almost open up vertically at the high densities and the effective hard-sphere diameter ratio is 0.86 in this case. When the effective hard sphere diameter ratio decreases further, the solid–liquid phase boundaries rise even more sharply from $x = 0$ and $x = 1$, as shown in Fig. 1(a), where the effective hard sphere diameter ratio is 0.7. This suggests that the Hume–Rothery rule may be used in binary colloids only that the effective hard sphere diameters must be used for the miscibility criterion instead of the bare particle diameters. We also plot the effective freezing densities for all four cases in Fig. 4. As the particle diameter ratio becomes smaller, the minimum freezing temperature becomes deeper. Again, the locations of the maxima in Figs. 3(a)–3(d) are not the same as those of the minima in Figs. 4(a)–4(d), as we have explained above.

Finally, we show in Fig. 5 the effect of adding salt for a mixture of particles of diameter $a_1 = 545$ A, charge $Z_1 = 300$ and particles of diameter $a_2 = 445$ A, charge $Z_2 = 245$. Curve (a) is for the case of no added salt, curve (b) is for the case of 10 μM salt and curve (c) is for 20 μM salt. Note that adding salt has the effect of decreasing the interparticle repulsion by screening and thus increasing the freezing density. Moreover, the shortened screening length makes the particles more like hard spheres. As a result, the effective hard sphere diameter ratio should move closer towards the bare particle diameter ratio. Indeed, this is the case, the effective hard sphere diameter ratio is 0.91 with 20
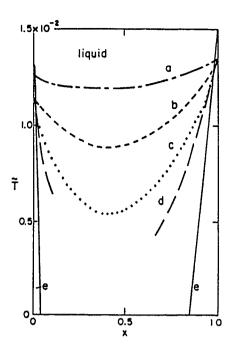
FIG. 4. $\tilde{T} - x$ phase diagrams of binary colloidal particles. Curves (a)-(d) correspond to the freezing temperatures of Figs. 3(a)-3(d) while (e) corresponds to Fig. 1(b).

μM salt as compared to 0.92 without salt where the bare particle diameter ratio is 0.817. In these mixtures, the diameter ratio of the effective hard spheres is larger than that of the bare particles. Thus, adding salt to change the diameter ratio of the effective hard spheres towards that of the bare particles enhances the maximum of the freezing curve in the D-x plane (minimum in the $T - x$ plane).

CONCLUDING REMARKS

We have determined the boundaries between the liquid phase and the disordered substitutional crystalline alloys for binary colloids by comparing the free energies of both the liquid and the solid phases. The free energies have been calculated variationally using the Gibbs–Bugolyubov inequality. Einstein oscillators are the reference system for the solids;

hard-sphere mixtures are the reference system for the liquids. We have shown the following: (1) For binary charged colloids, the freezing density as a function of the number fraction has a maximum. The maximum freezing density occurs in small-particle rich mixtures and the maximum freezing density increases sharply with decreasing particle diameter ratio. (2) When the effective hard sphere diameter ratio is about $0.86 \sim 0.85$, the solid–liquid boundaries rise almost vertically; the liquid phase is stable in most of the phase space except for small regions near the pure cases. (3) When the effective hard sphere diameters are used for the criterion, we have shown that the Hume-Rothery rule for the stability of the atomic substitutional alloys can also apply to binary charged colloids. (4) A maximum in freezing densities is equivalent to a minimum in freezing temperatures, i.e., an azeotropic or a eutectic. (5) Adding salt can enhance the maximum in the freezing density. (6) Finally, the pronounced stability of the liquid phase, i.e., the maximum in the freezing density in a colloidal mixture reflects the immiscibility at high densities (or low temperatures) just as it does in a binary metallic alloy. The glass formation observed experimentally corresponds to a deep minimum in the freezing temperatures (or pronounced freezing densities) in our calculation. The fact that the fluid phase can be stable up to an especially high density in a binary colloidal suspension can be helpful in colloidal processing where a high green-compact density is desired. A suspension of bimodal particle distribution may be used to achieve that goal. Indeed, this has been observed. Han et al.[18] have obtained a maximum in the green-body density (higher than those of the pure cases) when using a bimodal suspension. Another measurement that can reflect the maximum in the freezing densities we have discussed in this paper is the viscosity of the colloidal suspensions. The viscosity of the bimodal colloidal suspension may be found to have a minimum as a function of the number fraction at fixed particle number density (or total volume fraction). This has also been observed.[19]

FIG 5 D-x phase diagrams of binary colloidal particles where $a_1 = 545$. $Z_1 = 300$ and $a_2 = 445$. $Z_2 = 245$. Curve (a) is the freezing density without adding salt. (b) is that with $10\,\mu$M salt, and (c) is with $20\,\mu$M salt

[1]For a review of general properties of colloidal crystals and liquids, see P. Pieranski, Contemp. Phys. 24, 25 (1983).
[2]W Y Shih, I A Aksay, and R. Kikuchi, J Chem. Phys 86, 5127 (1987).
[3]P. M Chaikin and P. A. Pincus (unpublished).
[4]H. M. Lindsay and P. M. Chaikin, J. Chem Phys. 76, 3774 (1982).
[5]E. Liniger and R. Raj, J. Am. Ceram. Soc 70, 843 (1987)
[6]S Hachisu and S Yoshimura, Nature 283, 188 (1980)
[7]S Yoshimura and S Hachisu, J Phys Colloq C3, 46, 115 (1987)
[8]W Hume-Rothery, R E Smallman, and C. W Haworth, The Structure of Metals and Alloys (Metals and Metallurgy Trust, London, 1969)
[9]For example, see M Hansen, Constitution of Binary Alloys (McGraw-Hill, New York, 1958)
[10]For more general information on structural properties of metallic glasses, see D Turnbull, J Phys (Paris) 35, C4-1 (1974)

[11] W.-H. Shih and D. Stroud, J. Chem. Phy. 79, 6254 (1983).

[12] W. Y. Shih and D. Stroud, Phys. Rev. B 32, 7779 (1985); ibid, 7785 (1985).

[13] J. Lebowitz, Phys. Rev. A 133, 895 (1964).

[14] I. H. Umar, A. Meyer, M. Watabe, and W. H. Young, J. Phys. F 4, 1691 (1974).

[15] P. Pincus, Invited Paper at March Meeting of the American Physical So-
ciety, Los Angeles, California, 1983 (unpublished).

[16] W.-H. Shih and D. Stroud, J. Chem. Phys. 80, 4429 (1984).

[17] J. L. Barrat, M. Baus, and J. P. Hansen, Phys. Rev. Lett. 56, 1063 (1986).

[18] C. Han, I. A. Aksay, and O. J. Whittemore, in *Advances in Materials Characterization II*, edited by R. L. Snyder, R. A. Condrate, P. F. Johnson (Plenum, New York, 1985), p. 339.

[19] K. P. Darcovich and I. A. Aksay (unpublished).

APPENDIX III

MONTE CARLO SIMULATION OF ADSORPTION OF DI-BLOCK COPOLYMERS

WAN Y. SHIH, WEI-HENG SHIH, and ILHAN A. AKSAY
Department of Materials Science and Engineering, and Advanced Materials Technology Program, The Washington Technology Center, University of Washington, Seattle, WA 98195

Introduction

In this paper we are concerned with the morphology of the polymers adsorbed on surfaces, in particular di-block copolymers. Our work is motivated by the experimental findings of Hadziioannou et al. [1] on the steric forces between two adsorbed layers of di-block poly(vinyl-2-pyridine)/polystyrene (PV2P/PS) copolymer on mica surfaces. The PV2P block binds strongly on the mica surfaces and the PS block extends into the solvent toluene (good solvent for PS). Hadziiouannou et al. found that the repulsive forces between the two surfaces start at a distance D larger than 10 times the radius of gyration R_G of a free PS in toluene. Furthermore, the starting distance D increases with increasing degree of polymerization N of PS in a fashion $D \sim N^a$ with a close to 1. We study the adsorption of di-block copolymer with Monte Carlo simulations. The Monte Carlo simulations are especially powerful in dealing with kinetics which is important in systems where hysteresis is observed [1] and cannot be appropriately taken into account by analytical (or numerical) calculations based on equilibrium assumptions.

Model

We consider a cubic lattice in which there are M copolymer chains, each of which has N_2 anchoring segments and N_1 non-sticking segments (or monomers). Volume exclusion is taken into account by allowing no more than one monomer to occupy one lattice site. In general, we consider the monomer-monomer interaction up to the next-nearest-neighbor distance. The nearest-neighbor interaction E_1 and the next-nearest-neighbor interaction E_2 can be positive, zero, or negative, depending on solvent conditions. For instance, $E_1 = E_2 = 0$ represents an athermal polymer solution, which is the case we study in the present paper. Besides monomer-monomer interactions, a monomer also interacts with walls on the top and bottom of the lattice. When a monomer is right next to the wall, it gains energy E_b, where E_b can be either positive or negative. In the present study, E_{h1} is positive and E_{h2} is negative, 1 indicates a non-sticking polymer and 2 indicates an anchor polymer. We use the periodic boundary conditions in the xy directions.

In the simulations, the polymers are generated according to energy parameters using the Monte Carlo method, which means that whether or not a new monomer is added to a chain at a certain site in the process of polymerization is determined by the Boltzmann factor $e^{-\Delta E/T}$, where ΔE is the energy cost of the process and T is the absolute temperature. During the process of polymerization, as well as during other processes we will describe, the interaction between two adjacent monomers along a chain is not counted since they are chemically bonded to each other. When $E_1 = E_2 = 0$, the polymers we generated would be equivalent to self-avoiding random walks.

We allow three types of movements of the polymer chains. The first type is the Brownian motion, i.e., the polymer chains can move as a whole in a random fashion, illustrated in Fig. 1a. The second type is that of polymer wiggling; specifically, a monomer in a chain can flip, as illustrated in Fig. 1b. The third type is reptation, in which either end of a chain moves randomly to an adjacent unoccupied site and drags the rest of the chain along a "tube" that is shaped by its body, as illustrated in Fig. 1c. Reptation is especially important when the density is so high that the first two types of motion cannot effectively move the polymers. As the polymeric density increases, the motion of a polymer chain should be modified by the presence of other polymers and by itself (that is, the motion of one part of a polymer chain can be hindered by another part of the chain). The hindrance of motion is governed by the Boltzmann factor $e^{-\Delta E'/T}$, where $\Delta E'$ is the energy change due to the motion. Again, this process is simulated using the Monte Carlo method.

In order to compare with Ref. 1, we simulate polymers in a good solvent. For simplicity, we choose $E_1 = E_2 = 0$ for both the non-sticking polymers and the anchor polymers. The anchor polymers are of the strongly affinitive type whose $E_{h2} = -5T$, which means the adsorbed anchor polymers lay flat on the walls. For the non-sticking polymers, the walls are repulsive, i.e., $E_{b1} = 1T$. In the following, we fix the length of the anchor polymers, i.e., $N_2 = 10$ and change the length of the non-sticking polymers, i.e., N_1. For different values of N_1, we adjust the size of the simulation cell so that each dimension of the cell is more than 10 times the radius of gyration of the non-sticking polymers. For example, for $N_1 = 55$, the simulation cell is 42x42x60. The number of chains M in each run can be up to several hundred depending on the concentration.

Results and Discussion

Because of the strong affinitive nature of the anchor polymers, the walls prefer to be covered as much as possible by anchor polymers. At low initial segment density (defined as the average occupancy of a lattice site), the added di-block copolymers will all adsorb on the walls. As the initial segment density is increased, full surface coverage is reached quickly with shorter chains while the adsorption of longer chains begins to be limited by kinetics where surface coverage denoted as α is defined as the fraction of the surface sites that are occupied. To illustrate, we show the adsorption amount Γ, which is defined as the total number of segments of the adsorbed polymers, i.e., segments that are connected to the wall, per site, as a function of time for different chain lengths in Figs. 2-3. For $N_1 = 30$, 55% surface coverage is reached at about 6,000 Monte Carlo steps, as shown in Fig. 2. For longer chains ($N_1 = 45$), 45,000 Monte Carlo steps when we stop the simulation (see Fig. 3) the surface coverage is only about 52%. In the special case of di-block copolymers with non-sticking blocks and strongly affinitive anchors, the adsorption amount Γ is proportional to surface coverage α and can be expressed as $\Gamma = \alpha(N_1 + N_2)/N_2$. However, in general Γ is related to α but not necessarily proportional to α; for example, in the homopolymer case, one can have the same surface coverage but higher adsorption amount at higher bulk densities where the number of chains on the surface is higher but the fraction of a chain that is on the surface is smaller. The slow adsorption of long chains is the manifestation of the slow kinetics typical of long chains. Thus, the slow adsorption we observed is also indicative of the hysteresis behavior in the mechanical properties observed in experiments [1]
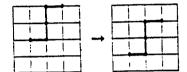
Fig. 1a.   A polymer can diffuse as a
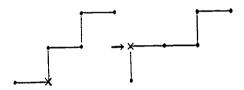whole (Brownian motion).

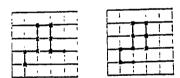Fig. 1b.   A monomer can wiggle within a chain
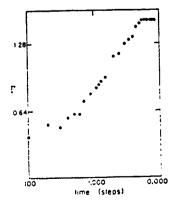(segment flipping).
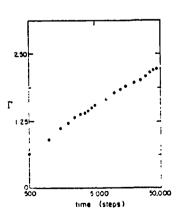

Fig. 1c.   Reptation
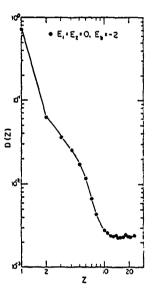

Fig. 2.   The adsorption amount Γ
vs. time for $N_1 = 10$.

Fig. 3.   The adsorption amount Γ
vs time for $N_1 = 45$.

Typical adsorption segment density profiles of both di-block copolymers and homopolymers are shown in Figs. 4 and 5. Figure 4 shows that the segment density of the adsorbed homopolymers decreases monotonically away from the surface and reaches the bulk value at a distance about 2 to 3 times the radius of gyration, R_G (for $N = 45$, $R_G = 3.9$). A more detailed study of the adsorption of homopolymers will be published elsewhere. The segment density profiles of the di-block copolymers adsorbed on the wall of various N_1 values are shown in Fig. 5. Since the anchor polymers are strongly affinitive, the segment density at $z = 1$ is mainly due to the anchor polymers. At $z \geq 2$, the segment density is attributed to the non-sticking polymers. The depletion of segments at $z = 2$ is due to the repulsive interaction of the non-sticking polymers with the surfaces, i.e., $E_{b1} = 1T$. The width of the depletion layer is roughly the radius of gyration R_{G_1} of the non-sticking polymers. This is why the width of the depletion layer increases with increasing values of N_1. Also note that for $N_1 = 10$, the surfaces are completely covered with anchor polymers, hence the depletion of segments at $z = 1$ does not occur in this case. Overall, one can see that the adsorbed di-block copolymers have a more uniform density profile than the homopolymers. Furthermore, the adsorbed di-block copolymers can extend out much farther (about $5 R_{G_1}$) than the homopolymers. Note that the extension of an adsorbed di-block-copolymer layer is already very large at low surface coverage ($N_1 = 45$ in Fig. 5 is an example) which is very different from that of an adsorbed homopolymer layer which is small at low surface coverage. The difference lies in that all the segments of a homopolymer are affinitive to the walls and therefore would prefer to lie on the walls when the surface coverage is low, resulting in very small layer thickness, whereas the non-adsorbing segments of a di-block copolymer do not stick.

In Fig. 6, we show the extension of the adsorbed di-block copolymer layers at high surface coverage with respect to N_1. In principle, the comparison should be made at the same surface coverage, since the layer thickness which may be characterized by the root-mean-square thickness H_1 or the outmost distance of the layer from the wall surface H_m increases with the increasing adsorption even though slowly. For $N_1 \leq 20$, we can have the wall surfaces completely covered with anchor polymers, namely, 100% surface coverage in a short time (4000 steps for $N_1 = 10$). With increasing chain length, the adsorption kinetics are slower, as we have discussed above, and it is difficult to achieve complete surface coverage. However, for the longer chains the adsorbed layer can extend to a distance $\geq 5 R_{G_1}$ even at about 55% surface coverage; for instance, for $N_1 = 45$ ($R_{G_1} = 3.9$), $H_m = 19$ and for $N_1 = 55$ ($R_{G_1} = 4.2$), $H_m = 24$. We plot H_m, H_1 of the adsorbed layers as a function of N_1 in Fig. 6. For $N_1 = 10$, the values of H_m and H_1 are taken at about complete surface coverage, for $N_1 = 20$ at about 76% coverage and for $N_1 \geq 30$ at about 55% coverage. The radius of gyration R_{G_1} of free polymers of equivalent length is also plotted for comparison in Fig. 6. It can be readily seen that the values of H_m are larger than $5 R_{G_1}$ (of free polymers in the solution) as we have discussed above. This agrees very well with Ref. 1 that the onset distance of repulsion between two layers is about $2 H_m$, which is larger han $10 R_{G_1}$.

Notice that in Fig. 6, H_m first increases with N_1 with power 0.6 for $N_1 \leq 30$ and with power 1.0 for larger N_1. The power 0.6 is in good agreement with the Flory's exponent [2] (see the exponent of R_{G_1} vs. N_1 in Fig. 6) and indicates that the non-sticking polymer behaves as in the bulk. The reason for a larger power at larger N_1 is that squeezing in the lateral direction occurs when N_1 is substantially larger than N_2 and the lateral squeezing forces the polymers to extend out in the normal direction To clarify this point further, we compare the
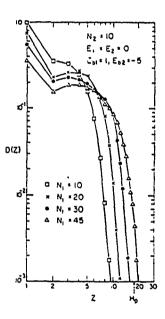
Fig. 4. The adsorption density profile of homopolymers of $N = 45$.

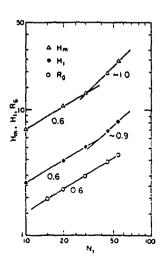Fig. 5. The density profiles of adsorbed di-block copolymers.

Fig. 6. The root-mean-square thickness H_1, the outmost distance of the adsorbed layer H_m, the radius of gyration R_G (of free polymers) vs N_1

projection of the radius of gyration of the non-sticking polymers on the surface (the xy plane), $R_{G_{1,xy}}$ to the radius of gyration of the anchor polymers R_{G_2} on the surface.

(a) If $R_{G_{1,xy}} \leq R_{G_2}/\sqrt{\alpha}$, the non-sticking polymers are hardly squeezed and should retain their free-polymer-like conformation. In this regime, H_1 and H_m should scale with N_1 with power 0 6.

(b) When $R_{G_{1,xy}} > R_{G_2}/\sqrt{\alpha}$, the non-sticking polymers are then squeezed in the lateral direction and hence would extend out in the perpendicular direction. H_1 and H_m in this case would scale with N_1 with a power close to 1 as predicted by the scaling theory of Alexander and de Gennes [3]. For all our cases, $R_{G_2} = 1.75$ while $R_{G_{1,xy}} = 1.19$ for $N_1 = 10$ at $\alpha = 100\%$; $R_{G_{1,xy}} = 1.75$ for $N_1 = 20$ at $\alpha = 76\%$; and for $\alpha \approx 55\%$, $R_{G_{1,xy}} = 2.24$ for $N_1 = 30$; $R_{G_{1,xy}} = 2.9$ for $N_1 = 45$; and $R_{G_{1,xy}} = 3.13$ for $N_1 = 55$. One can see that for small N_1, it falls into category (a) and for large N_1, it falls into category (b). The crossover occurs at about $N_1 = 30$ where $R_{G_{1,xy}} \approx R_{G_2}/\sqrt{\alpha}$. The behavior of $H_m \sim N_1^{1.0}$ at large N_1 is in agreement with Ref. 1.

Conclusions

We have simulated the adsorption behavior of di-block copolymers in a good solvent with the Monte Carlo method. We have shown that the segment density profiles of the adsorbed di-block copolymers are more uniform and the adsorbed di-block copolymer layers can extend much farther (at $H_{in} \geq 5R_{G_1}$), as compared to those of adsorbed homopolymers. We have also shown that at high surface coverage, H_m increases with increasing N_1; for small N_1, $H_m \sim N_1^{0.6}$ while for large N_1, $H_m \sim N_1^{1.0}$. The crossover occurs at $N_1 = 30$ for the cases we studied, i.e., $N_2 = 10$. The large N_1 behavior agrees with the experiment in Ref. 1. In addition, we have also shown that the adsorption of longer chains is very slow, which is the manifestation of the slow kinetics typical of long chains and is indicative of the hysteresis observed in the mechanical properties.

Acknowledgments

References

1. G. Hadziioannou, S. Patel, S. Granick, and M Tirrel, *J. Am. Chem Soc* 108, 2869 (1986).
2. For general informations, see P. G de Gennes, *Scaling Concepts in Polymer Physics*, Cornell University Press, Ithaca, N.Y., 1979.
3. S. Alexander, *J Phys. (Paris)*, 38, 983 (1977); P. G de Gennes, *Macromolecules*, 13, 1069 (1980).

APPENDIX IV

DENSITY PROFILES OF SEMI-DILUTE POLYMER SOLUTIONS NEAR A HARD WALL: MONTE CARLO SIMULATION

WAN Y. SHIH, WEI-HENG SHIH and ILHAN A. AKSAY
Dept. of Materials Science and Engineering
University of Washington, Seattle, WA 98195

Introduction

A semi-dilute polymer solution is one in which polymers overlap. The bulk prop··rties of semi-dilute polymer solutions have been studied extensively[1-3] and much has been known. Especially, the scaling theory has been very successful.[1,2] The predictions of the scaling theory about various physical quantities as a function of polymer concentration, c, have been confirmed experimentally.[1,3]

While the bulk properties of semi-dilute polymer solutions are well studied, the interfacial properties of a semi-dilute polymer solution are less well known. For example, the density profiles near a hard wall are difficult to examine experimentally. When a polymer solution is near a hard wall, it is thought that the polymer concentration is depleted in the proximity of the wall and the thickness of the depleted layer is on the order of the correlation length ξ. For semi-dilute polymer solutions in a good solvent, de Gennes predicts that the polymer concentration rises in a power-law fashion as $c(z) \sim (z/\xi)^m$, where z is the distance away from the wall and $m = 5/3$ [Refs. 2,4]. By arguing that the bulk osmotic pressure Π should be proportional to the first layer concentration $c(z=1)$, de Gennes predicts that in a lattice model, the concentration in the first layer near the wall behaves as $c(z = 1) \sim c^{3/4}$ [Ref. 2]. Though interfacial properties are technologically important, detailed study of polymer solutions near a wall, especially the determination of the concentration profiles, is experimentally difficult. The purpose of the present paper is therefore to use the Monte Carlo method[5] to simulate polymer solutions near a hard wall, to give a detailed account for the density profiles.

Model

We consider a $N_x \times N_y \times N_z$ cubic lattice in which there are M polymer chains each with N segments (monomers). A monomer is interacting with other monomers within the same chain (intra-chain) as well as in the other chains (inter-chain). In general, we consider for the monomer-monomer interaction (1) volume exclusion and (2) interactions up to the next nearest neighbors. Volume exclusion is taken into account by allowing no more than one monomer to occupy one lattice site. The nearest-neighbor interaction energy E_1 and the second-nearest-interaction E_2 can be positive, zero, or negative. One can control the values of E_1 and E_2 to simulate various solvent conditions. For instance, $E_1 = E_2 = 0$ represents an athermal polymer solution, which is the case we study in the present paper. Besides the monomer-monomer interactions, a monomer is also interacting with the hard walls on the top and at the bottom of the Monte Carlo cell. By hard wall we mean the wall is inpenetrable for the polymers. In addition to inpenetrability, we consider a nearest-neighbor wall-monomer interaction E_b, that is, when a monomer is right next to the wall, it gains energy E_b. In the present study, we consider $E_b = 0$. In the xy directions, we use the periodic boundary conditions.

Three types of movements are considered in the simulation. The first type of motion is the Brownian motion, namely, the polymer chains move as a whole in a random fashion as illustrated in Fig. 1a. The second type of motion is that a polymer can wiggle, specifically, a monomer in a chain can flip as illustrated in Fig. 1b. The third type of motion is reptation, that is, either end of a chain moves randomly to an adjacent unoccupied site and drags the rest of the chain along a *tube* that is shaped by its body as illustrated in Fig. 1c. Reptation is especially important when the density is high, so that the first two types of motions cannot effectively move the polymers. The motion of a polymer chain may be hindered by the presence of other polymers and/or by itself (that is, the motion of one part of a polymer

for $\varphi = .0925$, where φ is the bulk density. The extrapolated slope decreases with increasing bulk segment density and does not agree with the value 5/3 predicted by the scaling theory. The reason is that even with $N = 100$, the correlation length is still not large enough. In order to have the right extrapolated slope at small z one should have $z/\xi \ll 1$. Therefore, instead of extrapolating the exponent directly from the segment density profiles at small z, we use the following scaling form for the segment density profiles:

$$\varphi(z) = \varphi(1 - e^{-(\frac{z}{\xi})^m}) \qquad (2)$$

where φ is the bulk segment density and ξ is the correlation length. This scaling function gives the right behavior both at small z and at large z. At small z/ξ, $\varphi(z)$ increases in a power law fashion with z: $\varphi(z) \sim (z/\xi)^m$ and at $z/\xi \gg 1$, $\varphi(z)$ gives the bulk density φ. We fit the three density profiles shown in Fig. 4 to the above form and the results are shown in Fig. 5. One can see that the fit is extremely good. Although the scaling function Eq. (2) fits well to the density profiles, we should mention that the choice of the scaling function is not unique as long as the function has the right behavior at small z and at large z. We choose the form Eq. (2) for the following reasons. (i) It is easy to plot and to extract the parameters m and ξ using Eq. (2). (ii) The exponential form is rather a natural choice for surface density profiles. For many systems, the interfacial density profiles are known to he exponential (hyperbolic tangential) except that the exponent m is unity in these systems while m may be different from unity for polymer solutions. From the lines in Fig. 5, we extract the exponent m which is the slope of the lines and the correlation length ξ, which is $e^{y_0/m}$, where y_0 is the intercept of the lines with the y axis. (a) $m = 1.64$, $\xi = 2.3$ for $\varphi = 0.135$; (b) $m = 1.61$, $\xi = 2.8$ for $\varphi = .107$; and (c) $m = 1.68$, $\xi = 3.2$ for $\varphi = .0925$. The extracted values of both m and ξ are very reasonable: (1) the values for m are in very good agreement with the value 5/3 predicted by the scaling theory and (2) the values for ξ show the right trend of decrease with increasing bulk concentration.

Throughout the whole semi-dilute density range we have simulated (up to $\varphi = 1.6$ for $N = 100$ and $\varphi = .32$ for $N = 40$), the scaling function Eq. (2) fits the segment density profiles remarkably well. For the exponent m, we always obtain values around 1.6 (ranging from 1.55 to 1.7). Although the segment density profiles are more complicated in the dilute regime, we also get very good fit if we just use the portion of the density profiles that are near the wall. An example is shown in curve (d) in Fig. 6, where we obtain $m = 1.63$ and $\xi = 5.9$. Thus, the segment density near the wall is proportional to $(z/\xi)^{5/3}$ in both dilute and semi-dilute solutions, except that $\varphi(z)$ increases monotonically in semi-dilute solutions but undergoes a maximum before reaching the bulk density value in dilute solutions. A more detailed account of the density profiles in the dilute regime will be published in a separate paper.

We show the extracted values of ξ versus the bulk segment density φ in a double-logarithmic plot in Fig. 6 where full circles and triangles represent $N = 100$ and $N = 40$ respectively. (1) ξ is independent of the segment density at low segment densities. Notice that the values of ξ at low segment densities are approximately equal to the values of the radii of gyration $R_G \sim 6.3$ for $N = 100$ and ~ 3.6 for $N = 40$, which is in agreement with the notion that in the dilute regime, the polymers are well separated and the correlation length is equal to the radius of the gyration of the chains. (2) When the segment density reaches the crossover density φ^*, the estimated values for $N = 100$ and for $N = 40$ are indicated by arrows in Fig. 6. The two sets of data fall on one line with a slope ~ -0.75, in agreement with the scaling prediction that the correlation length ξ in the semi-dilute regime depends only on the segment density and behaves as $\xi \sim \varphi^{-3/4}$. The effect of N is to change the value of the crossover segment density φ^*. In view of the remarkable result for the correlation length ξ obtained from the segment density profiles near a wall, this may turn out an easier way of calculating the correlation length. Normally, the correlation length is obtained from calculating the density-density correlation function, which is very time-consuming.

In Fig. 7 we plot φ_1 vs. φ where φ_1 is the segment density at $z = 1$ and φ is the bulk

chain can be hindered by another part of the chain). The hindrance of motion is correctly taken into account by the Boltzmann factor $e^{-\Delta E/T}$, where ΔE is the energy change due to the motion. Again, this is simulated with the standard Metropolis Monte Carlo method.

In all the simulations, for a given N, we choose Nx, Ny and Nz all at least larger than $8 R_G$ to ensure that the obtained R_G is not affected by the boundary conditions of the Monte Carlo cell. In each run, we discard 2000-6000 Monte Carlo steps and average over 5000-10000 Monte Carlo steps. For a given initial concentration $\varphi_{in} = MN/NxNyNz$, we perform 2-4 independent runs.

Results

Chains with $E_1 = E_2 = 0$ correspond to self-avoiding random walks and represent polymers in an athermal solution. In the Flory-Huggins's language, the χ parameter is zero in this case. We found that the double-logarithmic plot of the radius of gyration R_G of polymers with degree of polymerization N versus N (not shown) in the dilute regime has a slope 0.6, which agrees with the Flory's number v which is 0.6 [Ref. 7] for athermal polymer solutions and is also within the numerical error of the self-avoiding random walks, which is .59 [Ref. 7].

One may define the segment density φ as the average occupancy of a lattice site by a segment (monomer). The segment density φ is related to the weight concentration c as $c = m\varphi/a^3$ where m is the molecular weight of a monomer and a is the segment length (lattice constant in the model). Throughout the text, we will use φ rather than c for convenience.

As one increases the segment density, at some point one passes from the dilute regime, where chains are well separated, to the semi-dilute regime, where chains overlap. An estimate of the crossover segment density φ^* from the dilute solution to the semi-dilute solution may be made by

$$\varphi^* = \frac{N}{\frac{4\pi}{3}R_G^3} , \tag{1}$$

where N is the number of segments in a chain or the degree of polymerization and R_G is the radii of gyration of the chains respectively. Knowing the value for R_G from the simulations, one can calculate φ^*. For example, when $N = 40$, $R_G = 3.6$, therefore $\varphi^* = 0.2$; when $N = 100$, $R_G = 6.3$ and $\varphi^* = 0.095$.

Because of the overlapping of chains, a semi-dilute solution is very different from a dilute solution. For instance, for a given N, the radius of gyration R_G is independent of the segment density in dilute solutions but has φ dependence in the semi-dilute regime: $R_G^2/N \sim \varphi^{-1/4}$ [Ref. 1]. we show R_G^2/N versus the segment density φ in a double-logarithmic plot in Fig. 2 where full circles represent $N = 100$ and triangles represent $N = 40$. In both cases, R_G remains constant at low segment densities. At higher segment densities the two sets of data fall on one line with a slope -0.23, which is within the numerical error bars of the value $-\frac{1}{4}$ predicted by the scaling theory. Notice that R_G changes from dilute-solution behavior to semi-dilute-solution behavior at about the estimated crossover segment density φ^*, which is .095 for $N = 100$ and .2 for $N = 40$, as indicated by arrows in Fig. 2. In the following, we will focus on the density profiles near a wall in the semi-dilute regime where R_G^2/N shows the φ dependence.

Typical density profiles in the semi-dilute regime are shown in Fig. 3. Curve (a) is for $N = 40$ in a $35 \times 35 \times 50$ lattice with the bulk segment density $\varphi \sim 0.23$, and curve (b) is for $N = 100$ in a $50 \times 50 \times 70$ lattice with the bulk segment density $\varphi \sim 0.15$. The segment density is indeed smaller near the walls and rises monotonically toward the bulk value. The thickness of the depletion layer is on the order of the correlation length, as evidenced by the wider depletion layers in curve (b) where the correlation length ξ is larger than in curve (a), as is shown in more detail below. To look at the density profiles near the wall more closely, we show density profiles $\varphi(z)$ vs. z in a double-logarithmic plot for $N = 100$ in Fig. 4, where z is the distance away from the wall and $\varphi(z)$ is the segment density at distance z. The extrapolated slope at small z is (a) 1.23 for $\varphi = 1.35$. (b) 1.27 for $\varphi = .107$ and (c) 1.41

segment density, as represented by the plateau in Fig. 4, for the semi-dilute regime. Again, full circles represent $N = 100$ and triangles represent $N = 40$. Again, the estimated crossover segment density $\varphi^* = .095$ for $N = 100$ and $\varphi^* = .2$ for $N = 40$ are indicated by arrows. One can see that above the crossover segment densities, the two sets of data fall on one line with a slope ~ 2.2, indicating that the behavior of the first-layer segment density is indeed similar to that of the bulk osmotic pressure Π, which behaves as $\Pi \sim \varphi^{9/4}$.

Summary

We have simulated semi-dilute athermal polymer solutions near a hard wall using the Monte Carlo method. We consider three types of polymer movements: (1) Brownian motion of a chain, (2) flipping of monomers, and (3) reptation. We have shown that in the semi-dilute regime, the radius of gyration R_G has φ dependence: $R_G^2/N \sim \varphi^{-0.23}$, in agreement with the scaling theory and also with the experiment. We have shown that in the semi-dilute regime, the segment density is depleted near the wall and the thickness of the depletion layer is on the order of the correlation length. By fitting the segment density profiles to the form Eq. (2), we are able to extract the exponent of the density profiles at small z/ξ, which ranges from 1.55 to 1.7, in agreement with 5/3 as predicted by the scaling theory. We have also extracted the correlation length which is also remarkably good: ξ is equal to the radius of gyration R_G at low densities and behaves as $\xi \sim \varphi^{-0.75}$ in the semi-dilute regime, again, in agreement with the scaling theory and also with the experiment. The first-layer segment density near the wall behaves as $\varphi_1 \sim \varphi^{2.2}$, indicating that the behavior of φ_1 is similar to that of the bulk osmotic pressure Π, which is known to behave as $\Pi \sim \varphi^{9/4}$. Therefore, for a hard wall, φ_1 is indeed proportional to the bulk osmotic pressure.

Acknowledgment

References

1. M. Daoud, J. P. Cotton, B. Farnoux, G. Jannink, G. Sarma, H. Benoit, R. Duplessix, C. Picot, and P. G. de Gennes, *Macromolecules*, 8, 804 (1975).
2. P. G. de Gennes, *Scaling Concepts in Polymer Physics*, (Cornell University Press, Ithaca, 1979), Chapter III and references cited therein.
3. K. Okano, E. Wada, Y. Taru, H. Hiramatsu, *Rep. Prog. Polym. Sci. Japan*, 17, 141 (1974).
4. P. G. de Gennes, *Macromolecules*, 14, 1637 (1981).
5. For a review, see *Monte Carlo Methods in Statistical Physics*, (Springer-Verlag, Berlin-Heidelberg, 1986), ed. K. Binder, Chapter 1.
6. N. Metropolis, A. W. Rosenbluth, M. N. Rosenbluth, A. H. Teller, E. Teller, *J. Chem. Phys.*, 21, 1087 (1953).
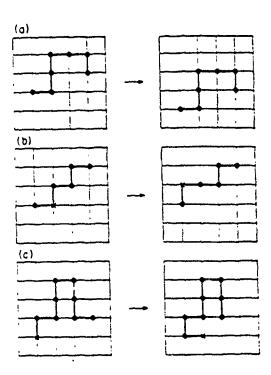7. For a review, see Ref. 2 and the references therein.

Fig. 1. (a) Brownian motion of the chain, (b) flipping of a monomer within a chain and (c) reptation of a chain.
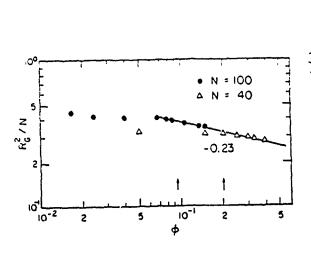

Fig. 2. R_G^2/N vs. φ for $N = 40$ ($\triangle$) and for $N = 100$ ($\bullet$) where R_G and N are as defined in Fig. 3 and φ is the bulk segment density.
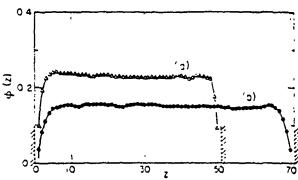

Fig. 3. Typical segment density profiles from $z = 1$ to N_z for (a) $N = 40$ with the bulk segment density $\varphi \sim 0.23$ and (b) $N = 100$ with the bulk segment density $\varphi \sim 0.15$. Notice that for profile (a) the walls are at $z = 0$ and $z = 51$ and for profile (b) the walls are at $z = 0$ and $z = 71$.
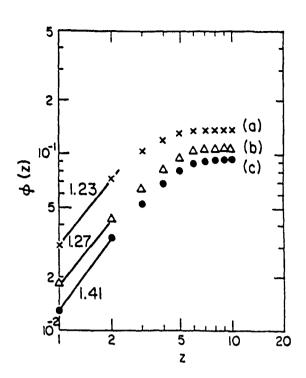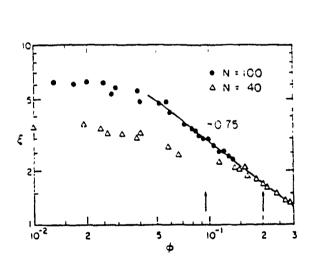
Fig. 4. The close-up of the segment density profiles for $N = 100$ near the wall (a) $\varphi = 0.135$, (b) $\varphi = 0.107$ and (c) $\varphi = 0.0925$, where φ is the bulk segment density.
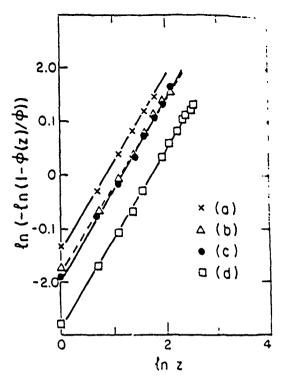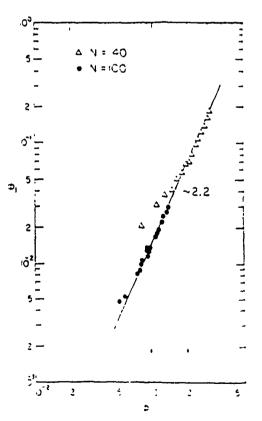

Fig. 5. $\ln\{-\ln[1 - \varphi(z)/\varphi]\}$ vs. $\ln z$. The fitted values for the exponent m and the correlation length ξ are (a) $m = 1.64$, $\xi = 2.3$ for $\varphi = 0.135$, (b) $m = 1.61$, $\xi = 2.8$ for $\varphi = 0.107$, (c) $m = 1.68$, $\xi = 3.2$ for $\varphi = 0.0925$, (d) $m = 1.63$, $\xi = 5.9$ for $\varphi = 0.0167$.

Fig. 6. ξ vs. φ for $N = 40$ ($\triangle$) and for $N = 100$ ($\bullet$) where ξ is the correlation length and φ is the bulk segment density.

Fig. 7. φ_1 vs. φ for $N = 40$ ($\triangle$) and for $N = 100$ ($\bullet$) where φ_1 is the first-layer segment density near the wall and φ is the bulk segment density.

APPENDIX V

NEW SIMULATION OF POLYMERS ON SURFACES

F. Aguilera-Granja and Ryoichi Kikuchi
Department of Materials Science and Engineering, FB-10, and
Washington Technology Center
University of Washington, Seattle, WA 98195

ABSTRACT

A new method of simulation based on the output of the analytical equilibrium calculation of the Cluster Variational Method (CVM) is used to obtain information about the properties of the polymers adsorbed on a surface. We find a strong preferential adsorption of longer chains, in agreement with experimental observations. This tendency is more pronounced in neutral polymers than in polyelectrolytes. Other geometrical properties like trains, tails, and loops of adsorbed polymers are also calculated.

I. MODEL AND METHOD

Statistics of polymers adsorbed on a solid surface has been studied using analytical techniques[1] and also by the Monte Carlo simulations[2]. Analytical techniques are almost always based on the Flory-Huggins approach[3]. An exception is the work by Kurata et al.[4] which uses a different method of estimating the free energy, namely they took account of correlations among polymer segments better than the Flory-Huggins method by using the pair and square approximations of the cluster variation method (CVM)[5]. Our approach is similar as Kurata's in the sense that we use the CVM pair approximation, but in addition to that, we have extended the analytical method to do a simulation based on the CVM outputs.

As is done in most of the polymer statistics, we place polymer segments and solvent molecules on a lattice structure ; for the sake of simplicity we use the simple cubic lattice. The configurational probabilities of the lattice points are written as $x_{n;i}$ where $n(=1,2,3...)$ is the plane number from the surface, $n = 1$ being the plane next to the solid surface, and $i(=0,1,..,11)$ designates the kind of species. The subscript 0 is for solvents particles, 1 to 3 for the end segments of a polymer, 4 to 7 for internal neutral polymer segments, and 8 to 11 for internal charged polymer segments. Directions of bonding arms are also included in defining the configuration i ; for example the direction of the bonding arm of an end segment is down for

$i = 1$, up for 2 and parallel to the solid surface for 3. One basic difference of our approach from Flory-Huggins' is that we use the probabilities for configurations of a lattice-point pair also. Probabilities for a pair of i and j species in a same plane n is written as $y^{(a)}_{n;ij}$ with a superscript (a) when the two segments are connected by a chemical bond, and with a superscript (b) when they are not connected. The probability for a pair with i on n and j on $n + 1$ is written as $z^{(a)}_{n+(1/2);ij}$ for bonding and the superscript (b) for non-bonding. The pair variables are introduced not only for the purpose of taking better account of segment correlations, but also in order to construct simulations based on the CVM outputs.

Before doing the simulation, we first solve the equilibrium state analytically using the CVM pair approximation, assuming appropriate interaction potentials. Solvent particles may interact with polymer segments. The simulation is done as follows. We construct the system from bottom to top starting from the surface, from left to right, and from back to front, by placing a species on a lattice point one at a time. Let us suppose that the lattice has been built up to the edge formation as shown in Fig. 1, and the next one to be placed is i on the nth plane. Around the i point, half of the nearest neighbors have been placed and known.
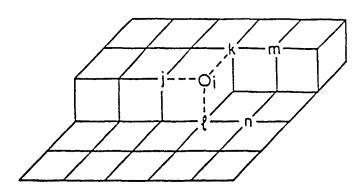

Fig. 1 An intermediate stage of constructing the simple cubic lattice.

Taking into account the nature of correlations in the pair approximation and following the general approach of the superposition, we can approximately write the probability of finding the corner configuration in Fig. 1 as

$$p_n(i, j, k, \ell) = y_{n;\,ji}\, y_{n;\,ki}\, z_{n-(1/2);\,\ell i} / (x_{n;\,i})^2 \, . \tag{1}$$

It can be proved that this relation satisfies the right relationship for evaluation of the pair probabilities[6]. When j, k, and ℓ in Fig. 1 are known, we want to formulate the probability of placing the species i at the circled point. The conditional probability $P_n(i;\,j, k, \ell)$ of finding i in the n plane when j, k, and ℓ are known is defined as

$$P_n(i;\,j, k, \ell) = p_n(i, j, k, \ell) / \sum_m p_n(m, j, k, \ell) \, . \tag{2}$$

We construct the lattice in such a way that (2) is satisfied at every point. For the first plane next to the surface, we use relations similar to (1) and (2) reduced to the 2-dimensional space. Because we assigne connecting arms in the probabilities, some additional geometrical constraints are needed in (2), but we do not go into the details. The size of the system in this simulation is 50x50x20, the average number of polymers is 21 in every simulation, and standard deviation of the number of polymers is 3.6. As the plane location n increases towards our end plane $n = 20$, the polymer properties level off and approach the bulk. The $n = 21$ plane, which is not in the formulation explicitly, is equivalent to the plane at $n = 20$.

II. RESULTS

In this simulation we work with the case of a bulk density $\rho(*) = 0.01$, which is defined as the fraction of lattice points occupied by polymer segments. The bulk average length is $\ell_{av} = 22$ segments. Since we control the average length by the ratio of end segments to the internal segments, the length is exponentially polydispersed, as has been shown before.[7]

We present two examples of choosing interaction energies. The first case is the neutral polymers for which we assume the van der Waals type interaction between polymer segments on the first layer and the colloid surface. In the second example for polyelectrolytes, in addition to the van der Waals type attraction, we consider attraction from the colloid surface due to electrical charge, and also repulsion between charges on the polyelectrolyte molecules. For the latter case we assume neutral and charged segments alternate along the polymer chain.

The density profiles as functions of the distance away from the surface due to the analytical CVM results are shown in Fig. 2, where the solid curve is for neutral polymers and a dashed curve for polyelectrolytes. The neutral polymers have higher coverage 0 and larger net adsorbed amount Γ_{exc}[1] than polyelectrolytes (0 = 0.58 and Γ_{exc} = 0.89 against 0 = 0.42 and Γ_{exc} = 0.40), where Γ_{exc} is defined as the sum of $\rho(n) - \rho(^*)$ over n. The density decreases monotonically in the neutral case, while for the polyelectrolytes there is a depression close to the surface because of the electrical repulsion of the charged segments. This means that the shape of the adsorbed polyelectrolytes is more flat than the neutral case [8].
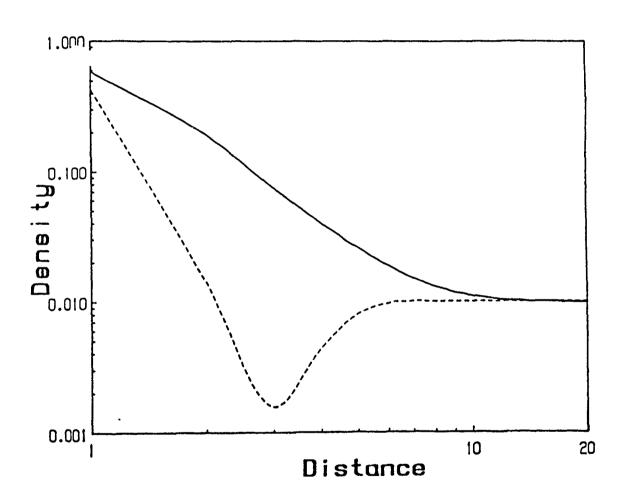

Fig. 2 Analytical results for adsorption due to the CVM.

In our treatment of the bulk polymer solution, the length ℓ has an exponential distribution[7]. For the case of our examples, the bulk average length is $\ell_{av} = 22$ and the ratio of the weight-average molar mass M_w to the number average mass M_n, called the polydisperse index, is equal to 1.9. Compared with the bulk properties, it is expected that the length distribution changes near the interface, because the polymers feel a different environment, i.e. the presence of the surface and the high density of polymers on the surface. Figure 3 shows the frequency distributions of the adsorbed polymers and polyelectrolytes. Deviation from the exponential behavior is noticeable near $\ell = 0$. The adsorbed polymer distributions are broader than the bulk case, and the average lengths are $\ell_{av} = 72$ and $\ell_{av} = 40$ for neutral polymers and polyelectrolytes, respectively. Their polydisperse indices are 1.41 and 1.48. This means that the surface likes to have longer polymers adsorbed on it, the tendency being larger for the neutral case in which the distribution is broader. It is because in the neutral case there is a big contribution of entropy that comes from the long tails of the adsorbed polymers. The polyelectrolyte distribution is narrower because the energy plays a more important role than the entropy. It is also consistent with the fact that the polyelectolytes have shorter tails going into the solution than the neutral case. This strong preferential adsorption for longer chains has been observed experimentally [9] in the case of neutral polymers. We see here that the same phenomenon is present in polyelectrolytes, but in a lesser degree.

Another result of this simulation is that for long neutral polymers approximatly 30% of the polymer segments are trains, more than 40% are on loops and the rest are on tails; for long polyelectroly tes, 83% are on trains and the rest on tails, the fraction on loops being negligible.

Key words: Polymer adsorption. Simulation, CVM.

REFERENCES

1. R.J. Roe, *J. Chem. Phys.*, 60, 4192 (1974).
2. E. Eisenrieger, K. Kremer and K. Binder, *J. Chem. Phys.*, 77, 6296 (1982).
3. J.M.H.M. Scheutjens and G.J. Fleer, *J. Phys. Chem.*, 83, 1619 (1979).
4. M. Kurata, M. Tamura and T. Watari, *J. Chem. Phys.*, 23, 911 (1955).

5. R. Kikuchi, *Phys. Rev.*, **81**, 988 (1951).

6. R. Kukuchi, *Phys. Rev. B*, **22**, 3784 (1980).

7. F. Aguilera-Granja and R. Kikuchi, presented at the 1988 MRS Fall Meeting, Boston, Mass., 1988 (unpublished).

8. F. Aguilera-Granja and R. Kikuchi to be published.

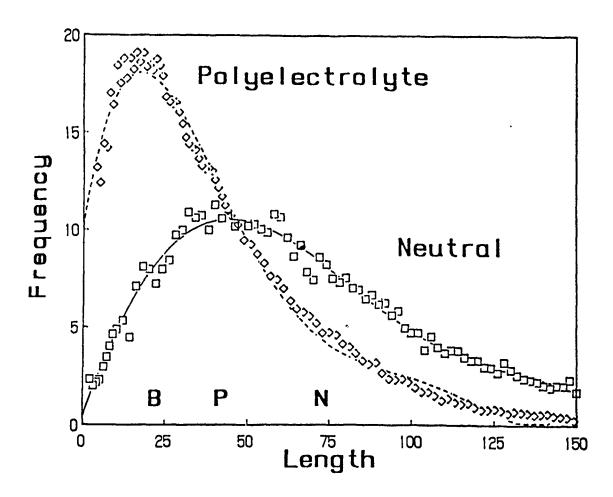9. C. Vander Linde and R. van Leemput, *J. of Colloid and Int. Sci.*, **67**, 63 (1978).

Fig. 3 Length dependence of adsorption obtained by the CVM simulation. The points B, P and N indicate the average lengths of the bulk, polyelectrolytes and neutral polymers.

APPENDIX VI

STABILITY OF A BINARY COLLOIDAL SUSPENSION AND ITS EFFECT ON COLLOIDAL PROCESSING

WAN Y. SHIH, WEI-HENG SHIH, JUN LIU and ILHAN A. AKSAY
Dept. of Materials Science and Engineering
University of Washington, Seattle, WA 98195

Introduction

The stability of a colloidal suspension plays an important role in colloidal processing. Especially, the stability of the colloidal fluid phase is vital in achieving high green densities where by colloidal fluid phase we mean a phase in which colloidal particles are well separated and free to move about. With monodisperse electrostatic suspensions, by controlling parameters such as pH, salt concentration, one can achieve high green densities in the repulsive (high zeta potential) regime where the suspension is well dispersed as a colloidal fluid and low green densities in the attractive (low zeta potential) regime, where the suspensions are flocculated.[1,2] While there is an increased interest in using bimodal suspensions to improve green densities, the stability of a binary suspension as a colloidal fluid and how the stability affects the green densities have not been well studied yet. Traditionally, the effect of using bimodal-particle-size distribution has only been considered in terms of geometrical packing developed by Furnas.[3] This kind of consideration is valid only when the particles are not interacting, i.e., hard sphere like or the particles are heavy enough so that the packing of particles are governed simply by gravitiy such as in Ref. 4. With the advance in powder technology, smaller and smaller particles are available for ceramic processing. Thus, the traditional consideration of geometrial packing for the green densities of bimodal suspensions may not be enough. The interaction between particles must be taken into account.

The purpose of this paper is to take into account the interparticle interactions explicitly and to examine the stability of a binary suspension as a colloidal fluid using analytic calculations as well as numerical simulations. From suspension stability, we will then discuss how the use of a bimodal (binary) suspension affects the green density. We will divide our studies into two regimes, i.e., the repulsive regime and the weakly attractive regime.

In the repulsive regime, flocculation does not occur. Suspensions are governed more by equilibrium conditions. We examine the stability of the supensions by constructing the solid-fluid phase diagrams. On the contrary, in the weakly attractive regime, at least one of the species has attractive interparticle interaction. The suspension may undergo flocculation and are more dominated by the kinetic conditions. To take into account the kinetic effect more accurately, we use Monter Carlo simulations to study the clustering befhavior of the suspensions.

Repulsive Regime

Model

We consider a binary aqueous suspension of N_1 particles of radius a_1, charge Z_1, and N_2 particles of radius a_2, charge Z_2 with volume Ω. In the absence of added electrolytes, there will be $N_1 Z_1 + N_2 Z_2$ counter ions (H_3O^+ or OH^- depending on the system) in solutions to neutralize the charges on the colloidal particles. If the number density of the colloidal particles is not too high or the temperature is not too low, the effective interactions between the colloidal particles can be adequately treated within the Debye-Huckel approximation. In MKSA units, the interaction takes the form

$$U(r_{ij}) = \frac{Z_i Z_j e^2}{4\pi\varepsilon_0 \varepsilon r_{ij}} \left[\frac{e^{qa_i}}{1 + qa_i}\right] \left[\frac{e^{qa_j}}{1 + qa_j}\right] e^{-qr_{ij}} . \tag{1}$$

Here r_{ij} is the separation between the centers of particle i and particle j, ε is the static dieletric constant of water, ε_0 is the permittivity of free space, e is the electronic charge, and q is the inverse screening length which satisfies

$$q^2 = \frac{e^2}{\varepsilon_0 \varepsilon k_B T} \sum_i n_i(z_i^2) , \tag{2}$$

where k_B is the Boltzmann constant, T is the absolute temperature, z_i and n_i are the charge and the number density of the ith species of ions, respectively. The term in the brackets of Eq. (1) is the size correction which takes into account the fact that part of the volume of the suspension is not available for screening due to the finite sizes of the colloidal particles.

When the colloidal suspension is at equilibrium, its thermodynamic properties are determined by the Helmholtz free energy $F = E - TS$, where E is the total energy and S is the entropy. For a system of particles interacting via the potential Eq. (1), the free energy per particle takes the following form:

$$F = \frac{1}{2N} \sum_{\substack{i,j \\ i \neq j}}^{N} \frac{Z_i Z_j e^2}{4\pi\varepsilon_0 \varepsilon} \left(\frac{e^{qa_i}}{1 + qa_i}\right) \left(\frac{e^{qa_j}}{1 + qa_j}\right) < \frac{1}{|\vec{r}_i - \vec{r}_j|} e^{-q|\vec{r}_i - \vec{r}_j|} >$$

$$+ E_{kin} - TS , \tag{3}$$

where E_{kin} and S are the kinetic energy and the entropy per particle, $N = N_1 + N_2$ is the total number of particles in the system, $< \ >$ denotes the thermal average over the canonical ensemble, a d $\vec{r}_i$ is the position of particle i. Equation (3) includes only the part of the free

energy that depends on the arrangement of the particles. These are the terms that are relevant in determining the structure of the colloidal suspension.

The free energy can be obtained from Eq. (3) by the use of a variational principle based on the Gibbs-Bogolyubov inequality which states as follows:

$$F \leq F_0 + <U - U_0>_0 \equiv F' , \tag{4}$$

where F_0 is the free energy of the reference system and $<U - U_0>$ is the potential energy difference of the system of interest and the reference system. Since F is upper bounded by F', we can then approximate F to be the minimum of F' with respect to the appropriate variables, that is, $F \simeq F'(x_0, y_0)$ and

$$\frac{\partial F'(x,y)}{\partial x}\Big|_{x-x_o} = 0 \quad \text{and} \quad \frac{\partial F'(x,y)}{\partial y}\Big|_{y-y_o} = 0 \tag{5}$$

where x and y are the appropriate variables.

For the solid phases, it is convenient to choose an ensemble of Einstein oscillators to define the reference system: each particle of type 1 or 2 oscillates about a lattice point independently in a potential well with a frequency ω_1 and ω_2. The free energy may then be written in terms of ω_1 and ω_2 and the free energy of the equilibrium state is determined by minimizing the free energy with respect to ω_1 and ω_2.

For the reference system of the liquid phase we consider a binary hard sphere fluid where particles are interacting via the hard sphere potential,

$$U_0(r_{ij}) = \begin{array}{ll} \infty & r_{ij} < \sigma_{ij} \\ 0 & r_{ij} \geq \sigma_{ij} \end{array} \tag{6}$$

in which $\sigma_{ij} = (\sigma_i + \sigma_j)/2$, where σ_i, the effective hard sphere diameter of particle i, is not, in general, equal to a_i, the actual diameter of a type-i particle. Again, the free energy of the fluid state can be expressed in terms of σ_1 and σ_2 and the free energy of the equilibrium fluid state is determined by minimizing the free energy with respect to σ_1 and σ_2.

The phase diagrams are then constructed by directly comparing the free energies of the solid phases (We consider face-centered-cubic (fcc) and body-centered-cubic (bcc) substitutional alloys in this paper) to that of the fluid phase. The details of the approach are described in Ref. 5.

Results

We plot the freezing densities of mixtures with actual particle diameter ratios ranging from .9 to .7 in Figure 1(a)-(d). For all the cases shown, the large particles have a radius $a_1 = 545$ Å and a surface charge $Z_1 = 300$. For the small particles, we use the linear-diameter-charge relationship proposed by Pincus[6] to determine the charge for particles of a given size: $a_2 = 491$ Å, $Z_2 = 270$ in Figure 3(a); $a_2 = 445$ Å, $Z_2 = 245$ in Figure 3(b);

$a_2 = 409$ Å, $Z_2 = 225$ in Figure 3(c); and $a_2 = 382$ Å, $Z_2 = 210$ in Figure 3(d). The actual particle diameter ratio is .9 in Figure 1(a), .817 in Figure 1(b), .75 in Figure 1(c) and .7 in Figure 1(d), while the diameter ratio of the effective hard spheres is 0.96 in Figure 1(a), 0.92 in Figure 1(b), 0.89 in Figure 1(c), and 0.86 in Figure 1(d). One can see that as the particle diameter ratio decreased more from unity, the freezing curve in the D-x phase diagram began to show a maximum with respect to x. Note that there is indeed a weak maximum which occurs near $x = 0$ in curve (a) which may be better seen from the minimum in $\tilde{T} - x$ plane when we plot the effective freezing temperature in Figure 2. We define the effective temperature temperature $\tilde{T} = k_B T / (Z^2 e^2 / 4\pi\varepsilon_0\varepsilon a_s)$ where $Z = x_1 Z_1 + x_2 Z_2$ is the average charge and $a_s = D^{-1/3}$ is the average nearest distance between particles. The maximum becomes more pronounced as the diameter ratio is progressively decreased, which has been observed experiemntally.[7] As a result, the disordered crystalline alloy phase shrinks to small regions near $x = 0$ and $x = 1$ for the small particle diameter ratio as is shown in Figure 1 (c)-(d), in agreement with experiments.[7,8] Note that the solubility of small spheres in the crystals of large spheres is always larger than the solubility of large spheres in the crystals of small spheres. This feature is also seen in the recent density-functional calculations of binary hard spheres.[9] Also note that the solid-liquid phase boundaries in Figure 1(d) almost open up vertically at the high densities and the effective hard-sphere diameter ratio is 0.86 in this case. When the effective hard sphere diameter ratio decreases further, the solid-liquid phase boundaries rise even more sharply from $x = 0$ and $x = 1$ (not shown). We also plot the effective freezing densities for all four cases in Figure 2. As the particle diameter ratio becomes smaller, the minimum freezing temperature becomes deeper. We have shown elsewhere the minimum in the freezing temperature or the maximum in the freezing density is actually related to a eutectic and the dept of the extrema does reflects the difficulty of mixing the particles. This suggests that the Hume-Rothery rule[10] for metallic alloys which states that no substitutional alloys can be formed when the diameter of the two species differ for more than 15%. may be used in binary colloids only that the effective hard sphere diameters must be used for the miscibility criterion instead of the bare particle diameters.

Attractive Regime

For convenience, we only perform calculations on a 2-dimensional square lattice. Consider a *mixture* of N_1 particles 1 and N_2 particles 2 placed in a square lattice of area A. The number density of particles 1 is $c_1 = N_1/A$ and that of particles 2 is $c_2 = N_2/A$. The total particle number density is $c = c_1 + c_2$. We will take the area of a unit cell to be unity. Thus, $c = 1$ represents the case where the lattice is fully occupied. An unoccupied site represents the solvent. For the interactions, we assume that only nearest neighbors have non-zero interactions.

Simulations

Initially, we randomly distributed the N_1 particles 1 and the N_2 particles 2 in a $M \times M$ lattice with periodic boundary conditions. The random distribution is to mimic the initial

4

mixing in the experiments. The particles are then performing Brownian motion (random walk). A particle of the ith species moves one lattice constant after every $\tau_{D,i}$. However, the Brownian motion of a particle may be modified when the particle is in the vicinity of other particles. Such modification is incorporated in the simulations by the use of a Boltzmann factor. When a particle is attempting motion, the motion is achieved according to the probability $e^{-\Delta E/T}$, where ΔE is the energy change due to the motion. When two particles are adjacent to each other in the model, they can form a cluster and diffuse as a whole. The mobility of a cluster is roughly assumed to be inversely proportional to its mass. Except for this difference, a cluster is treated in the same way as a particle: the clusters are also performing Brownian motion and the motion is also modified by the Boltzmann factor. When two clusters collide, they form a larger cluster. A particle within a cluster can also unbind from its neighbors by thermal motion due to the finite attraction energy, leading to the fragmentation of the cluster. The unbinding of an ith-species particle takes place according to the rate $(1/\tau_{R,i})e^{-(\Delta E/T)}$, where ΔE again is the energy change associated with the process and $\tau_{R,i}$ is the time constant associated with the unbinding of the ith-species particles. For the modification of the Brownian motion and the unbinding process, we use the Monte Carlo method (the Metropolis algorithm). A more detailed description of the aggregation model is given in Ref. 2 and 11.

There are seven parameters in general in a binary aggregation model such as this, namely, the interactions E_{11}, E_{12}, and E_{22}, and the time constants $\tau_{D,1}$, $\tau_{D,2}$, $\tau_{R,1}$, and $\tau_{R,2}$. The parameter $\tau_{D,i}$, where $i = 1$ or 2, is related to the mobility of the particles while the parameter $\tau_{R,i}$ is the inverse of the unbinding attempt frequencies and is more related to the surface properties of the particles. In general, $\tau_{D,i}$ is different from $\tau_{R,i}$. The mobility of the particles 1 can also be different from that of the particles 2. Unless mentioned, in most simulations we use $\tau_{R,i} = \tau_{D,i} = \tau$. The choice of a different set of $\tau_{R,i}$ and $\tau_{D,i}$ will mainly affect the aggregation rate but not the qualitative behavior[2] and our choice for $\tau_{D,i}$ and $\tau_{R,i}$ in this paper is arbitrary. However, it is worth noting that a smaller value of $\tau_{D,i}$ may be interpreted as a larger particle mobility and a smaller $\tau_{R,i}$ as a larger relaxation rate. In the simulations, we monitor the cluster size of particles 1 as well as the effective mobility of all particles. The reported results are the average over 10 different runs for each case.

Results

In the experiments the first species always flocculates before the second species, indicating that the interaction between particles 1 is more attractive than that between particles 2 or that between particles 1 and particles 2. Since we are only interested in the qualitative behaviors, for convenience we choose E_{11} to be attractive and $E_{12} = E_{22}$ to be repulsive. In the following, the energies will be expressed in units of the room temperature T.

As an example of how the aggregation of the first-species particles changes with the density of the second-species particles, in Figure 3 we show the pictures of the systems taken at $t = 100\tau$ for three different particle-2 densities $c_2 = 0$, 0.122, and 0.245 with $c_1 = 0.245$ fixed. With the periodic boundary conditions, it is clearly shown that the largest cluster (the

darkened circles) in the system is larger in the mid particle-2 density than in the other two cases.

To show the time dependence of the N versus c_2 curve, we plot in Fig. 4a for $c_1 = 0.25$, $E_{11} = -1$, $E_{12} = E_{22} = 3$ at different times $t = 100\tau$, 400τ, and 1000τ. The calculations were done on a 20×20 lattice. For all cases, the curve shows a peak, consistent with the experimental observation.[12] Note that the peak of the curve shifts to a higher value of c_2 at a later time and at higher values of $c_2 > 0.2$, the initially small clusters grow with time. This kind of aging behavior has also been observed experimentally.[12] Also shown in Fig. 4b is the effective particle mobility μ_{eff} versus c_2 for the same system as in Fig. 4a at $t = 100\tau$, where μ_{eff} is defined as the average number of movements made per particle within a time interval $\Delta t = 2\tau$. One can see that as c_2 increases, the movement of a particle becomes more and more hindered. As a result, the effective mobility decreases. Thus, Figures 4 together indicate that the decrease in cluster size and the restabilization at high c_2 is a kinetic effect and hence can *not* be predicted by equilibrium calculations. For instance, if one waits long enough, one should always see that the curve N versus c_2 is going upward and should not bend over as it does at an earlier time as shown in Ref. 11. The maximum flocculation rate in the mixtures in the attractive regime implies a minimum green density in the colloidal processing.

Summary

We have studied the stability of a binary colloidal suspensions by explicitly taking into account the interparticle interactions. For the repulsive regime, we have determined the boundaries between the liquid phase and the disordered substitutional crystalline alloys for binary colloids by comparing the free energies of both the liquid and the solid phases. We have shown the following: (1) For binary charged colloids, the freezing density as a function of the number fraction has a maximum. The maximum freezing density occurs in small-particle rich mixtures and the maximum freezing density increases sharply with decreasing particle diameter ratio. (2) When the effective hard sphere diameter ratio is about 0.86 ~ 0.85, the solid-liquid boundaries rise almost vertically; the liquid phase is stable in most of the phase space except for small regions near the pure cases.

The fact that the fluid phase can be stable up to an especially high density in a binary colloidal suspension can be helpful in colloidal processing where a high green-compact density is desired. Indeed, this has been observed experiemtally: A suspension of bimodal particle distribution does have a lower viscosity[13] and does give a higher green density[14] than a monodisperse suspension.

For the weakly Attractive regime, we have used Monte carlo simulations to study the flocculation behavior of a binary suspension. (1) We have shown that upon the addition of particles 2, the flocculation rate of particles 1 has a peak with respect to the particle-2 concentration. (2) We have clearly shown the aging phenomenon occurring at high particle-2 concentrations, namely, the cluster size grows with time. Both (1) and (2) have been observed experimentally.[12] (3) Therefore, the restabilization at high particle-2 concentrations is due to slow kinetics, i.e., slow particle movements but not thermodynamic reasons. The maximum flocculation rate occurring in the mixtures in the attractive regime implies a

minimum green density in the mixtures in colloidal processing. Thus, the use of binary suspension in the attractive regime is not advantageous.

Acknowledgment

References

1. I. A. Aksay and R. Kikuchi, in *Science of Ceramic Chemical Processing*, ed. by L. L. Hench and D. Ulrich (John Wiley abd Sons, New York, 1986)
2. W. Y. Shih, I. A. Aksay, and R. Kikuchi, *Phys. Rev. A* **36**, 5015 (1987).
3. C. C. Furnas, *U. S. Bur. of Mines Res. Invest.* No. 2894 (1928)
4. A. E. R. Westman and H. R. Hugill, *J. Am. Ceram. Soc.*, **13**, 767 (1930).
5. W. Y. Shih, W.-H Shih and I. A. Aksay, *J. Chem. Phys.*, in press; and the references therein.
6. P. Pincus Invited Paper at March Meeting of the American Physical Society, Los Angeles, California, 1983 (unpublished).
7. P. M. Chaikin and P. A. Pincus, unpublished.
8. E. Liniger and R. Raj, *J. Am. Ceram. Soc.* **70**, 843 (1987).
9. J. L. Barrat, M. Baus, and J. P. Hansen, *Phys. Rev. Lett.* **56**, 1063 (1986).
10. W. Hume-Rothery, R. E. Smallman, and C.W. Haworth, *The Structure of Metals and Alloys* (The Metals and Metallurgy Trust, London, 1969).
11. J. Liu, W. Y. Shih R. Kikuchi and I. A. Aksay, to be published.
12. M. Yasreby, W. Y. Shih and I. A. Aksay, to be published.
13. K. P. Darcovich and I. A. Aksay, unpublished.
14. C. Han, I. A. Aksay, and O. J. Whittemore, in *Advances in Materials Characterization II*, edited by R. L. Snyder, R. A. Condrate, P. F. Johnson (Plenum Press. New York, 1985), p. 339.

Figure captions

Fig. 1. D-x phase diagrams of binary colloidal particles with diameter ratio ranging 0.9 - 0.7. a_1 = 545 Å, Z_1 = 300 for all cases, while a_2 = 491 Å, Z_2 = 270 in (a); a_2 = 445 Å, Z_2 = 245 in (b); a_2 = 409 Å, Z_2 = 225 in (c); and a_2 = 382 Å, Z_2 = 210 in (d).

Fig. 2. $\tilde{T}$ - x phase diagrams of binary colloidal particles. Curves (a)-(d) correspond to the freezing temperatures of Figures 1(a)-(d).

Fig. 3 Monte Carlo simulations at different densities of particle 2 (with periodic boundary conditions). "o" denotes a particle 1 and "x" denotes a particle 2. The darkened circles denote the largest cluster in the system. (a) c_2 = 0, (b) c_2 = 0.122 and (c) c_2 = 0.245. In all three cases, c_1 = 0.245, t = 100τ, E_{11} = -1, E_{12} = E_{22} = 3. Note that particles 2 remain dispersed while particles 1 are undergoing clustering and that the largest cluster size in (b) is larger than in (a) and (c).

Fig. 4 (a) The average cluster size N versus the particle-2 density c_2 at different time whose c_1 = 0.25, E_{11} = -1, and E_{12} = E_{22} = 3. Note that the cluster size increases with time and that the peak shifts to a higher value of c_2 at a later time. (b) The effective particle mobility μ_{eff} at t = 100τ is plotted versus c_2. Note that μ_{eff} decreases with increasing c_2. The smaller μ_{eff} at high c_2 is responsible for the decrease in flocculation rate.
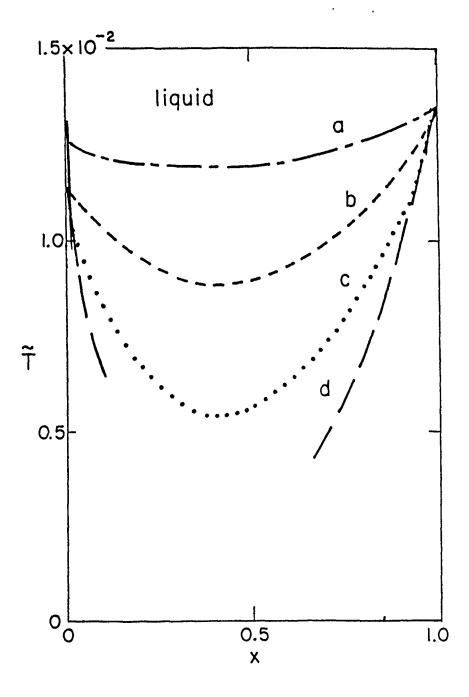
Fig.1

FIG. 2

(a)　　　　　(b)　　　　　(c)

Fig.3

(a)

$t = 1000\tau$

$t = 400\tau$

$t = 100\tau$

N

6.2

5.2

4.2

3.2

(b)

$\Delta t = 2\tau$
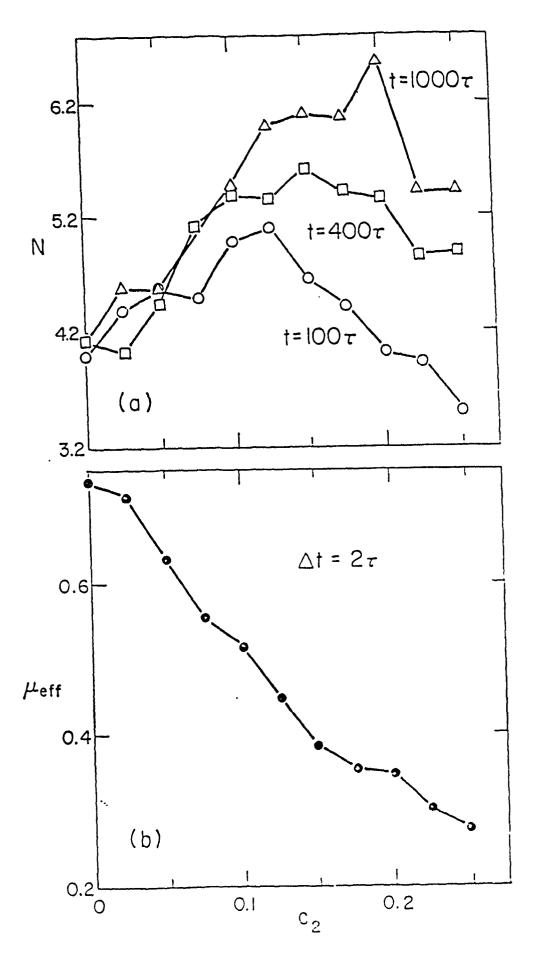
μ_{eff}

0.6

0.4

0.2

0   0.1   0.2 c_2
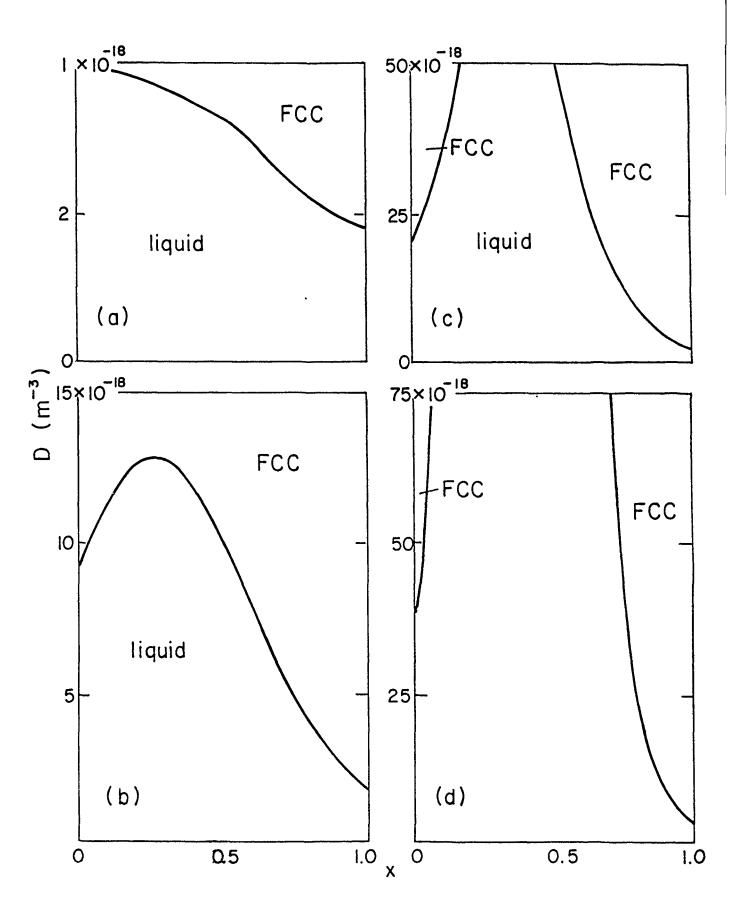
Fig. 4

APPENDIX VII

MECHANICAL PROPERTIES OF COLLOIDAL GELS

JUN LIU, WEI-HENG SHIH, WAN Y. SHIH, S. I. KIM, M. SARIKAYA, AND I. AKSAY
Dept. of Materials Science and Engineering
University of Washington, Seattle, WA 98195

Introduction

Colloidal processing of ceramics is becoming more important nowadays because of its better control on the microstructures of the green compact. Furthermore, the colloidal suspensions offer opportunity for a variety of techniques to improve the packing capability in the suspension stage. In general, a colloidal suspension can be either dispersed or flocculated depending on the interaction between the colloidal particles. If the interaction is repulsive, particles can relax to the minimun in their potential due to neighboring particles and the system can reach an equilibrium dispersed state. In the case of attractive interaction, particles form aggregates before they settle on the bottom of the container. As the concentration of particles is increased, the overcrowding of the aggregates produces a continuous network throughout the solvent before they settle and a colloidal gel is formed. A major difference between a colloidal gel and a colloidal suspension is that the gel can sustain finite stress and is therefore viscoelastic. Previously we studied the storage modulus and the yield strain of boehmite gels and found they are related to particle concentrations in a power-law fashion. We developed a scaling theory which successfully explains the experimental results on boehmite gels. The theory predicts that there are two types of power-law behavior depending on the relative elastic strength of the clusters and the links between clusters within the gel network. It is also predicted that there can be crossover phenomenon from one type of behavior to the other as we vary the particle concentration. In this paper we did dynamical rheology study on silica gels and demonstrate the crossover behavior, in good agreement with the theory. Furthermore, we found that depending on adding surfactant or not, we may have two types of mechanical behavior of colloidal gels. (1) Hard gels: in this type of gels the storage modulus G' increases with the particle volume fraction in a power-law fashion as described by the scaling theory. (2) Soft gels: the G' in this case increases with concentration in an exponential fashion. Monte carlo simulation on the restructuring of clusters shows exponential relationship between the largest cluster size and the concentration indicating that the exponential behavior in G' may be due to the restructuring of clusters. The exponential behavior of G' with respect to particle concentration is similar to the behavior of cake density as a function of applied pressure in pressure filtration suggesting that the pressure filtration behavior is also due to restructuring in the particle network. In the following we briefly summarize our theory on the elastic constant and yield strain of colloidal gels, followed by the experimental results on silica and boehmite gels. Finally, we end with some discussions and conclusions.

Scaling theory

A scaling theory is developed to correlate the elastic constant and yield strain of colloidal gels to their structures[1]. Here we briefly summarize the important results of the theory and refer to reference 1 for more detailed description of the theory. The theory is based on the fact that in the dilute regime of flocculated systems there are isolated clusters which are fractal objects with fractal dimension D. As the concentration of particles increases those individual clusters begin to overlap and eventually form a continuous network before they settle to the bottom of the container. In a simple approximation we may view the continuous gel network as a system of uniform-size clusters closely packed together. A schematic representation of a gel structure is shown in Fig.1a and a TEM micrograph of a silica gel is shown in Fig.1b for comparison. The model structure is similar to the TEM picture and contains the essential feature of a gel structure. The average cluster size ξ is related to the particle volume fraction φ as

$$\xi \sim \varphi^{1/(D-d)} \tag{1}$$

where d is the Euclidean dimension of the system. The above relation has been shown experimentally to be correct for silica gels[2].

The elastic constant of a cluster K_ξ is dominated by the bending constant between two bonds connected to the same particle and is related to ξ as

$$K_\xi \sim K_0 / \xi^{2+x} \tag{2}$$

where K_0 is the local bending constant between two adjacent bonds and the exponent x is the fractal dimension of the elastic backbone[3]. The macroscopic elastic constant K is related to the K_ξ as

$$K \sim (L/\xi)^{(d-2)} K_\xi \tag{3}$$

where L is the sample size. We now need to divide our discussion into two situations in which the elastic constant of the link between the clusters K_l is larger or smaller than K_l. In the strong-link regime in which $K_l > K_\xi$,

$$K \sim \varphi^{(d+x)/(d-D)} \tag{4}$$

whereas in the weak-link regime in which $K_\xi > K_l$,

$$K \sim \varphi^{(d-2)/(d-D)} \tag{5}$$

The yield strain γ_y of a colloidal gel can also be obtained by studying the bond-breaking of the weakest bonds in the network. For the strong-link regime,

$$\gamma_y \sim \varphi^{-(1+x)/(d-D)} \tag{6}$$

while for the weak-link regime,

$$\gamma_y \sim \varphi^{1/(d-D)} \tag{7}$$

As is clear from the above equations, the scaling behavior of the elastic constant and the yield strain is very different between the two regimes. In the strong-link regime the elastic constant increases with concentration with a larger power than in the weak-link regime. The yield strain decreases with increasing concentration in the strong-link regime whereas the yield strain increases with concentration in the weak-link regime. The crossover from the strong-link behavior to the weak-link behavior could occur as concentration is increased since increasing concentration reduces the average cluster size and making K_ξ larger.

Experiment

Silica gels are prepared from Ludox Colloidal Silica H30. The particle size is 12 nm and the as received suspensions are electrostatically stabilized. Two types of sample are prepared. In the first type which we called hard gels, the pH of the suspensions is adjusted to 9.5 and the suspensions are mixed with KCl. The particle concentration is adjusted to predetermined value (0.65% to 11.25%) and the KCl concentration is set at 0.25M. In the second type of samples which we called soft gels, the suspensions are adjusted to pH = 2 first and then the nonionic surfactant Octyphenol is added such that the surfactant to particle concentration is 15.64% by weight. The gels are grown in situ within the test fixtures to prevent disturbance and the growth of gels takes 10 minutes to 1 hour.

Two types of test fixtures are used in the dynamic rheological study using Rheometrics Fluids Spectrometer (RFS-8400). In the couette fixture, the gels are grown between two cylinders with a gap of 1 mm. We exert torsional stress on the outside cylinder and measure the response of a torsion wire attached to the inner cylinder. In the parrallel plate fixture, the gels are grown between two parrallel disk with diameter 25 mm and the gap between the disks is between 1 to 2 mm. When the bottom disk is stressed, the dynamic response of the sample is obtained by looking at the torsion wire attached to the upper disk. A dynamic oscillatory strain is imposed on the system by either rotating the bottom disk or outer cylinder with certain frequency and amplitude. The frequency of the oscillation is fixed at 1 rad/sec and the amplitude is varied over a range from 0.1% to 50%. The viscoelastic properties of the gels are characterized by the storage and loss moduli, G' and G''. We focus our attention to the storage modulus G' in this study.

The storage and loss moduli G' and G'' as a function of particle volume fraction for silica gel without surfactant is shown in Fig.2. There is a clear crossover behavior in G' at higher volume fraction. We interpret this as the crossover from the strong-link behavior to the weak-link behavior as predicted by the theory. Furthermore, the slopes of the weak-link regime is indeed much smaller than the strong-link regime. An additional proof of the weak-link behavior is shown in Fig.3 in which the storage modulus as a function of

the strain amplitude for several volume fractions of silica gel is presented. As can be seen from the figure the constant G' region decreases in the strong-link regime and it begins to increase in the weak-link regime. The behavior of the G' can be fitted to

$$G' \sim \varphi^5 \tag{8}$$

in the strong-link regime and

$$G' \sim \varphi^{1.2} \tag{9}$$

in the weak-link regime with an error of 0.2 since we have only four data points. Using the results of the scaling theory we calculated $D = 2.17$ and $x = 1.17$. We also did some preliminary light scattering studies on the diluted samples and found D to be between 2. and 2.2. The present results are consistent with the light scattering results.

Adding surfactant to the silica suspensions greatly changes the behavior of G'. The G' of silica gels with surfactant as a function of particle volume fraction is shown in Fig.4. The data can not be fitted to a straight line in a log-log plot indicating that it is not power-law behavior. The behavior of G' can be described by

$$G' \sim \exp(\alpha\varphi) \tag{10}$$

with $\alpha = 13.48$ with unit $\ln(dyne/cm^2)$ rather well.

Discussions and Conclusions

The exponential behavior of G' as a function of particle volume fraction is probably due to the restructuring of the clusters before they form the network since the attraction between particles is probably due to the interaction among the hydrophobic segments of the surfactant and those interactions are weak. With restructuring, there will be a distribution of cluster sizes within the gel network. The mechanical behavior of the network will be dominated by the weakest cluster which is also the largest cluster in the network (see equation (2)). A possible explanation of equation (10) is that equation (1) no longer holds for the largest cluster ξ_{max} and is replaced by an exponential relation

$$\xi_{max} \sim \exp(-a\varphi) \tag{11}$$

To see whether this is true, we did Monte Carlo simulation on the aggregation of particles and clusters with restructuring [4]. Both particles and clusters are allowed to move according to the relation between diffusivity and cluster size. In the present calculation, the diffusivity is assumed to be independent of the cluster size. Fig.5 shows the largest cluster size as a function of concentration in the dilute regime. The largest cluster size ξ_{max} is found to be related to the concentration exponentially,

$$\xi_{max} \sim \exp(b\varphi) \qquad (12)$$

This result suggest that at higher concentration when overlapping among clusters occur, equation (11) may be expected, leading to equation (10).

The exponential behavior of G' as a function of concentration provides a basis for understanding pressure filtration. In pressure filtration of colloidal suspensions, a typical particle volume vs. pressure curve is shown in Fig.6 for alumina. For dispersed state, the final density is high and is insensitive to the applied pressure. While for flocculated states, the final density is usually a logarithmic function of the applied pressure,

$$\varphi = A\ln(P) + \varphi_0 \qquad (13)$$

where A is slope and Φ_0 is some constant. This equation can be inversed to be

$$P = \exp(\varphi - \varphi_0/A) \qquad (14)$$

which is essentially an exponential relation between pressure and concentration similar to the behavior of G'. It suggests that the pressure filtration behavior is probably due to the restructuring of the network under pressure.

In conclusion, two types of elastic behavior of collidal gels are found: hard gels and soft gels. In the case of hard gels, there are two regimes that need to be specified depending on the relative elastic strength of the clusters and the link between clusters. The storage modulus G' increases with concentration in a power-law fashion in both regimes but with a larger exponent in the strong-link regime than that of the weak-link regime. The yield strain decreases with concentration in the strong-link regime whereas it increases in the weak-link regime. There is a crossover from the strong-link behavior to the weak-link behavior as we increase the concentration. These theoretical predictions are shown to be true in the rheological study of silica gels. In the case of soft gels in which surfactant is added, the power-law behavior of G' with concentration changes to exponential. Monte Carlo simulation results on restructuring of clusters indicates that the exponential behavior is due to the restructuring of the clusters. Our results imply that the pressure filtration behavior of colloidal suspensions can be understood in terms of the restructuring of the particle network.
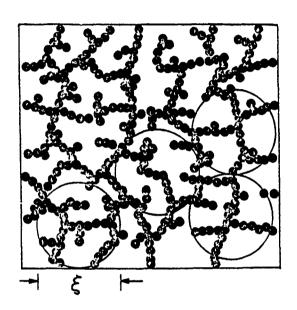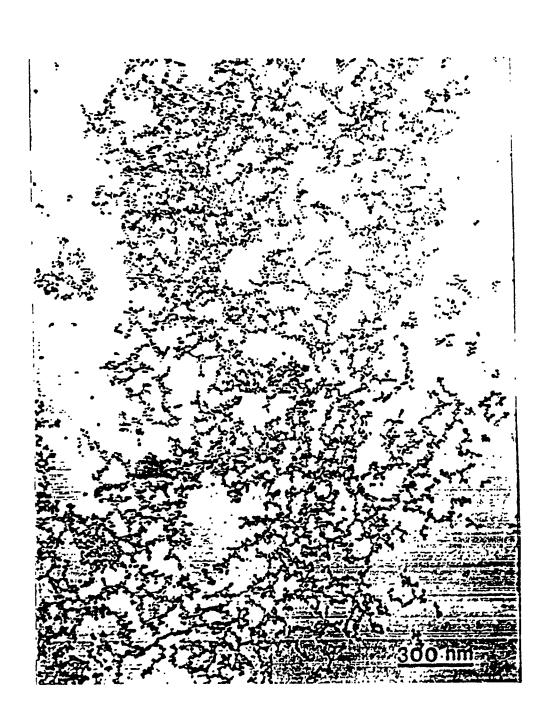
Acknowledgment

References

1. W.-H. Shih, W. Y. Shih, S. I. Kim, I. A. Aksay, preprint.
2. G. Dietler, C. Aubert, D. S. Cannel, and P. Wiltzius, *Phys. Rev. Lett.*, **57**, 3117 (1986).
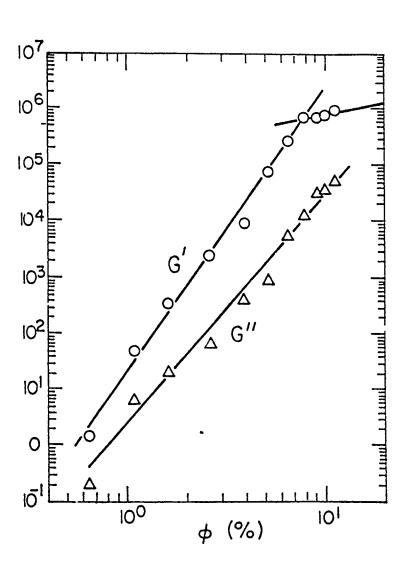3. Y. Kantor and I. Webman, *Phys. Rev. Lett.*, **52**, 1891 (1984).

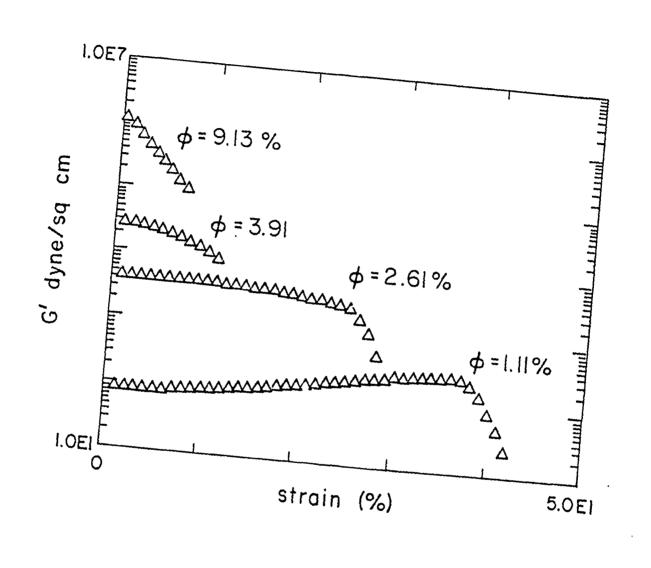4. W. Y. Shih, I. A. Aksay, and R. Kikuchi, *Phys. Rev. A* , **36**, 5015 (1987).
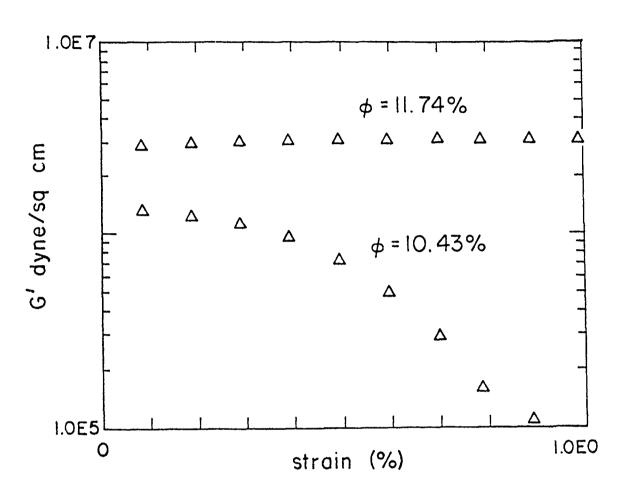
FIGURE CAPTIONS

Figure 1   The schematic structure of a gel network is shown in 1a in which some clusters with average size ξ are circled. 1b shows TEM microgragh of a typical silical gel.

Figure 2 G' and G'' of silica gels at pH = 9.5 as a function of particle volume fraction φ. A clear crossover occurs at around $\varphi = 10\%$.

Figure 3   The storage modulus G' of silica gels as a function of the strain amplitude γ for various concentrations. 3a shows results in the strong-link regime in which γ_y is shrinking with increasing concentration. 3b shows results in the weak-link regime in which γ_y increases with concentration.

Figure 4 G' of silica gels with surfactant added as a function of particle volume fraction φ.

Figure 5   The largest cluster size ξ_{max} as a function of particle concentration in the dilute regime.

Figure 6   The cake density as a function of the applied pressure in pressure filtration for alumina at pH = 3, 7, 7.5, and 8.

300 nm

DENSITY (%)

APPLIED PRESSURE (PSI)

pH
3.0
7.0
7.5
8.5
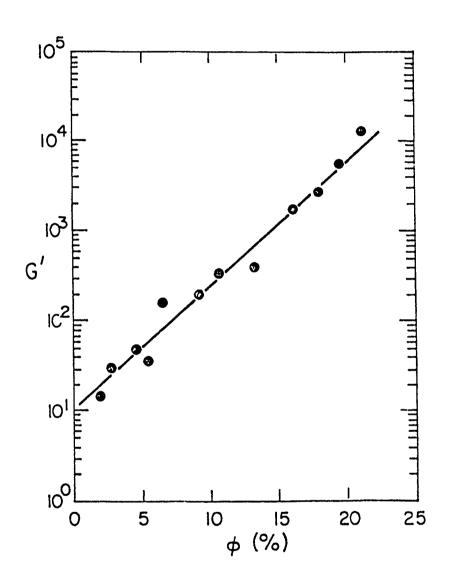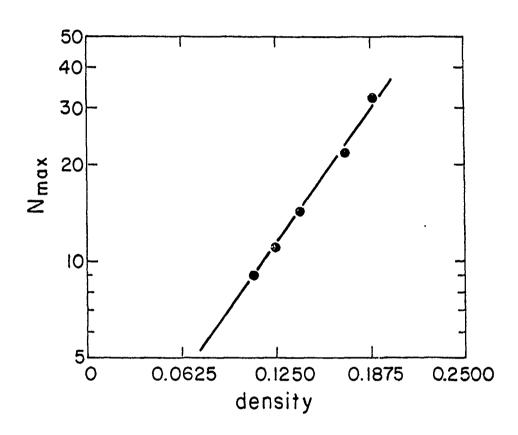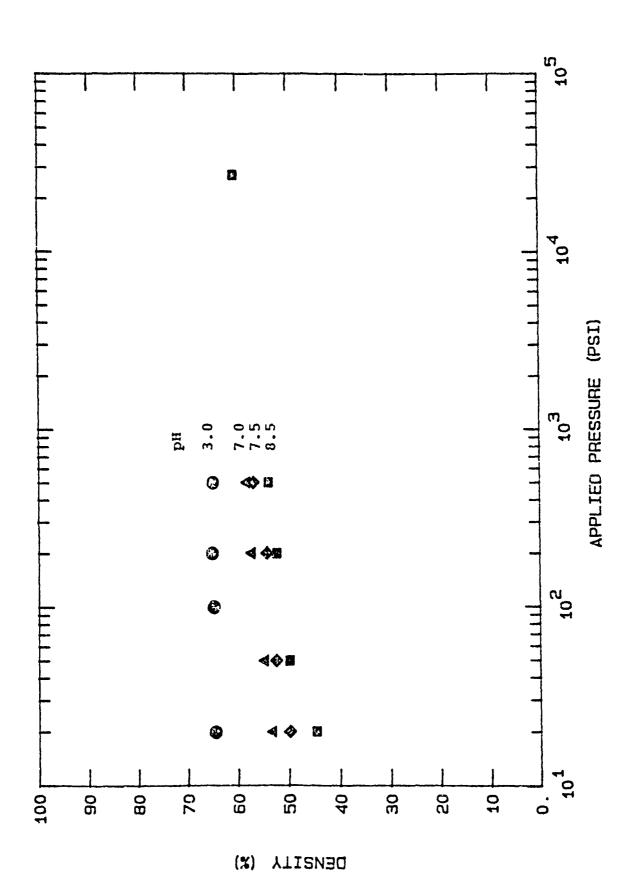
APPENDIX VIII

REMOVAL OF PROCESSING AIDS FROM CERAMIC/POLYMER COMPOSITES

GREGORY C. STANGLE, DONG-JOO RHEE, AND ILHAN A. AKSAY
Materials Science and Engineering, University of Washington, FB-10, Seattle, WA (195

ABSTRACT

Fundamental issues in the removal of processing aids from ceramic compacts prior to sintering have been investigated, both experimentally and theoretically. A general theoretical model has been developed that couples simultaneous momentum, heat, and mass transfer phenomena in disordered porous materials with the mechanical response predicted by an appropriate poroelasticity theory for partially saturated porous granular materials. The kinetics of pyrolytic degradation of organic processing aids were studied using a thermogravimetric analysis-mass spectrometry (TG-MS) system. Taken together, the modelling and reaction kinetics information can be used to predict internal stresses (that may compromise mechanical integrity) during removal of processing aids from the body. Agreement between simulated and experimental results is good.

INTRODUCTION

Success in the development of high-performance, high-reliability structural ceramics will be achieved only when a fundamental understanding of the effects of processing steps upon properties of the final ceramic body is achieved. Net shape or near-net shape forming of flaw-free, uniform, and homogeneous bodies must be possible for commercial applications (e.g., heat engine components) to be realized. Fabrication of ceramics by injection molding techniques is a favored approach, since this technique offers the advantages of production of complex shapes and of high rates of automated production. [1,2] This approach consists of dispersing the powder and processing aids in a binder, injection molding, debindering, and densifying.

Following consolidation and prior to sintering, it is necessary to remove various processing aids from the consolidated green body. This might include the organic vehicle used in dispersion, polymeric dispersant, and various binders, plasticizers, and lubricants. Approaches to the removal of processing aids include thermal degradation [3,4], chemical degradation [5], evaporation or sublimation at ambient or reduced pressures, [6] solvent extraction, [7] and capillary action. [8] Thermal (or thermal plus chemical) methods are often preferred. [3] The underlying goal of any scheme to remove processing aids is to reproducibly fabricate a debindered ceramic compact with microstructural uniformity. Proper debindering studies, therefore, require a combined experimental and theoretical effort to develop a fundamental understanding of the mechanisms involved in binder removal.

This paper summarizes the theoretical studies of the removal process, which include the movement of energy and material into and out of the green body, as well as the material response to internal stresses generated during the removal process. Experimental polymer degradation studies complete the picture by supplying necessary reaction rate data.

1

MOMENTUM, HEAT, AND MASS TRANSFER

Theoretical studies of the debindering process were undertaken in order to develop predictive capabilities in the design of an improved debindering process. Further, the design of experimental debindering studies can be improved since a theoretical model, once developed and verified, can test a much larger array of variables in less time than an analogous experimental approach. The theoretical model developed describes the simultaneous momentum, heat, and mass transfer with chemical reaction in a disordered porous medium. Table I summarizes the various processes responsible for the redistribution of material and energy into, out of and within the body during the removal process. Where appropriate, the driving force for the process and the transport coefficient are listed.

Special care must be taken, of course, when specifying transport coefficients in random "composite" materials of this nature. Figure 1 schematically illustrates this
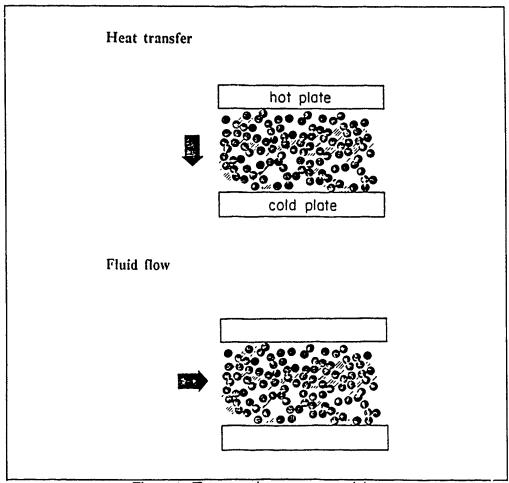
Figure 1. Transport in porous materials

point. Heat transfer between the hot and cold plates depends on the amount of each phase (gas, liquid and solid), the thermal conductivity of each phase, and the *specific spatial arrangement* of the materials between the plates. Similarly, fluid flow through such a "composite" is restricted to *available pathways*. Gas may flow (or diffuse) only through a connected network of liquid-free pores that "communicates" with the surface of the sample. Volumes occupied by solid and liquid are obviously eliminated from the allowable pathway, but so are bubble-like regions of gas that are completely enclosed by liquid and solid and thus unable to communicate with the surface of the sample. Allowable pathways for liquid flow

are restricted to continuous, connected networks of liquid-phase material, such that islands of liquid are incapable of capillary flow. A suitable approach is to estimate effective transport coefficients based on percolation concepts as applied to disordered media. [9-12]

The more generalized form of transport equations [12,13] has been reduced to the appropriate form by Stangle and Aksay [14] for the present problem. Energy, momentum and mass balance equations form a set of highly non-linear partial differential equations, to which the usual initial and boundary conditions apply. [14] External heat and mass transfer coefficients take into account the change in conditions external to the ceramic green body during the removal process. A fully explicit finite difference technique [15] was used for solution. Profiles of temperature, gas- and liquid-phase holdup, gas phase composition, and fluid velocities were predicted. Figure 2 shows a comparison of the simulated and experimental removal processes, (i.e., the removal of paraffin wax from an α-Al_2O_3/paraffin compact) wherein parameters for simulation were determined a priori. Good agreement is seen.
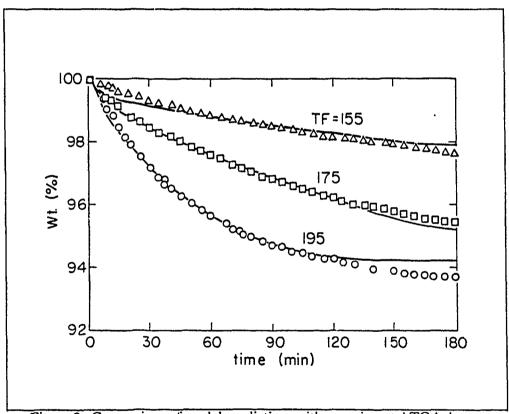

Figure 2. Comparison of model predictions with experimental TGA data.
From ref. [14].

POLYMER DEGRADATION KINETICS

Degradation of polymers by thermal and oxidative mechanisms is well documented in the literature. [5,16-18] Thermal degradation may take place by one or both of the following mechanisms: (a) depolymerization, whereby the backbone of the polymer is broken, effectively "unzipping" the polymer, or (b) removal of polymer side groups by substitution or rearrangement processes. The former mechanism results in a decrease in molecular weight of the polymer and may leave a wide or narrow molecular weight distribution of fragments.

depending upon whether the depolymerization takes place at random sites or at regularly spaced sites possessing high reactivity. The latter mechanism has little effect upon the molecular weight of the polymer. Many oxidative degradation mechanisms exhibit results similar to those of thermal degradation by depolymerization, usually differing only in the "point of attack" on the polymer chain and the oxygen-content of the resulting species. Oxidative degradation is usually more highly exothermic than thermal degradation. Two factors that are most important to the debindering of consolidated ceramic compacts are the rate at which the polymer is broken into fragments and the size of the resulting fragments. The first factor may cause the process to fall into the kinetic-limited regime, while the second influences volatility and diffusivity and hence may cause the process to fall into the diffusion-limited regime.

A thermogravimetric analysis-mass spectrometry (TG-MS) system was used [19,20] since (i) use of the TGA alone does not provide information about evolved gases, and (ii) TGA-GC and TGA-FTIR do not provide real-time data acquisition and molecular weight distributions, respectively. Only TG-MS provides simultaneous monitoring of sample weight and complete gas-phase composition (functional group analysis and molecular weight distribution) in a real-time sampling/analysis mode. Figure 3 shows the TGA data for identical samples of paraffin wax heated in different atmospheres (air and N2), while Figure 4 shows the mass spectra of gaseous material evolved from the samples at 80% weight loss, as detected by a triple-quadrapole mass spectrometer using an atmospheric pressure chemical ionization detector. Pyrolysis atmosphere is seen to have a profound effect on the mean fragment size and on the width of the fragment distribution.
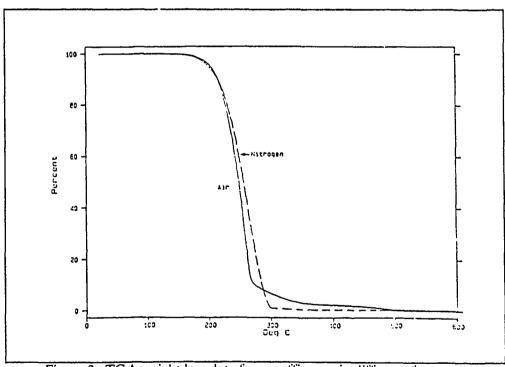

Figure 3. TGA weight loss data for paraffin wax in different furnace atmospheres.
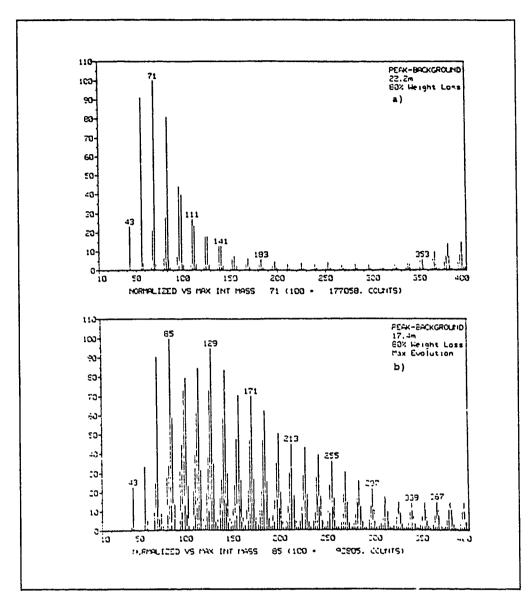
Figure 4. Mass spectra at 80% weight loss in (a) N_2 snf (b) air.

The implications of these results on the success of the removal process are twofold: (i) effective diffusion coefficients of larger molecules are lower than smaller molecules, thus reducing diffusive flux of the larger species out of the sample; and (ii) production of a larger number of smaller species may increase internal gas-phase pressure, which is particularly important in the pore space of fine-grained samples that have low effective gas-phase permeability. Both may lead to failure of the sample if the gas-phase contribution to internal stresses causes local stress values to exceed some failure criterion.

MECHANICAL RESPONSE

The mechanical response of the compact throughout most of the removal process (constitutive relationship and failure criterion) is quantified by applying appropriate poroelasticity theory to this rather "complex" partially saturated porous granular material. The geophysics and geomechanics literature is literally littered with treatments of important geological materials that are highly anisotropic and very heterogeneous, and may contain a number of solid-phase and fluid-phase materials. [21-24] A usual approach to the problem is to separate the contribution of each phase's stress to the total stress at a point. Such total stresses are related to the degree of deformation by constitutive relationships that include solid particle, drained skeleton, and liquid- and gas-phase compressibilities. Redistribution of gas, liquid, and solid may be retarded by drag forces between phases, thereby modifying mechanical response of the material. In addition, such variations in temperature as occur during the removal of processing aids require an inclusion of temperature-dependence in the relationship. Finally, a failure (or material strength) criterion is available from either micromechanical or empirical points of view [21-23]; the former can be more cumbersome than the latter but eliminates many of the simplifying assumptions required by the latter.

Figures 5 and 6 illustrate the relationship between the temperature (T_f) at which the removal process takes place, the liquid saturation (U) profiles, and internal stress distributions. [14] For T_f = 155°C (Fig. 5), the liquid saturation decreases steadily as a function of time and evenly as a function of position. For T_f = 230°C, on the other hand, Fig. 5 shows predictions of nonuniform saturation and thus relatively steep liquid gradients, particularly between U(0) I 0.70 and U(0) I 0.40, where U(0) is the value of U at the center of the sample. Calculation of the stress profiles for both cases was undertaken, and showed the largest tensile stresses occur at the surface of the sample. This is significant since it is known that (i) partially saturated granular materials are much weaker in tension than in compression and (ii) failure (that is, cracking and other permanent microstructural deformation) can occur if any component of stresses locally exceeds the tensile strength of the material. [25] Curves (a) and (b) in Figure 6 illustrate the significant differences in tensile stress buildup and decay for T_f = 230°C and 155°C, respectively. The magnitude of the surface tensile stress thus results from the steepness of the liquid saturation profile, which in turn derives from the relative rates of (i) convective mass transfer from the surface and (ii) that of capillary liquid flow that replenished the "drier" surface region. These relative rates, furthermore, depend fundamentally on the pore-space topology and the conditions to which the sample is subjected.
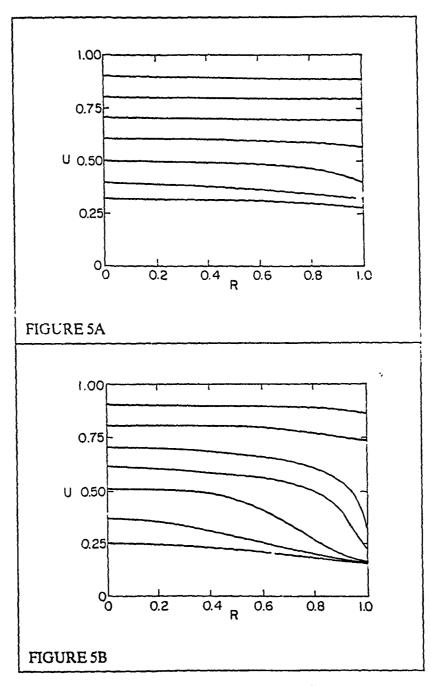
FIGURE 5A

FIGURE 5B

Figure 5. Liquid saturation profiles at (a) $T_f = 155^{\circ}C$ and (b) $230^{\circ}C$. By definition: $R = r/r_p$ = dimensionless radial coordinate; U = dimensionless saturation parameter ($U = 1$ when pores are full, and $U = 0$ when empty); and $\tau = \alpha_s t/r_p^2$ = dimensionless time. The quantities r_p and α_s are sample radius and thermal diffusivity, respectively.
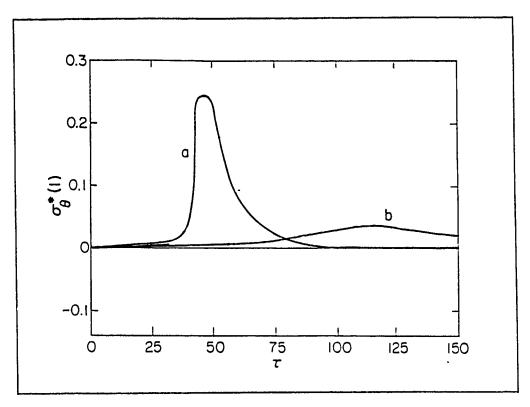
Figure 6. Internal stress profiles corresponding to saturation profiles in
Figure 5.　　(a) $T_f = 230^\circ C$; (b) $T_f = 155^\circ C$

CONCLUSIONS

The results of a combined theoretical and experimental study of the removal of processing aids from ceramic/polymer composites have been presented. Appropriate transport phenomena in disordered porous materials were modelled, with microstructural effects accounted for explicitly and quantitatively. The kinetics of pyrolytic degradation of the nonceramic processing aids was investigated with the TG-MS technique, and showed marked differences in the time-temperature-composition behavior of both solid and gas phases during decomposition. Poroelasticity theory provided a basis for quantifying the stress-strain-failure relationship. Predictions were verified by comparison with experimental removal processes. The verified theoretical model can thus be employed to improve (and possibly optimize) processing conditions in the removal of processing aids from a consolidated ceramic green body.

ACKNOWLEDGMENTS

REFERENCES

1. M. J. Edirisinghe and J. R. G. Evans, Int. J. High Tech. Ceram., 1, 1 (1986).
2. M. J. Edirisinghe and J. R. G. Evans, Int. J. High Tech. Ceram., 2, 249 (1986).
3. B. C. Mutsuddy, Proc. Brit. Ceram. Soc., 33, 117 (1983).
4. A. Johnsson, E. Carlstrom, L. Hermansson and R. Carlsson, Proc. Brit. Ceram. Soc., 33, 137 (1983).
5. L. Reich and S. S. Stivala, Elements of Polymer Degradation (McGraw-Hill, New York, 1971).
6. R. E. Weich, U.S. Patent 4,305,756 (15 Dec. 1981).
7. M. A. Strivens, U.K. Patent 808,583 (4 Feb. 1959).
8. I. Peltzman and M. Peltzman, Interceram., 4, 56 (1984).
9. S. Reyes and K. F. Jensen, Chem. Eng. Sci., 37, 905 (1982).
10. G. K. Batchelor and R. W. O'Brien, Proc. Roy. Soc. Lond. A, 7, 179 (1974).
11. R. B. Stinchcombe, Phys. C: Solid State Phys., 355, 313 (1977).
12. R. B. Bird, W. E. Stewart, and E. N. Lightfoot, Transport Phenomena (Wiley, New York, 1960).
13. S. Whitaker, Adv. Heat Transfer, 13, 119 (1977).
14. G. C. Stangle and I. A. Aksay, Chem. Eng. Sci., submitted (1989).
15. B. Carnahan, H. A. Luther and J. O. Wilkes, Applied Numerical Methods (Wiley, New York, 1969).
16. R. T. Couley, ed., Thermal Stability of Polymers (Marcel Dekker, New York, 1970). See also J. Anal. Appl. Pyrolysis, 11 (1987).
17. A. D. Jenkins, ed., Polymer Science (North Holland, Amsterdam, 1972).
18. Y. Tsuchiga and K. Sumi, J. Polym. Sci., 40, 1723 (1985).
19. G. C. Stangle, R. B. Prime, D.-J. Rhee, J. C. Seferis, and I. A. Aksay, SPE Conf. Proc.: ANTEC 89 (1989).
20. G. C. Stangle, D.-J. Rhee, and I. A. Aksay, J. Am. Ceram Soc., submitted (1989).
21. J. G. Berryman and L. Thigpen, in Physics and Chemistry of Porous Media II, edited by J. R. Banavar, J. Koplik, and K. W. Winkler (American Institute of Physics, New York, 1987), p. 209.
22. I. Vardonlakis and D. E. Beskos, Mech. Mat., 5, 87 (1986).
23. D. F. McTigue, R. K. Wilson, and J. W. Nunziato, in Mechanics of Granular Materials: New Model and Constitutive Relations, edited by J. T. Jenkins and M. Satake (Elsevier, Amsterdam, 1983), p. 195.
24. M. A. Biot, J. Acoust. Soc. Am., 28, 168 (1956).
25. P. J. Sherrington and R. Oliver, Granulation (Heyden, Philadelphia, 1981), p. 19.

Table I. Processes Responsible for Redistribution of Material and Energy.

| PHASE | PROCESS | IMPORTANT QUANTITIES | |
		MATERIAL	ENERGY
Gas	Diffusion	Concentration gradient Effective diffusivity	-----
	Convection	Pressure gradient Effective permeability	Temperature, pressure gradients Effective permeability
	Evaporation	Vapor pressure	Heat of vaporization
	Chemical reaction(s)	Reaction rate(s) Concentration of reactant(s)	Heat(s) of reaction
Liquid	Convection	Pressure gradient Effective permeability	Temperature, pressure gradients Effective permeability
	Evaporation	Vapor pressure	Heat of vaporization
	Chemical reaction	Reaction rate(s) Concentration of reactant(s)	Heat(s) of reaction
Solid	Conduction	-----	Temperature gradient Effective conductivity

APPENDIX IX

POWDER PROCESSING--SCIENCE AND TECHNOLOGY

Ilhan A. Aksay and Gregory C. Stangle

Department of Materials Science and Engineering
Advanced Materials Technology Program, The Washington Technology Center
University of Washington
Seattle, Washington, U.S.A. 98195

ABSTRACT

The processing of ceramics with ultrafine (submicron) ceramic particles involves four key steps: (i) synthesis and/or refinement of raw materials, which may be in the form of powders, fibers, or whiskers; (ii) addition of a fluid phase and other processing additives to aid in the dispersion of colloidal suspensions and subsequent consolidation of the solid phase; (iii) removal of all nonceramic processing aids; and (iv) densification of the consolidated ceramic compact by sintering, which involves structure evolution and property development. Precise control of process parameters in these four steps can lead to the development of a new class of ceramic materials for electronic and structural applications.

要約
　サブミクロンの超粒子を用いたセラミックスの製造は、4つの重要な工程からなっている。1）粉末、繊維あるいはウイスカー状の原料の合成および精製、　2）コロイド懸濁液の分散、固化を助ける液体及び他の処理剤の添加、3）セラミックス以外の全ての処理剤の除去、及び4）固化したセラミックス成形体の焼結による緻密化で、それは微構造の発達および、特性の付与をもたらす。これら4工程のプロセスパラメター正確に制御することにより、新しいエレクトロ及び構造用セラミックスを発展させることができる。（図1）

1. INTRODUCTION

Near-net-shaping of monoliths with complex geometries with a precise control of structural features on all length scales may be achieved by better understanding and control of the four fundamental steps of the ceramic fabrication procedure: (i) synthesis or selection of the raw materials in powder form; (ii) consolidation of the powders by either wet (i.e., dispersion in a liquid medium) or dry methods; (iii) removal of all nonceramic processing aids; and (iv) densification of the consolidated ceramic powder compact by sintering (Figure 1).

The use of colloidal suspension techniques favors control of microstructural uniformity and the fabrication of complex geometries that cannot be easily accomplished by dry pressing techniques (1). Particularly in the case of ceramic powders in the submicron size range, colloidal techniques are essential in producing highly concentrated yet sufficiently fluid colloidal suspensions that are suitable for near-net-shape forming while simultaneously avoiding problems with undesirable agglomerate formation (Figure 2). These ceramic powder suspensions with high solids content but low viscosity are then consolidated into densely packed states. Achievement of higher powder packing densities results in attaining higher sintered densities at lower sintering temperatures and with lower shrinkages than could be achieved with lower packing densities (2). Thus, the present interest (3) in the colloidal approach to ceramics processing is mainly a consequence of the realization that unwanted inhomogeneities introduced into a compact during the presintering stages generally remain in the finished product as defects (4,5).

As a result of this renewed interest in the colloidal processing approach, significant contributions to the field have been made (6-12). In particular, the use of surface-active polymers and polydisperse particle systems have been employed in micrometer-sized particle systems to achieve highly concentrated, low viscosity suspensions that give high packing densities upon consolidation, but the difficulties increase as the particle size is reduced to the nanometer size range. Promising results have been obtained with the use of lubricating surfactants, where dense (> 60 v/o) nanoscale structures have been formed. In the remainder of this paper, we describe and critique the results of experimental and theoretical investigations of the preparation of ceramic materials by colloidal techniques. Although these recent findings agree for the most part with our experience in traditional (clay-based) materials processing, the new interpretations should lay the groundwork for future improvements in colloidal processes in the production of superior ceramics.

2. RAW MATERIAL SYNTHESIS AND REFINEMENT

Two criteria generally guide the choice of synthesis scheme: purity and particle size. A high purity starting material for producing advanced ceramics is often desired in order not to compromise various properties of the final product. The use of powders with particles in the submicron range is preferred in order to increase the driving force for densification and also to form fine-grain microstructures. Particle shape can also be an important factor. The choice of preparation route also depends upon the type of material and the economics of the process. Traditional preparation methods of milling and classification are inadequate for producing powders for advanced ceramics, and so novel synthesis schemes are being developed.
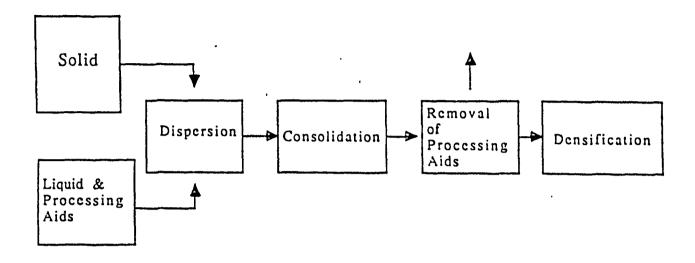
Figure 1. Sequence of processing steps taken in the ceramic fabrication process.

Powder synthesis involves the chemical conversion of a pre-ceramic compound to a ceramic compound. The system may be single phase (e.g., MgO production from $MgCO_3$) or multiphase (e.g., nucleation and precipitation from a fluid-phase mixture). Methods for production of powder include solution techniques (hydrolysis of metal-organic compounds, precipitation from solution, emulsion and microemulsion methods) and vapor-phase techniques (applications of chemical vapor deposition and plasma processing techniques, and various aerosol techniques) (13-15).

Hydrolysis of metal alkoxides has been used in an attempt to improve the purity of ceramic powders and to successfully achieve the mixing of pre-ceramic components on a molecular scale (16-22). The starting (monomeric) material is an organic compound that contains both the metal and at least two functional groups by which monomeric units can be joined during hydrolysis and polymerization. Precipitation techniques have been widely employed to prepare pure ceramic powders from salt solutions (23). Coprecipitation has been used to prepare multicomponent powders in our laboratory and elsewhere (24-26). Emulsion and microemulsion schemes are emerging as powder preparation methods. In both cases, a "water-in-oil" (W/O) dispersion is prepared wherein the aqueous phase is dispersed in an organic liquid and stabilized with the aid of an emulsifying agent. The aqueous phase contains dissolved preceramic components that form solid particles (27-34). Chemical vapor deposition and plasma processing techniques have been successfully applied in the preparation of fine, high-purity, unagglomerated particles with a fairly well controlled size distribution (13,26,35-39). They have been applied successfully to a variety of oxide and nonoxide materials (24). Particles as fine as 10 nm have been prepared by these techniques (40). Liquid aerosol powder production processes are discussed by Matejevic (41). In this procedure, an atomized metal-containing solution is introduced into a gas stream containing a reactant vapor. The subsequent
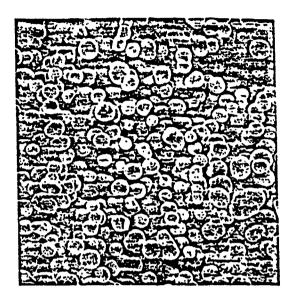
Figure 2. Scanning electron micrograph (SEM) of TiO$_2$ powder derived from TiCl$_4$

absorption with chemical reaction produces a solid powder. Powder purity can be high. Final particle size is related to solution droplet size.

The wide variety of powder synthesis and preparation methods discussed in this section provides many starting points in the ceramic fabrication process. Highly pure ceramic powders can be insured by carefully controlled synthesis routes. Surface properties, as well as particle size, size distribution and shape, can also be controlled with varying degrees of success, depending upon the chosen method. Since surface properties and particle size and shape strongly affect dispersion, rheology, and consolidation, densification and the final microstructure are significantly influenced by this initial fabrication process step.
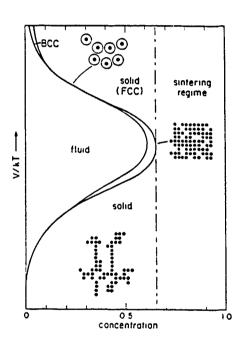
3. DISPERSION AND CONSOLIDATION

The use of powders in the submicron range is preferred in the fabrication of advanced ceramics, because of the effects of particle size and size distribution on sintering behavior and microstructural evolution. A significant difficulty which arises in employing submicron colloidal particles is their tendency to agglomerate due to interparticle attractive forces, particularly van der Waals. Such clustering leads to undesirable micro- and nano-structures and to highly viscous and viscoelastic suspensions. Subsequent densification may be impeded due to packing density variations. A process leading to the formation of a colloidally consolidated compact begins with the dispersion of the particles in a liquid medium. The dispersion process possesses a number of attractive features: poorly packed agglomerates can be removed by gravitational or centrifugal sedimentation; additional modifications of the particles' surface chemistry can be accomplished by using surface-active polymers and, for aqueous systems, varying pH and ionic strengths; and particles in multiphase systems can be mixed on a length scale equal to the size of the individual particle. Such modifications can produce highly concentrated yet sufficiently fluid suspensions

suitable for subsequent shape-forming (i.e., consolidation) processes. This section describes th · fundamental experimental and theoretical work performed on the dispersion and stability of submicron :c mic particles in suspension and on the consolidation of such suspensions. These results can be applied t. the improvement of techniques for obtaining higher packing densities and microstructural uniformity, and for fabricating complex geometries not otherwise attainable by alternative processing methods.

As in the atomic systems, equilibrium and nonequilibrium thermodynamic treatments have been used to describe the stability regions of fluid and solid phases in the parameter space of interparticle energy and particle number density (42-44). However, experimental observations have shown that colloidally consolidated systems always display hierarchically clustered nonequilibrium structures as a result of a nucleation and growth process of particle clusters (42). The most important consequence of this hierarchical clustering is that even in monosize particle systems, a monomodal void size distribution is never attained. When the first-generation particle clusters are at a packing density of 74%, the packing density of the second-generation clusters drops to an average value of at least 64% due to the bimodality of the void size distribution.
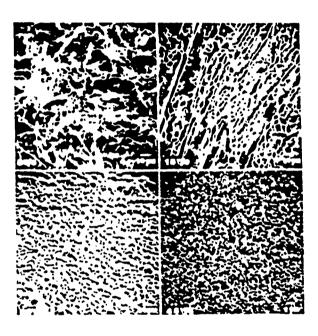

Figure 3: Schematic form of the nonequilibrium colloidal phase diagram. In the high V/kT region, the onset of fluid to solid transition shifts to lower concentrations due to increasing hydrodynamic radius. A similar trend is observed at the low V/kT region due to the formation of low density fractal clusters. Body centered cubic (bcc) packing of particles is observed with organic particles, but ceramic systems have only been observed with face centered cubic (fcc) packing (45,46).

Since these hierarchically clustered structures signify the formation of nonequilibrium structures, in Fig. 3 we suggest the form of a nonequilibrium phase diagram in a V/kT versus particle concentration space where V denotes the generalized interaction potential, k is the Boltzmann constant, and T is the temperature (46). The high V/kT region of this diagram outlines the equilibrium transitions observed in highly repulsive systems as detailed elsewhere (43). In electrostatically interacting systems, the onset of fluid to solid transition shifts to lower concentrations as the hydrodynamic radius of the particles increases with the development of an electrostatic repulsive barrier around the particles. In the low V/kT region, the onset of fluid-to-solid transition again shifts to lower concentrations because of the formation of low density fractal clusters (45,46). In highly repulsive systems, the hierarchy is observed only to the second order (Fig. 4(d)), whereas in highly attractive systems, as low density fractal clusters form, the order may

increase to the third or fourth level of hierarchy (Fig. 4(a)) (47). From a practical point of view, the conditions corresponding to the upper and the lower ends of this diagram must be avoided to obtain high packing densities in the casts and to minimize drying shrinkages. The middle range is most suitable for the preparation of high concentration slips that can be converted to high packing density casts with minimum amount of shrinkage. As an extension of this concept, the methodology of optimizing the processing conditions in this middle range to prepare highly concentrated colloidal suspensions will now be discussed.
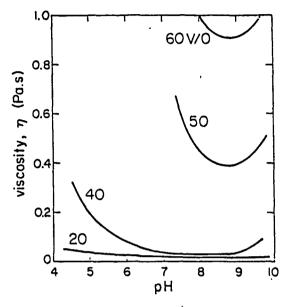
Figure 4: Electron micrographs of freeze-dried suspensions showing the arrangement of particle clusters in an aqueous α-Al_2O_3 (0.4 μm) system. Low density, higher order hierarchically clustered networks that form in highly attractive particle systems are shown in (a) 5%. (b) 15%, and (c) 30% solids contents. Pressure casting reduces the hierarchy to the second-generation level at 45% (d). Highly repulsive systems also result in microstructures similar to those of (d) (47).

Two basic approaches to increasing the solids loading of a suspension without increasing the viscosity above 1 Pa-s are now illustrated. The first method is based on the principle of hydrodynamic radius minimization, and the second method is based on the principle of space filling with multimodal particle systems. It is also important to note that neither of these methods is by any means novel. In clay-based technologies, both of these methods are routinely used to achieve high packing densities and to lower sintering temperatures (48,49).

One effective way of developing sufficient repulsive interaction between particles without increasing the hydrodynamic radius is through the steric repulsion of polymeric protective coatings. Industrial practice has shown that polyelectrolytes are especially useful in achieving this goal in aqueous systems. Following this trend, we have recently illustrated the effective use of a polymethacrylic acid (PMAA) polyelectrolyte with a model system of relatively monodispersed (0.4 μm) α-Al_2O_3 aqueous suspension (50). Fig. 5 shows that in highly concentrated (> 50 v/o) suspensions of PMAA coated α-Al_2O_3 suspensions stabilized with the PMAA polyelectrolyte (52). At a fixed solids content, nearly an order of magnitude decrease in the viscosity can be realized simply with the addition of smaller particles into a nearly monosize matrix. As we show in following sections, the addition of these small particles into a matrix provides clear advantages

over monosize particle systems in obtaining higher green densities and thus lower sintering temperatures with less grain growth.

Figure 5: Viscosity (at 9.3 s^{-1}) of aqueous α-Al$_2$O$_3$ (0.4 μm) suspension stabilized with a Na+ salt of PMAA polyelectrolyte as a function of pH from 20 to 60 v/o solids concentration.

Figure 6: Zero-shear viscosity of an aqueous α-Al$_2$O$_3$ (0.8 μm) suspension as a function of fraction of fines (0.18 μm) at a fixed solids loading of 50%.

The illustrations given above are for systems containing micrometer-size particles. When the size of the particles is reduced to the nanometer or the sol-gel processing range, the same degree of success is not obtained (Fig. 7) (46). The key unifying feature of both the nano- and the micro-meter range is that regardless of the particle size, the nucleation of particle clusters and their networks as hierarchically clustered structures takes place in both ranges. The extent of the hierarchy determines the overall packing density of the system (42). Our recent studies have shown that in the nanometer range the relaxation of these hierarchically clustered structures to higher densities does not readily take place (46). As a result, lower density gel structures are commonly observed (Fig. 8(a)). In contrast, when these nanometer-size particles are first coated with lubricating surfactants, we are able to form the close-packed structures as shown in Fig. 8(b) (53). This observation suggests the possibility of obtaining highly concentrated suspensions with nanometer-size particles, although practical applications have not yet been illustrated.
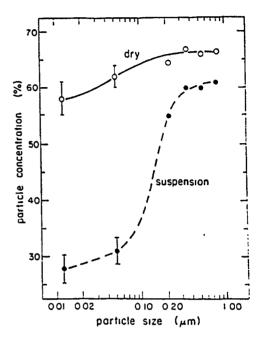
Powder Processing--Science & Technology

Figure 7: The effect of particle size on the maximum particle concentration of electrostatically stabilized suspensions of α-Al$_2$O$_3$ (> 1 μm) and AlOOH (< 1 μm) without exceeding a suspension viscosity of < 1 Pa·s. Notice the drastic change in the suspension concentration as the particle size falls below 0.1 μm (46).

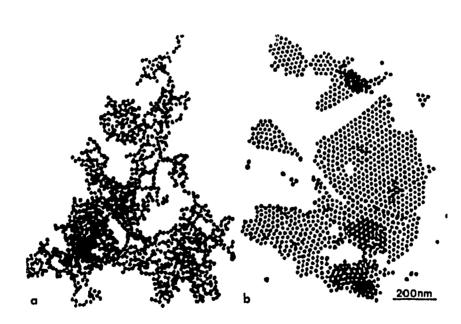Figure 8: (a) Fractal clusters of 15 nm gold particles that result in the formation of low density compacts; (b) The dense packing of the same gold particles after they are first coated with lubricating surfactants (53).

4. REMOVAL OF PROCESSING AIDS

Processing aids added to the suspension must be removed following consolidation of colloidal suspensions and prior to densification. These additives include material required for powder synthesis and preparation (e.g., residual carbonaceous components from the alkoxide hydrolysis route, surfactant from the microemulsion route) and powder dispersion (e.g., solvent, acid/base, salt, polymeric dispersant and possibly various binders, plasticizers and lubricants). This processing step is conducted at moderate temperatures and is usually completed upon reaching the temperature range of 600-700°C. In addition, certain preceramic materials require similar temperatures for conversion to the desired final ceramic compound, thus taking place simultaneously with the removal of processing aids.

Removal of liquid from the porous consolidated ceramic particle compact is commonly the first step in the removal of processing aids, and is achieved by evaporation and thermal and/or chemical degradation. The presence of a liquid phase can lead to significant capillary pressure as the initially liquid-filled pores are emptied, creating gas-liquid menisci. For small pores in the consolidated colloidal compact, the capillary forces can be quite large. Such forces can impose significant internal stresses in the compact, resulting in inhomogeneous shrinking and, ultimately, cracking of the body. The greatest concentration of internal capillary-induced stresses occurs at the location of the largest number of menisci, suggesting that the position and thickness of the drying front (i.e. the transition zone between liquid-filled and dry regions of the solid) are controlling factors in the design of a successful liquid-removal process. Shaw (54) employed invasion percolation concepts (55-58) to predict the morphology of the drying front observed experimentally in a pseudo-two-dimensional porous medium composed of submicron silica spheres. Scherer's series (59-63) of papers considers drying of pre-ceramic gels produced by hydrolysis of alkoxides in order to predict differential internal stresses that cause cracking during drying.
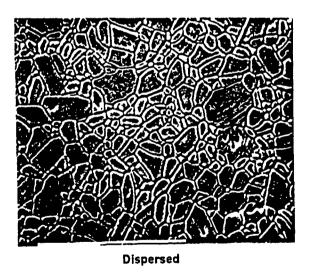
Removal of polymeric dispersing agents required for the production of stable colloidal suspensions and of binders, lubricants, plasticizers, and surfactants added in certain processing schemes is usually accomplished following removal of the solvent from the compact. Complete removal is necessary to prevent residual (usually carbonaceous) impurities from compromising ceramic powder purity during subsequent densification. In some ceramic body fabrication processes (e.g., injection molding) the "binder removal" stage can be the most critical step in the process (64). Recently, a number of studies have been reported (64-69) where oxidative and thermal degradation mechanisms were employed to carry out the removal of processing additives. Temperature history (initial and final temperature, ` .ing rate), polymer chemistry, furnace atmosphere, and ceramic powder microstructure were demonstrated to play important roles in the process. The additives must be removed under carefully controlled conditions so that the microstructure experiences minimal disruption (e.g., cracking, slumping, blistering, etc.) (69).
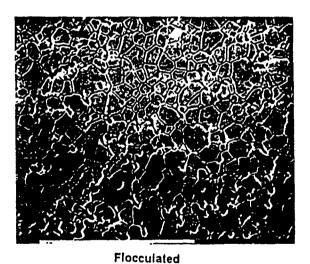
Partial pyrolysis of polymeric ceramic precursors (used as binder materials or as infiltrants) is an important consideration when producing single-phase or multiphase ceramics by either the metal alkoxide (16,17) or other pyrolyzable pre-ceramic polymers (70). For example, Walker et al (70) reviewed a number of ring and cage compounds that can be used to form ceramics of B_4C, BN, SiC, and Si_3N_4. References (6), (9) and (10) provide certain additional examples and more specific experimental details of the pyrolytic conversion of numerous polymeric ceramic precursor materials.

Powder Processing--Science & Technology

5. DENSIFICATION

Subsequent to the removal of processing aids, the consolidated ceramic green body is fully prepared for densification. In the sintering of consolidated ceramic powder compacts, microstructural inhomogeneities introduced during consolidation lead to variations in sintering kinetics and subsequent microstructural evolution: Figure 9 underscores this point. Particles that are more densely packed sinter to full density at a higher rate and at lower temperatures than do less densely packed particles. Three conditions must be achieved in the consolidated powder compact in order to sinter successfully at lower temperatures: small particle size, narrow pore size distribution, and uniform spatial distribution of pores. The effects of these parameters on sintering kinetics and microstructure evolution have been studied in detail and are described below.

A consolidated compact composed of smaller particles sinters more quickly and at lower temperatures than does a compact composed of relatively larger particles; this is due to a larger chemical potential in the former as a result of its smaller radius of curvature. Sol-gel processing employs submicron-sized particles and has advantages for reducing the sintering temperature and for preparing materials with high uniformity and purity compared to conventional processing. An investigation of the sintering and microstructure evolution of alumina and mullite-forming gels was undertaken in our laboratory. Enhanced densification and lower sintering temperatures were achieved when the dense particle packing of nanosized particles resulted in a relatively small pore size distribution. Slow drying of the gels was necessary to minimize anisotropic shrinkage of the gel prior to sintering.

Dispersed   Flocculated

1450°C - 1.0 Hour

Bar = 10.0μm

Figure 9. Effect of processing path upon microstructure of Al_2O_3 after densification by sintering for 1 hr. at 1450°C. Bar = 10.0 μm.

Powder Processing--Science & Technology

The study of the effect of pore size distribution upon sintering and densification behavior naturally follows from the work described in the previous paragraph. A model system was thus devised (19) to investigate microstructure evolution during sintering in a ceramic compact with a controlled pore structure. The approach was motivated by the space-filling concept, which suggests that the addition of fine particles in a coarse matrix results in the reduction of pore size and overall porosity. A colloidally consolidated ceramic compact was prepared from a suspension of particles with a bimodal particle size distribution. The packing density went through a maximum at an intermediate value for a volume fraction of fines (see Figure 10), thus suggesting an optimum amount of small particles that was required to occupy the void space between large particles.
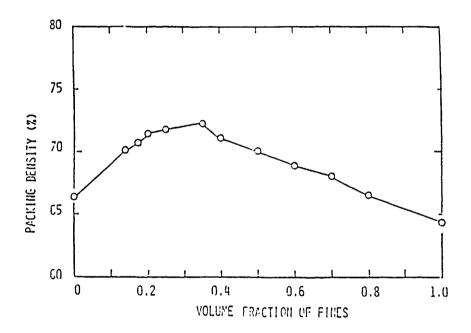

Figure 10. The variation of packing densities with fraction of fines.

As a result, the pore size distribution was smaller, which led to lower sintering temperatures and times. Grain growth was consequently reduced. The evolution of pore size distribution during densification was studied by mercury porosimetry, showing that bimodal compacts retained open pores at relatively later stages of sintering and thus reduced the sintering temperature and improved the degree of densification. This is most certainly at variance with the work of Bowen et al (71,72) and Ogihara et al (73), whose powder compacts contained a significant amount of second-generation voids. The advantage derived from employing a bimodal particle size distribution is that the width of the pore size distribution can be reduced by filling in the second generation voids with fine particles.

Powder Processing—Science & Technology

Microstructure evolution during sintering also involves particle rearrangement (74) and a change in particle size distribution (75). Lange & Kellett (74) discuss particle rearrangement during initial sintering stages. Neck growth between particles in contact during sintering creates stresses, resulting ultimately in anisotropic shrinkage of the sintered powder compact (see Figure 11). Complete pore closure can also be inhibited. Undesirable grain growth may also occur, which has been shown to be due to particle size and such pre-sintering microstructural characteristics as packing density and frequency of first-, second- and third-generation voids. Martin (75), for example, studied the sintering of a model monosized ZrO_2 compact. Fukuda et al. (76) have developed a model based upon statistical mechanical concepts to describe time-dependent processes such as grain growth or disappearance and grain-boundary exchanges during sintering.
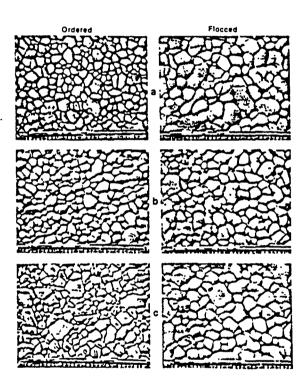

Figure 11. Micrographs of surface grain shapes for the 170 g ordered and flocced compacts sintered at 1150°C for (a) 10 minutes, (b) 2 hours, and (c) 10 hours (note scale changes).

The study of sintering (with attention paid to the influence of earlier processing steps) is of importance not only to ceramics with structural applications, but also to those applications for which electrical or optical properties are important. For example, the transparency of mullite to infrared radiation was shown to be dependent primarily on the purity and post-sintering microstructure (77). Mullite-forming gels were used to prepare monolithic ceramic bodies, which densified to nearly (98%) theoretical density at 1250°C. Infrared transparency depended upon 'pore-filling' (i.e., microstructure evolution) by viscous phase deformation of silica and subsequent crystallization of mullite during sintering. Infrared absorption analysis can thus in this case be used to characterize the completeness of chemical reaction, the nature of pore size distribution, and the degree of densification.

Powder Processing--Science & Technology

6. SUMMARY

Important investigations are being undertaken to fabricate ceramic matrix materials by colloidal consolidation techniques. Small, pure, unagglomerated particles for advanced ceramics cannot be prepared by traditional "crushing and grinding" approaches, but must, in most cases, be made by more novel approaches. Stable, concentrated, yet sufficiently fluid suspensions of submicron colloidal particles must be achieved in order to fabricate ceramic bodies of complex geometrical shapes and uniform microstructures. Colloidal consolidation techniques must be developed to ensure that unwanted homogeneities are not introduced into the microstructure at this step. All processing aids added during previous processing steps must be removed with minimal disruption to the green compact. Finally, densification should take place at relatively low temperatures, with controlled pore closure (i.e., achievement of nearly theoretical density), reduced grain growth, and, for composite materials, controlled introduction of intergranular material. This sequence of processing steps has a "memory," in the sense that all stages must be under the direct control of the process designer for success to be realized.

ACKNOWLEDGMENTS

LITERATURE CITED

1. Norton, F. H. 1974. *Elements of Ceramics*, 2nd ed., Reading, CA: Addison-Wesley.
2. Kocatopcu, S. S. 1946. *J. Am. Ceram. Soc.*, 29:4.
3. See, e.g., *Am. Ceram. Soc. Bull.*, 64:1082, 64:1097 (1985).
4. Kingery, W.D. 1978. *Ceramics Processing Before Firing*, G. Y. Onoda, Jr., L. L. Hench, eds., New York: Wiley.
5. Lange, F. F., Aksay, I. A., Davis, B. I. 1983. *J. Am. Ceram. Soc.*, 66:407.
6. Hench, L. L., Ulrich, D. R., eds. 1984. *Ultrastructure Processing of Ceramics, Glasses and Composites*. New York: Wiley.
7. Brinker, C. J., Clark, D. E., Ulrich, D. R., eds. 1984. *Better Ceramics Through Chemistry*. Mat. Res. Soc. Symp. Proc., 32. Amsterdam: North-Holland.
8. Brinker, C. J., Clark, D. E., Ulrich, D. R., eds. 1986. *Better Ceramics Through Chemistry II*. Mat. Res. Soc. Symp. Proc., 32. Amsterdam: North-Holland.
9. Hench, L. L. and Ulrich, D. R., eds. 1986. *Science of Ceramic Chemical Processing*. New York: Wiley.
10. Davis, R. F., Palmour III, H., and Porter, R. L., eds. 1984. *Emergent Process Methods for High-Technology Ceramics*. New York: Plenum.
11. Messing, G. L., Mazdiyasni, K. S., McCauley, J. W., Haber, R. A., eds. 1987. *Ceramic Powder Science*. Westerville, OH: American Ceramic Society, Inc.
12. Kuczynski, G. C., Miller, A. E., Sargent, G. A., eds. 1984. *Sintering and Heterogeneous Catalysis*. New York: Plenum.
13. Kato, A., Hojo, J., and Watari, T. 1984. *Emergent Process Methods for High-Technology Ceramics*. R. F. Davis, H. Palmour III, R. L. Porter, eds. p. 123. New York: Plenum.

14. Kato, A. 1987. *Ceramic Powder Science. Adv. Ceram.,* 21. G. L. Messing, K. S. Mazdiyasni, J. W. McCauley, R. A. Huber, eds., pp. 181-192. Westerville, OH: American Ceramic Society, Inc.

15. Johnson, D. W. 1987. *Ceramic Powder Science. Adv. Ceramic,* 21. G. L. Messing, K. S. Mazdiyasni, J. W. McCauley, R. A. Haber, eds., pp. 3-19. Westerville, OH: American Ceramic Society, Inc.

16. Johnson, D. W. 1985. *Am. Ceram. Soc. Bull.* 64:1597-1602.

17. Yoldas, B. E. 1977. *J. Mat. Sci.* 12:1203-1208.

18. Okamura, H., Bowen, H. K. 1986. *Ceram. Intl.* 12:161-171.

19. Mazdiyasni, K. S., Lynch, C. J., Smith, J. S. 1967. *J. Am. Ceram. Soc.* 50:532.

20 Mazdiyasni, K. S., Brown, L. M. 1972. *J. Am. Ceram. Soc.* 55:548.

21. Mazdiyasni, K. S. 1984. *Better Ceramics Through Chemistry.* Brinker, C. S., Clark, D. E., Ulrich, D. R., eds., pp. 175-187. *Mat. Res. Soc. Symp. Proc.,* 32 Amsterdam: North-Holland.

22. Dosch, R. G. 1984. *Better Ceramics Through Chemistry.* Brinker, C. J., Clark, D. E., Ulrich, D. R., eds., pp. 199-204. *Mat. Res. Soc. Symp. Proc.,* 32 Amsterdam: North-Holland.

23. See, e.g., Matijevic, E. 1976. *Progr. Colloid & Polymer Sci.* 61:24-35.

24. Johnson, D. W. 1987. *Adv. Ceram.* 21:3.

25. Matijevic, E. 1984. *Ultrastructure Processing of Ceramics, Glasses, and Composites,* pp. 334-352. L. L. Hench, D. R. Ulrich, ed., New York: Wiley.

26. Matijevic, E. 1987. Personal communication.

27. Pak, S. 1988. M.S. Thesis. University of Washington, Seattle, WA, USA.

28. Reynon, P., Bastius, H., Fiedler, M. 1983. *Ceramic Powders.* Amsterdam: Elsevier, p. 499-504.

29. Akinc, M., Richardson, K. 1986. *Mat. Res. Soc. Symp. Proc.* 73:99-109.

30. Akinc, M., Celikkaya, A. 1987. *Adv. Ceram.* 21:57-68.

31. Kandori, K., Kon-no, K., Kitahara, A. 1987. *J. Colloid Interface Sci.* 115:579-582.

32. Gobe, M., Kon-no, K., Kandori, K., Kitahara, A. 1983. *J. Colloid Interface Sci.* 93:293-295.

33. Inouye, K., Endo, R., Otsuka, Y., Miyashiro, K., Kaneko, K., Ishikawa, T. 1982. *J. Phys. Chem.* 86:1465-1469.

34. Liano, P., Thomas, J. K. 1986. *J. Colloid Interface Sci.* 117:505-512.

35. Kato, A. 1987. *Adv. Ceram.* 21:181-192.

36. Hollabaugh, C. M., Hull, D. E., Newkirk, L. R., Petrovic, J. J. 1984. *Ultrastructure Processing of Ceramics, Glasses and Composites,* pp.367-373. L. L. Hench and D. R. Ulrich, eds. New York: Wiley.

37. Biswas, D. R., Oh, P. S. 1986. *J. Am Ceram. Soc.,* 69, C90-C91.

38. Haggerty, J. S. 1987. *Adv. Ceram.* 21:353-366.

39. Haggerty, J. S. 1984. *Mater. Sci. Res.* 17:137-154.

40. Kagawa, M., Honda, F., Onodera, H., Nagae, T. 1983. *Mat. Res. Bull.* 18:1081-1087.

41. Matijevic, E. 1984. *Ultrastructure Processing of Ceramics, Glasses and Composites.* pp. 334-352. L. L. Hench and D. R. Ulrich, eds. New York: Wiley.

42. Aksay, I. A. and Kikuchi, R. 1986. *Science of Ceramic Chemical Processing,* L. L. Hench and D. R. Ulrich (eds.), John Wiley and Sons, New York.

43. Shih, W. Y., Aksay, I. A., and Kikuchi, R. 1987. *J. Chem. Phys.,* 86[9]:5127.

44. Efremov, I. F. *Surface and Colloid Science,* E. Matijevic, ed., John Wiley and Sons, New York, 1976, Vol. 8, pp. 85-192; and P. Picranski. 1988 *Contemp. Phys.,* 24, 25, provide extensive reviews on fluid-solid transitions in colloidal systems. Also, see K. E. Davis and W. B. Russel in this proceeding.

45. Shih, W. Y., Aksay, I. A., and Kikuchi, R. 1987. *Phys. Rev. A* 36[10]:5015.

46. Aksay, I. A., Shih, W Y., and Sarikaya, M. 1988. *Proceedings of the 3rd International Conference on Ultrastructure Processing of Ceramics, Glasses, and Composites*, John Wiley & Sons, NY.

47. Kim, S. I. and Aksay, I. A. 1988. To be submitted to *J. Am. Ceram. Soc.*

48. Norton, F. H. 1974. *Elements of Ceramics*, 2nd Ed., Addison-Wesley, Reading, CA.

49. Kocatopcu, S. S. 1946. *J. Am. Ceram. Soc.*, 29[4]:99.

50. Cesarano III, J., Aksay, I. A., and Bleier, A. 1988. *J. Am. Ceram. Soc.*, in press.

51. Cesarano III, J. and Aksay, I. A. 1988. *J. Am. Ceram. Soc.*, in press.

52. Darcovich, K. P. and Aksay, I. A. 1988. To be submitted to the *J. Am. Ceram. Soc.*.

53. Liu, J., Sarikaya, M., and Aksay, I. A., unpublished work.

54. Shaw, T. M. 1986. *Mat. Res. Soc. Symp. Proc.* 73:215-223.

55. LeNormand, R. 1987. *A. I. P. Conf. Proc.* 154:98-115.

56. Wilkinson, D. 1984. *Phys. Rev. A.* 30:520-531.

57. Wilkinson, D., Williamsen, J. F. 1983. *J. Phys. A.* 16:3365-3376.

58. Wilkinson, D. 1986. *Phys. Rev. A.* 34:1380-1391.

59. Scherer, G. W. 1986. *J. Non-Cryst. Solids.* 87:199-210.

60. Scherer, G. W. 1987. *J. Non-Cryst. Solids.* 89:217-238.

61. Scherer, G. W. 1987. *J. Non-Cryst. Solids.* 91:83-100.

62. Scherer, G. W. 1987. *J. Non-Cryst. Solids.* 91:101-121.

63. Scherer, G. W. 1987. *J. Non-Cryst. Solids.* 92:122-144.

64. Johnsson, A., Carlstrom, E., Hermansson, L., Carlsson, R. 1983. *Proc. Brit. Ceram. Soc.* 33:139-147.

65. Do, C. II. Sun, Y.-N., Sacks, M. D., Williams, J. W., Scheiffle, G. W. 1986. Presented at 88th Annual Meeting, American Ceramic Society, Chicago, II., USA, Paper 9-E-86.

66. Mutsuddy, B. C. 1987. A. I. Ch. E. Conf. on Emerging Technologies in Materials. Minneapolis, MN, USA. Paper CE5 '.

67. Cima, M. J. 1987. Presented at A. I. Ch. E. Conf. on Emerging Technologies in Materials. Minneapolis, MN, USA. Paper CE5.2.

68. Farneth, W. E. and Staley, R. II. 1987. Presented at A. I. Ch. E. Conf. on Emerging Technologies in Materials. Minneapolis, MN, USA. Paper CE5.4.

69. Quackenbush, C. L., French, K., and Neil, J. T. 1983. *Ceram. Eng. & Sci. Proc.* 3:20-34.

70. Walker, B. E., Jr., Rice, R. W., Becher, P. F., Bender, B. A., Coblenz, W. S. 1983. *Ceram. Bull.* 62:916-923.

71. Barringer, E., Jubb, N., Fegley, B., Pober, R. L., Bowen, II. K. 1984. *Ultrastructure Processing of Ceramics, Glasses, and Composites,* pp. 315-333. L. L. Hench, D. R. Ulrich, eds. New York: Wiley.

72. Fegley, B. Jr., White, P., Bowen, II. K. 1985. *Am. Ceram. Soc. Bull.* 64:1115.

73. Ogihara, T., Mizutani, N., Kato, M. 1987. *Ceram. Intl.* 13:35.

74. Lange, F. F., Kellett, B. 1986. In: *Science of Ceramic Chemical Processing,* pp. 561-574. L. L. Hench, D. R. Ulrich, eds. New York: Wiley.

75. Martin, C. B. 1987. M.S. Thesis. University of Washington, Seattle, WA, USA.

76. Fukuda, S. 1988. Ph.D. Thesis. University of Washington, Seattle, WA, USA.

77. Shinohara, N., Dabbs, D. M., and Aksay, I. A. 1986. *SPIE Infrared and Optical Transmitting Materials.* 683:19-24

APPENDIX X

PROCESSING WITH NANOMETER-SIZED COLLOIDS

Ilhan A. Aksay, Gregory C. Stangle, and Mehmet Sarikaya

Department of Materials Science and Engineering; and the Advanced Materials Technology Program, The Washington Technology Center
University of Washington, Seattle, Washington, USA 98195

ABSTRACT

The main advantages of colloidal techniques center around two needs: (i) the need to consolidate powders as homogeneously as possible with respect to chemical and density fluctuations, and (ii) the need to shape complex geometries with a minimum degree of volume change (i.e., near-net-shape forming). Nanometer-sized particles provide the best solution for the first need but generally fail in the second category due to low density packing of particles. The work summarized in this paper addresses this low density packing problem. We highlight two important procedures to achieve high density packings with nanometer-sized particles: (i) the minimization of the effective particle size while still retaining a sufficient degree of suspension stability, and (ii) restructuring of particle clusters in weakly attractive systems that no longer retain suspension stability (i.e., flocculated suspensions).

INTRODUCTION

The use of powders in the submicron range is preferred in the fabrication of advanced ceramics, due primarily to the effects of particle size on sintering behavior and microstructural evolution. However, a significant difficulty which arises in employing submicron particles is their tendency to agglomerate due to interparticle attractive forces, particularly van der Waals.[1] Subsequent densification may be impeded due to packing density variations associated with agglomerates.[2-3]

Colloidal suspension techniques provide advantages in control of microstructural uniformity by minimizing the detrimental effects of agglomerates.[4-5] A process leading to the formation of a colloidally consolidated compact begins with the dispersion of the particles in a liquid medium. This dispersion process possesses a number of attractive features: poorly packed agglomerates can be removed by gravitational or centrifugal sedimentation; additional modifications of the particles' surface chemistry can be ac-

complished by using surface-active polymers and, for aqueous systems, varying pH and ionic strengths; and particles in multiphase systems can be mixed on a length scale equal to the size of the individual particles.

Furthermore, colloidal techniques (particularly for powders in the submicron size range) are essential in producing highly concentrated yet sufficiently fluid colloidal suspensions that are suitable for near-net-shape forming while simultaneously avoiding problems with undesirable agglomerate formation: a goal with submicron particles would be > 70 vol.% solids content with a < 1 Pa·s suspension viscosity. These ceramic powder suspensions with high solids content but low viscosity are then consolidated into densely packed states. Achievement of higher powder packing densities results in attaining higher sintered densities at lower sintering temperatures and with lower shrinkages than could be achieved in the case of lower packing densities.

Recent research results have shown that when particle surfaces are coated with polymeric processing aids, highly concentrated (> 60 vol.%) yet sufficiently fluid (< 1 Pa·s) suspensions suitable for subsequent shape-forming (i.e., consolidation) processes can be prepared if the particles are larger than 1000 Å (0.1 μm).[6] In the nanometer range (< 0.1 μm), however, the same level of success has not been achieved yet.[7-8] It has been customary to expect that colloidal suspensions of nanometer-sized particles (i.e., particulate sols) cannot be concentrated to high solids loading levels. Typically, phase transitions from a low viscosity sol to a high viscosity gel state are expected at solids loadings < 30 vol.% (Figure 1). Contrary to this common view, in the following sections, we illustrate that nanometer-sized particles can also be consolidated to densities > 50 vol.% prior to the removal of the fluid phase from the system.

To achieve this goal, we highlight two important procedures: (i) the minimization of the effective particle size while still retaining a sufficient degree of suspension stability, and (ii) restructuring of particle clusters in weakly attractive systems that no longer retain suspension stability (i.e., flocculated).
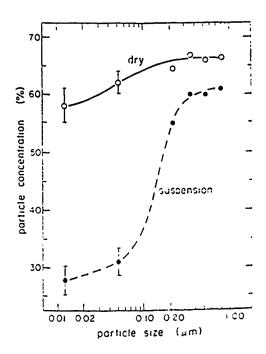

Figure 1. The effect of particle size on the maximum particle concentration of electrostatically stabilized suspensions of α-Al₂O₃ (~ 1 μm) and AlOOH (< 1 μm) without exceeding a suspension viscosity of 1 Pa·s (broken line). Corresponding densities after drying are shown with the solid line.

THE COLLOIDALLY CONSOLIDATED POWDER COMPACTS

Colloidal suspensions are quite simply a dispersion of a discrete solid phase in a continuous fluid phase. The suspensions may be dilute or concentrated (with respect to solids concentration), while the latter may be easily deformed or relatively rigid. The particles are known to interact with one another by one or a combination of attractive and repulsive interparticle forces. In general, colloidal suspensions can be dispersed by electrostatic, steric or electrosteric interparticle interaction mechanisms, either by generating an ionic cloud around the particles and/or by coating the particles with polymeric or macromolecular material. In the first case, electrostatic repulsion occurs when the ionic clouds overlap. In the second case, steric repulsion arises when the adsorbed polymer layers interact. Electrosteric repulsion occurs when both mechanisms are significant. Useful introductions to electrostatic and steric stabilization of colloidal suspensions are provided by Hunter[9] and Napper[10], respectively. The underlying feature of all these stabilization techniques is the ability to fine-tune the balance between repulsive interparticle interactions with respect to the (effectively fixed) attractive van der Waals interactions, in an effort to enhance suspension stability, and achieve a higher degree of packing density uniformity upon consolidation.

Colloidal consolidation in the usual sense is simply the nucleation and growth of particle clusters.[5,11-13] It is, then, the transition of a colloidal suspension from a dispersed to a clustered state. It may also be considered as a transition from a fluid-like to a solid-like state, by analogy with atomic systems. Our prior work showed that nonequilibrium structures resulting from the formation of these clusters become responsible for lower packing densities than are expected under equilibrium conditions.[12-15] It was argued that since the fundamental process of cluster formation is not easily avoidable, the detrimental effects of cluster formation should be minimized through a restructuring process towards higher packing densities.[12-15] As illustrated in the following sections, this restructuring process requires a careful manipulation of the interaction energy between particles. In the nanometer particle size range, this manipulation becomes exceedingly difficult for two reasons (Figure 2): (i) when particle interactions are repulsive, surface modifications needed to create these repulsive interactions result in a significant volume increase in the effective size of the particles, and (ii) when particles are attractive, the tendency to form fractal clusters increases. In either case, the packing densities become low. In the following sections, we address both of these problems through modification of particle surfaces.
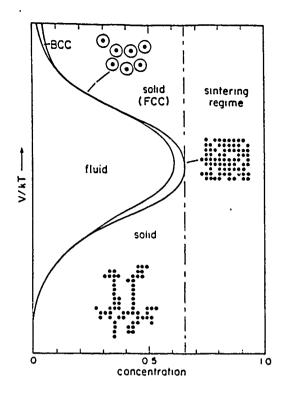
Figure 2. Schematic form of nonequilibrium colloidal phase diagram. V denotes the generalized interaction potential between particles; k is the Boltzmann constant; and T is the temperature.

NANOPARTICLE SYSTEMS WITH ELECTROSTATIC INTERACTIONS

Electrostatic stabilization can be easily understood in terms of the net attractive or repulsive interaction forces between colloidal particles in suspension.[9,13,14] Repulsive forces depend principally upon the interactions of the layers of adsorbed surface ions surrounding the particle. The thickness of the layer and hence the effective range of the interaction potential depends upon surface charge density and (for aqueous systems) ionic strength. The magnitude of repulsive electrostatic forces decreases exponentially with distance from the surface, having a range on the order of the Debye-Hückel length (i.e., approximately the thickness of the layer of adsorbed ions). Van der Waals attractive interaction forces arise because of London dispersion forces, Keesom forces due to interactions between permanent dipoles and induced dipoles in the particles, and Debye forces due to interactions among induced dipoles. For interacting spherical particles, these attractive forces decay as the inverse power of the separation distance between particle surfaces. Further, van der Waals attractive forces are nearly independent of the ionic strengths of the suspending medium. The combined form of the interaction potential between particles constitutes the DLVO theory, resulting in a pairwise potential that, in general, has a maximum (either in the repulsive or attractive range) separating two minima (both in the attractive range).[9]

To illustrate the importance of the electrostatic interaction mechanism in stable suspensions containing nanometer-sized particles, we briefly summarize our investigations of colloidal silica suspensions. Figure 3 shows packing densities as a function of pH for ~ 16 nm amorphous Ludox silica particles with 10^{-3} M NaNO$_3$ electrolyte.[16] Particles were consolidated under a centrifugal force field and packing densities were measured in the wet state before drying.[16] The inset shows mobility and zeta potential values as a function of pH determined by electrophoresis. These results, reported in Figure 3, are contrary to expectations because the lowest packing densities occur at the highest pH where the particles have the highest zeta potentials. This is opposite to the trends seen in larger submicron oxide particles.[5,13] Viscosity experiments indicate that the suspensions at high pH have the highest viscosities, corresponding to the low packing densities. As the pH is lowered from pH 9, the wet gel packing density increases and the suspension viscosity decreases. This corresponds to the compression of the effective particle radius with decreasing potential. Above pH 9, the presence of excess counterions due to base addition also compresses the effective particle radius, again resulting in an increase in packing density.
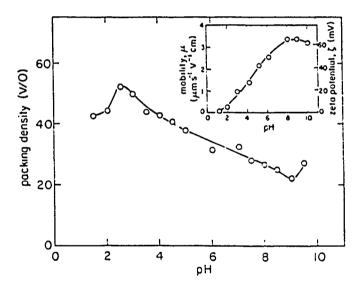
Figure 3. Pa.king densities and zeta potentials of ~16 nm size silica particles as a function of pH (10^{-3} M NaNO$_3$) before drying.[16]

Although the effective particle size effect due to long-range repulsive interactions has been seen in larger submicron silica particles at high charge, the effect is much more extreme in reducing packing densities in nanometer-sized particles. This occurs because the size of the double layer is significant relative to the particle size. Our results, therefore, indicate that highly charged, highly stable systems are not desirable for nanometer particle processing, in contrast to the conventional processing schemes

used for larger submicron particle systems. What is important, however, is the minimization of the screening length around the particles.

NANOPARTICLE SYSTEMS WITH STERIC INTERACTIONS

Clearly, manipulation of particle zeta-potential is not the only means by which to regulate interparticle interactions. In steric stabilization, this interaction potential adjustment is achieved by controlling the extent of polymer adsorption on the surface of the colloidal particle. Steric interaction forces result from interaction of the adsorbed polymer layers and can be either attractive or repulsive, depending in large part upon the solvent-polymer, polymer-polymer, and polymer-particle compatibility in the system considered. For example, if the solvent power for the adsorbed polymer is low, the polymer layers interpenetrate and suspension stability is poor. If the solvent power is "satisfactory," then little polymer-polymer interpenetration occurs and colloidal suspension stability is enhanced. Polymer adsorption can occur by electrostatic, hydrogen, or covalent bonding mechanisms.[10,17] The key requirement in steric stabilization, as in electrostatic stabilization, is that interparticle repulsive forces must be sufficiently high with respect to van der Waals attractive forces in order to prevent nucleation and growth of particle clusters and to prepare dispersed suspensions. The dispersed state is possible, of course, only below a certain critical particle concentration.[13,14]

A unique case of sterically interacting particles is one where particles are weakly attractive and thus clustering of particles cannot be avoided. But, the clusters can still pack densely due to a significant amount of restructuring. The importance of cluster restructuring through particle unbinding and rearrangement to obtain dense packings was first discussed by Shih et al.[12] It was predicted that in weakly attractive systems, although particle clustering cannot be prevented, high packing densities can still be achieved through restructuring. Liu et al.'s[18] experiments with surfactant-coated nanometer-sized gold particles have recently confirmed the validity of this prediction (Figures 4 and 5). The two contrasting views shown in Figures 4 and 5 illustrate that, when particles are coated with a surfactant (Adgon 462, a quaternary ammonium salt), dense packing of clusters is achieved (Fig. 4). On the contrary, when particle clustering is induced by the addition of NaCl or pyridine, particles stick very strongly and low density clusters result (Fig. 5). These results indicate that by controlling the particle interactions with the amount of adsorbed surfactant, clusters with high densities can be formed. It should be noted that this observation contrasts the results presented in the previous section where dense packing of silica particles was obtained from a stable suspension, whereas here similar results are obtained with an unstable suspension.
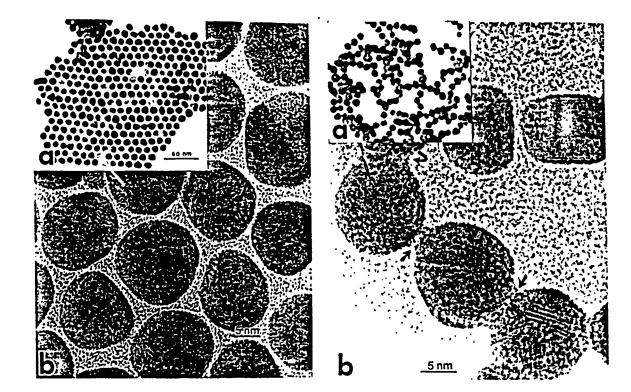
Figure 4. Close packing of ~15 nm size gold particles with a surfactant coating: (a) low magnification bright field; and (b) high resolution electron micrograph images.

Figure 5. Ramified clustering of gold particles without surfactant coating: (a) low magnification bright field; and (b) high resolution electron micrograph images revealing structural details at the particle/particle contact points.

CONCLUSIONS

This paper summarizes our recent results on the colloidal dispersion and consolidation of particles with diameters smaller than 0.1 μm. Concentrated yet sufficiently fluid suspensions of nanometer-sized particles must be achievable in order to fabricate ceramic bodies of complex geometrical shapes and uniform microstructures. Studies on suspensions in which electrostatic interactions are important demonstrated that dense nanoparticle compacts can be achieved when the effective particle size is minimized, so that particles are stable due to short-range repulsion. Other studies on suspensions in which steric interactions predominate indicate that aggregation of ultrafine particles can be controlled by the use of surfactants and that cluster densities depend on the degree of restructuring that occurs when direct particle contact is prevented by the presence of these surfactants.

ACKNOWLEDGMENTS

REFERENCES

1. See, e.g., Bacon, J. et al. 1983. *Faraday Discuss. Chem. Soc.*, 76:165.

2. Kingery, W.D. 1978. In *Ceramic Processing Before Firing*, G. Y. Onoda, Jr., and L. L. Hench, eds., New York: Wiley.

3. Lange, F. F., Aksay, I. A., and Davis, B. I. 1983. *J. Am. Ceram. Soc.*, 66:407.

4. Barringer, E. A., and Bowen, H. K., 1982. *J. Am. Ceram. Soc.*, 65:C199.

5. Aksay, I. A. 1984. In *Advances in Ceramics*, vol. 9, J. A. Mangels and G. L. Messing, eds., Am. Ceram. Soc., OH.

6. Cesarano III, J., and Aksay, I. A. 1988. *J. Am. Ceram. Soc.*, 71:1062.

7. Rabinovitch, E. M., Johnson, D. W., MacChesney, J. B., and Vogel, E. M. 1983. *J. Am. Ceram. Soc.*, 66:683.

8. Brinker, C. J., Drotning, W. D., and Scherer, G. W. 1984. In *Better Ceramics Through Chemistry*, MRS Proc., 32:25.

9. Hunter, R. S. 1981. *Zeta Potential in Colloid Science: Principles and Applications*, London: Academic Press.

10. Napper, D. H. 1983. *Polymer Stabilization of Colloidal Dispersions*, London: Academic Press.

11. Onoda, G. Y., Jr. 1985. *Phys. Rev. Lett.*, 55:226.

12. Shih, W. Y., Aksay, I. A., and Kikuchi, R. 1987. *Phys. Rev. A*, 36:5015.

13. Aksay, I. A. and Kikuchi, R. 1986. In *Science of Ceramic Chemical Processing*, L. L. Hench and D. R. Ulrich, eds., New York: Wiley.

14. Shih, W. Y., Aksay, I. A., and Kikuchi, R. 1987. *J. Chem. Phys.*, 86:5127.

15. Aksay, I. A., Shih, W. Y., and Sarikaya, M. 1988. In *Ultrastructure Processing of Advanced Ceramics*, J. D. Mackenzie and D. R. Ulrich, eds., New York: Wiley.

16. Tarasevich, B. J., Liu, J., Sarikaya, M., and Aksay, I. A. 1988. In *Better Ceramics Through Chemistry III*, MRS Proc., 121:225.

17. Cesarano III, J., Aksay, I. A., and Bleier, A. 1988. *J. Am. Ceram. Soc.*, 71:250.

18. Liu, J., Sarikaya, M., Shih, W. Y., and Aksay, I. A., unpublished work.

APPENDIX XI

LIQUID CRYSTAL-LIKE PHASE SEPARATION IN SYSTEMS OF MACROSCOPIC RODS

LARRY A. CHICK[*], CHRISTOPHER VINEY[**] AND ILHAN A. AKSAY[**]

[*]Battelle Pacific Northwest Laboratory, P.O. Box 999, Richland, WA 99352

[**]Department of Materials Science and Engineering FB-10, and the Advanced Materials Technology Program, University of Washington, Seattle, WA 98195

ABSTRACT

Experiments with monolayers of macroscopic rods indicate separation into isotropic and aligned phases at greater-than-critical concentrations. This behavior is qualitatively similar to that of rodlike liquid crystalline polymers, which in turn has been modelled successfully in three dimensions by Flory and Ronca. We have adapted their approach to predict the ordering of rods in two dimensions. A preliminary phase diagram is presented. The critical rod concentration at which an aligned phase can appear first is a decreasing function of rod axial ratio. Rods of a given axial ratio will phase separate at lower overall concentrations in two dimensions than in three.

INTRODUCTION

Macroscopic rods, in the form of fibers or whiskers, are used as reinforcing agents in a wide variety of composite materials. Strength, stiffness and toughness all are increasing functions of the attainable volume fraction of rods [1-3]. There are several available and potential processing methods for inducing global rod alignment, thus allowing them to pack more densely. However, the properties of the finished artefact are then necessarily anisotropic. For situations where isotropic properties are desirable, it is of fundamental interest to determine whether clusters of aligned rods can develop spontaneously. While such alignment would allow accommodation of a greater rod volume fraction than is possible if the rods are independently and randomly oriented, it is not clear whether the presence of the clusters would improve the mechanical properties. If the matrix material is brittle, the clusters may act as crack-initiating defects. In either case, it is of value to understand and predict the formation of such clusters.

Evans and Gibson [4] suggest that the maximum packing density for randomly oriented macroscopic rods is comparable to the phase boundary marking the appearance of the nematic phase in a system of rod-like liquid crystalline polymer molecules. They contend that macroscopic rods have no analog to diffusion as a means of effecting their rearrangement into an aligned state. Chick and Aksay [5] suggest that the vibrations and turbulence that prevail during the processing of many composites may facilitate such rearrangement. If phase separation does occur, we should expect an athermal model to apply, since the interactions between rods will be dominated by steric repulsion. A notably successful model for phase separation in athermal systems of rodlike particles has been derived by Flory and Ronca [6]. It is found to be qualitatively applicable to a number of polymer - solvent systems [7]. We have set out to investigate the applicability of this model to the systems of macroscopic and truly athermal rods that pertain to composite materials in the absence of forced alignment. Our analysis is confined to two dimensions (a monolayer of rods), for the following reasons: Firstly, it is simpler to observe clustering in two dimensions than in three, both for models that are generated statistically in a computer and also for real systems. (In real three-dimensional systems, the container walls constrain those configurations that are readily visible; it is difficult to characterize the bulk configurations.) Secondly, practical composites frequently are built up from laminated sheets that individually contain a two-dimensional distribution of fibers or whiskers.

THE MODEL IN TWO DIMENSIONS

Our approach is directed by the model of Flory and Ronca [6], which is derived for three dimensions. We shall use the notation (FRxx) to refer to equation (xx) in their work. If the Flory-Ronca model were exact, adapting it to two dimensions would only require modification to parameters that characterize rod orientations. The model contains three such parameters. One is a disorientation index y, defined for each molecule in terms of the lattice model that constitutes the basis of the Flory-Ronca approach. y is the number of adjacent lattice rows occupied by a molecule, where rows are defined as lying parallel to the direction of preferred molecular orientation X. Other parameters that describe molecular orientation are ψ, the angle between a rod and X, and ω_y, the fractional range of *solid* angle associated with molecules having a given value of y. In the two-dimensional case of present interest, we have to redefine ω_y as a fractional range of *planar* angle. Thus

$$y = (4/\pi)x \sin \psi \qquad\qquad \text{(FR27)}$$

and

$$\omega_y = \sin \psi \,(d\psi / dy) \qquad\qquad \text{(FR28)}$$
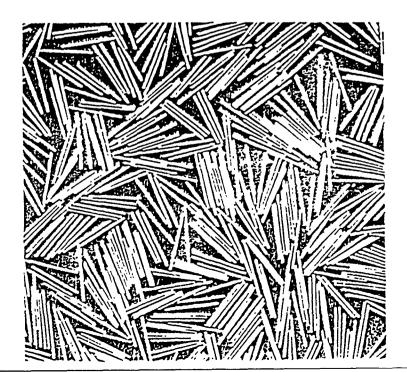
are replaced in two dimensions by

$$y = 1 + (x - 1)\sin \psi \qquad\qquad (1)$$

and

$$\omega_y = d\psi / dy = (\sec \psi)/(x - 1) \qquad\qquad (2)$$

Here x is the axial ratio of the rods, which are assumed to be monodisperse. However, if we effect these simple substitutions only, we find that the model does not predict any phase separation, and so does not agree with experiment (Fig.1). Some further refinements are therefore necessary.

Figure 1

Wooden rods (2mm diameter) with an axial ratio of 25. Rods were scattered onto a horizontal substrate, forming a random pile several rods deep. The substrate was then vibrated until the rods formed a monolayer. Since all the rods can be accommodated in two dimensions, their distribution after prolonged vibration should be independent of the density and surface finish of individual rods.

The Flory-Ronca implementation of the lattice model starts out by contemplating the number of situations v_j available to the jth rod, if it is to be incorporated into an existing configuration of $(j - 1)$ rods. An explicit formula for v_j is given as Eq.(FR1). The derivation is equally applicable to either two or three dimensions. However, Flory and Ronca express clear reservations about the validity of the equation at large disorientations of the rods. Also [8], the equation permits the model to contain intersecting rods as shown in Fig.2.
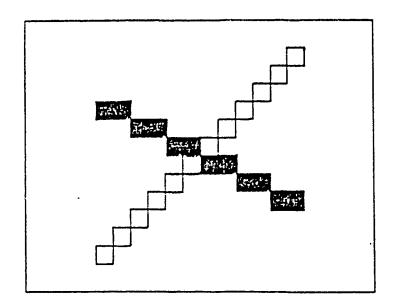
Figure 2

Flory and Ronca's lattice model allows the situation shown alongside, where rods can intersect provided that their segments do not overlap.

While the approximations inherent to Eq.(FR1) do not seem to present a problem in three dimensions, they apparently become significant when the overall number of rod configurations is limited by working in two dimensions. We therefore choose to rely on Monte Carlo techniques to obtain values of v_j. We postulate that v_j is given consistently by:

$$\frac{v_j}{n_0} \propto \frac{1}{<T_j>} \qquad (3)$$

where n_0 is the total number of lattice cells in the two-dimensional model. The quantity $<T_j>$ is the average number of tries required for the Monte Carlo algorithm to place the jth rod in an existing configuration of $(j - 1)$ rods. The algorithm first chooses an angle for the jth rod, and then tries combinations of positional coordinates until the rod is placed successfully. $<T_j>$ necessarily increases with increasing rod concentration, since, at each concentration, it is inversely proportional to the fraction of situations available in the existing configuration as stated in Eq.(3). For the isotropic phase, the program calls upon a random number generator to choose the orientation of each rod. For the aligned phase, the program uses two random numbers to generate orientations that follow a normal distribution with a user-defined standard deviation [9]. An appropriate initial standard deviation of $10°$ was estimated by using the Flory-Ronca model to calculate the average $<\psi>$ from Eq.(FR27). Flory and Ronca claim that $<\psi>$ is insensitive to x; using their model, we found that $<\psi>$ changes by less than 20% as x varies between 10 and 100. Although the values of $<\psi>$ thus calculated are pertinent to three dimensions, we feel that they represent a useful initial estimate for the value in two dimensions.

Three separate Monte Carlo runs were averaged to estimate $< T_j >$ at each value of j. For both the isotropic and anisotropic phases, we found that the empirical relationship between $\ln < T_j >$ and j can be fitted closely by a quadratic equation:

$$\ln < T_j > = Aj^2 + Bj + C \tag{4}$$

The constant C is necessarily equal to zero. We substitute Eq.(4) into Eq.(3) to obtain values of v_j.

Our approach then parallels that of Flory and Ronca in calculating total configurational entropy Z_M as the product of combinatory (steric) and orientational factors. Since we are dealing with an athermal system, there is no enthalpic contribution to the free energy. We can therefore determine phase separation at a given value of x by plotting $- \ln Z_M$ as a function of the area fraction of rods (xj / n_o) for both the isotropic and the anisotropic phase, and then searching for a common tangent to both curves. Our expressions for Z_M in both phases are derived analogously to Eq.(FR7).

RESULTS AND DISCUSSION

Our preliminary predictions for phase separation in two dimensions are shown in Fig.3. For the purposes of comparison, the results for phase separation in three dimensions as predicted by Flory and Ronca are also given. It is evident that separation occurs at lower rod packing fractions in two dimensions. Qualitatively, this would be predictable on the basis of the restricted number of orientations available in two dimensions. We are at present investigating the extent to which our diagram for two dimensions is sensitive to the assigned standard deviation of orientations in the anisotropic phase.
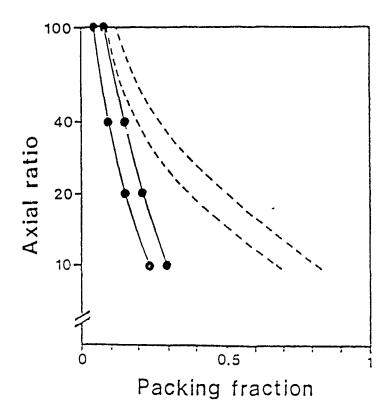

Figure 3

Preliminary (partial) phase diagram for rods in two dimensions (solid lines). Phase boundaries have been calculated for aligned rods that follow a normal distribution having a standard deviation of $10°$. Flory and Ronca's phase diagram for three-dimensional systems is also shown (broken lines).

approximation leads to a prediction that agrees at least qualitatively with experiment, we can deduce that the Flory-Ronca approximation tends to underestimate v_j at high axial ratios, and that it overestimates v_j at low axial ratios.
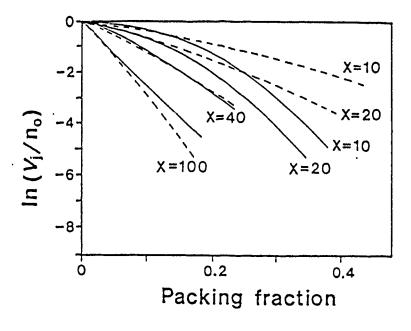

Figure 4

Comparison of $\ln(v_j/n_o)$ *versus* rod concentration for our model and the Flory-Ronca model.
Solid lines were calculated from Eq.(3) and Monte Carlo data. Broken lines were calculated from Eqs.(FR1) and (1), with $\bar{p} = 1 + (x-1)\sin < \psi >$. Here $<\psi>$ is set equal to $8°$, consistent with the standard deviation of $10°$ chosen for our normally distributed rod orientations.

The athermal separation of rods into isotropic and anisotropic phases can also be demonstrated by our Monte Carlo program for randomly oriented rods, with the area fraction of rods increased beyond the critical value defined by the common tangent construction. Fig.5 shows clusters of aligned rods, with random alignment persisting in the intervening spaces. However, once a rod is placed successfully by the Monte Carlo program, subsequent motion is disallowed. For this reason, the configuration in Fig.5 cannot be associated with the minimum free energy for the given rod aspect ratio and packing fraction.
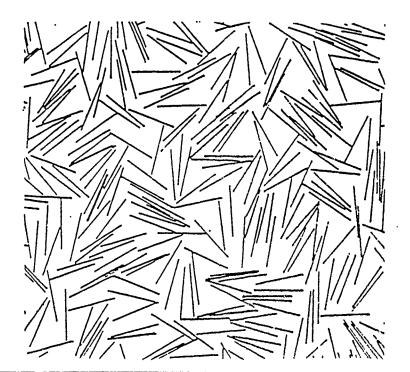

Figure 5

Configuration produced by Monte Carlo program for rods with an aspect ratio of 40. The area fraction shown, 0.12, is in the middle of the two-phase region on the proposed phase diagram (Fig.3).

Simulated annealing should lead to growth and coalescence of ordered clusters. By developing selection rules to identify whether any one rod belongs to a particular cluster or not, we anticipate being able to predict the *scale of the microstructure, i.e.* the average ordered domain size, as a function of the length of anneal. This will add to our ability to predict and therefore control the properties of fiber- or whisker-reinforced composite materials.

CONCLUSIONS

1. With some modifications, Flory and Ronca's model for the athermal phase separation of rodlike particles in three dimensions can be adapted for two-dimensional systems.
2. In two dimensions, as in three, the critical rod concentration at which an aligned phase can appear first is a decreasing function of rod axial ratio.
3. Rods of a given aspect ratio will phase separate at lower overall concentrations in two dimensions than in three.
4. Microstructures of the phase-separated and single phase anisotropic systems can be calculated by Monte Carlo techniques. This offers the possibility of predicting microstructural scale in such systems.

ACKNOWLEDGEMENTS

REFERENCES

1. G.C. Wei and P.F. Becher, American Ceramic Society Bulletin 64(2), 298 (1985).
2. R.W. Davidge, Composites 18(2), 92 (1987).
3. A.G. Evans, M. Ruchle, B.J. Dalgleish and M.D. Thouless in Advances in Structural Ceramics, edited by P.F. Becher, M.V. Swain and S. Sōmiya (Mater. Res. Soc. Proc. 78, Pittburgh, PA 1987) pp.259-271.
4. K.E. Evans and A.G. Gibson, Composites Science and Technology 25, 149 (1986).
5. L.A. Chick and I.A. Aksay in Atomic and Molecular Processing of Electronic and Ceramic Materials: Preparation, Characterization and Properties, edited by I.A. Aksay, G.L. McVay, T.G. Stoebe and J.F. Wager (Mater. Res. Soc., Pittburgh, PA 1987) pp.135-145.
6. P.J. Flory and G. Ronca, Molecular Crystals and Liquid Crystals 54, 289 (1979).
7. P.J. Flory, Advances in Polymer Science 59 1 (1984).
8. A.M. Liebetrau, Battelle PNL (private communication).
9. G.E.P. Box and M.E. Mueller, Annals of Mathematical Statistics 29, 610 (1958).

APPENDIX XII

PHASE SEPARATION AND CLUSTERING IN SYSTEMS OF RODLIKE PARTICLES

LARRY A. CHICK*, CHRISTOPHER VINEY** AND ILHAN A. AKSAY**

*Battelle Pacific Northwest Laboratories, P.O. Box 999, Richland, WA 99352
**Department of Materials Science and Engineering FB-10, and the Advanced Materials
Technology Program, University of Washington, Seattle, WA 98195

ABSTRACT

Macroscopic rodlike particles are known to align, forming clusters at greater-than-critical concentrations. This behavior can be modeled as a phase-separation phenomenon, by analogy with liquid crystalline solutions. Flory and Ronca successfully modeled the phase separation of rigid rodlike molecules in three dimensions. We have adapted their approach to predict the formation of ordered domains in monolayers of rodlike particles. Monte Carlo simulations with continuous distributions of rod angles and positions were used to generate a phase diagram for rods in two dimensions. The implications for processing fiber- or whisker-reinforced composites are discussed.

INTRODUCTION

Although a few investigators[1-2] have reported maximum packing concentrations for randomly oriented, rodlike reinforcing media, we have found no published studies dealing with the local arrangement of such rods. Milewski's[1] empirical studies of randomly oriented macroscopic rods (wooden sticks) established an inverse relationship between the axial ratio and the maximum packing fraction. Evans and Gibson[2] used free-volume concepts to model the maximum packing fraction. These free-volume arguments were originally developed to model the liquid crystalline phase behavior of rodlike molecules. However, it is reasonable to expect the packing of macroscopic rods (sticks), microscopic rods (fibers and whiskers) and molecular rods to

follow the same pattern. Fig.1 compares Milewski's results with the upper concentration limit of stability for pure random phase predicted by Flory[3-4] for an athermal system of rodlike molecules. At concentrations greater than those indicated by the phase boundary, rodlike molecules phase-separate into an aligned (ordered; anisotropic) phase and a randomly oriented (disordered; isotropic) phase. This transition is spontaneous if the molecules undergo sufficient thermal agitation. Evans and Gibson assume that randomly oriented macroscopic and microscopic rods would not exhibit the transition to an aligned phase because they are too large to be agitated sufficiently. Yet, it is easily demonstrated that, when packed to high concentration, macroscopic rods do form into clusters with a high degree of internal alignment (Fig.2). We suggest that many processing operations that are used in fabricating composites, for example high-shear blending and sonication, provide sufficient agitation to allow at least partial transition to an aligned state.

In investigating similarities between the packing of macroscopic rods and the phase behavior of rigid rodlike molecules, we began with two-dimensional systems. It is simpler to observe the arrangement of rods in a monolayer than in the bulk of a three-dimensional system. Also, practical composites are frequently built up by laminating sheets that individually contain two-dimensional distributions of fibers. Our first task has been to establish a phase diagram for two-dimensional systems of rods. Several investigators[5-7] have studied two-dimensional configurations of rods by using lattice-based Monte Carlo simulations. However, these calculations restricted the rods to two distinct orthogonal orientations and to distinct positions determined by the lattice; none produced a phase diagram. We also employed Monte Carlo techniques, but utilized continuously varying position and orientation.

THE MODEL

Our approach is directed by the well-accepted three-dimensional model of Flory and Ronca[4], which is derived for athermal systems; *i.e.* for rods that exhibit neither attraction nor repulsion with respect to the solvent or each other. In such systems, the free energy is determined solely by entropy, which is composed of a translational and an orientational component. Flory and Ronca approximated the translational entropy on the basis of a lattice model, and the orientational entropy by using an equation derived from combinatorial analysis. It is possible to formulate their model in two dimensions by re-defining the parameters that describe rod

orientation. However, the model adapted in this way does not predict any phase separation[8]. Some further refinements are therefore necessary. We chose to measure the translational entropy directly from our Monte Carlo simulations, and to calculate the orientational entropy by using the exact combinatorial equation from which Flory and Ronca's approximation was derived.

The Flory-Ronca approach stipulates that the translational (combinatory) partition function is given by:

$$Z_c = \frac{1}{n_x!} \prod_{j=1}^{n_x} v_j \qquad (1)$$

where n_x is the total number of rods (with axial ratio x) in the lattice, and v_j is the number of vacant positions available to the jth rod when $j-1$ rods have already been placed in the lattice. This relation should apply equally well to two- or three-dimensional systems, as long as the v_j factors reflect placement in the system of appropriate dimension. We claim that v_j can be measured from our Monte Carlo data by using:

$$v_j = \frac{K}{<T_j>} \qquad (2)$$

where $<T_j>$ is the average number of tries required for the Monte Carlo algorithm to find a vacant position, within the existing configuration, in which to place the jth rod. K is a mathematically arbitrary constant of proportionality; it does not affect the outcome of subsequent calculations. The algorithm first randomly chooses an orientation for the jth rod, and then tries sets of randomly-generated positional coordinates until the appropriate space is found. As more rods are added to the configuration, $<T_j>$ increases, reflecting the increasing difficulty of happening upon an appropriate vacant site by choosing candidate positions at random. For the isotropic (randomly oriented) phase, rod orientations are evenly distributed between 0° and 180°. For the aligned phase, the orientations are generated to fill a normal distribution with a preset standard deviation. (Flory and Ronca assumed that the shape of the distribution of rod orientations within the aligned phase would have little effect on the results. They based their calculations on an even distribution. However, we have found that a normal distribution has significantly lower free energy than an even distribution with the same average angular deviation.) Data for the number of tries per rod are collected from several Monte Carlo runs

simulating a given system. The number of tries for the ith rod is averaged over the several runs, and the averaged data are fitted to an empirical relation of the form:

$$\ln <T> = AF_x^2 + BF_x \qquad (3)$$

where F_x is the area fraction (concentration) of rods and A and B are fitted coefficients. This relation is used with equations (2) and (1) to yield $\ln Z_c$. We have found that averaging the number-of-tries data from nine Monte Carlo runs is sufficient to determine the phase boundaries to within a few percent.

We calculate the orientational partition function by randomly generating large sets of angles with the appropriate distribution. The distribution is divided into a sufficiently large number of increments, and the partition function is calculated as:

$$Z_o = \frac{n_x!}{n_1!\,(n_x - n_1)!} \times \frac{n_x!}{n_2!\,(n_x - n_2)!} \times \dots \times \frac{n_x!}{n_p!\,(n_x - n_p)!} \qquad (4)$$

where n_1, n_2, ... , n_p are the numbers of rods falling within the respective increments. Each factor represents the number of ways of choosing the n_i rods within the ith increment from amongst the n_x rods in the entire system. As the number of increments is increased, the calculation converges at approximately 90 increments. For each phase, be it randomly, evenly, or normally distributed, the orientational entropy decreases linearly with increasing rod concentration.

The total entropy of the configuration, Z_m, is given by:

$$-\ln Z_m = -\ln Z_c - \ln Z_o \qquad (5)$$

Phase equilibria are determined by finding the common tangent to the free energy curves for the random and aligned phases.

RESULTS AND DISCUSSION

Our preliminary phase diagram for two-dimensional systems of rods, with axial ratios from 10 to 100, is shown in Fig.3. For comparison, Fig.3 also shows Flory and Ronca's[4] phase diagram for three-dimensional systems. In each case, the lines represent the boundaries of the two-phase region. It is evident that separation occurs at lower rod concentrations in two dimensions - which seems reasonable on the basis that orientational freedom is more restricted in two dimensions than in three.

Since the free energy of the aligned phase varies with the spread in rod orientations, it is necessary to determine which standard deviation gives the lowest free energy when compared to the random phase. The aligned phase having this particular standard deviation will achieve equilibrium with the random phase at the lowest possible overall concentration. At an axial ratio of 25, the first normally distributed aligned phase to appear as the concentration is increased has a standard deviation of approx. 12.5°. Investigation of the equilibria *between aligned phases* with various standard deviations indicates that, as the concentration is increased above the upper boundary of the two-phase region, aligned phases with progressively decreasing standard deviation have the lowest free energies. In other words, as the rod concentration is increased above the point at which the random phase disappears, the aligned phase gradually becomes more perfectly aligned.

Figures 4a and 4b are computer-generated drawings of the random and normally-distributed aligned phases that are in equilibrium for an axial ratio of 25. As the concentration is increased above that of the random phase shown, the translational freedom of the rods becomes so restricted that the total entropy can be decreased if clusters of aligned rods are formed. Thus maximum orientational entropy is sacrificed for increased translational entropy as the aligned phase appears and increases in area fraction. At the upper boundary of the two-phase region, given sufficient agitation, the entire configuration will transform to the aligned phase. This aligned phase will contain many "packing defects", but will attain more perfect alignment as the concentration is increased further.

The phase diagram (Fig.3) predicts area fractions of the phases present at equilibrium. It does *not* predict the *scale* of the microstructure. For example, above the two-phase region we know that the entire configuration will tend to transform to an aligned state with a predictable standard deviation of rod orientations, but the phase diagram does not predict the resulting cluster (domain) size.

IMPLICATIONS FOR COMPOSITE ENGINEERING

The discussion so far has assumed that the rods are sufficiently agitated, either by thermal or mechanical means, so that they can attain a configuration characterized by maximum total entropy. The degree to which they approach that equilibrium state is a matter of kinetics, and is therefore difficult to predict, especially for larger scale rods that have no thermally activated motion. Furthermore, in ceramic and metal composite processing, the motion of the fibers or whiskers is restricted by the presence of the matrix phase. However, the phase diagram does predict the critical concentrations above which the rods in a system will tend to form an aligned phase.

Also, our analysis establishes the minimum incidence of clustering present at a given concentration of rods. By way of illustration, consider the configuration in Fig.5a, produced by running the Monte Carlo algorithm for the random distribution well beyond the upper boundary of the two-phase region. This disordered configuration necessarily is unstable and is expected to transform to an aligned phase, given sufficient agitation. However, the Monte Carlo algorithm allows no movement of a rod once it is placed successfully. Since no movement has taken place and the configuration has a random distribution of rod orientations, the free energy of the configuration is given by the extrapolation of the random phase free energy curve. This configuration therefore represents the condition of minimum possible entropy at this concentration. Yet, there are definitely clusters of rods present. The clusters that appear at high concentrations in the random phase arise due to space-filling constraints. Simply put, the majority of the available vacant positions for new rods are next to, and aligned with respect to, existing rods. The most probable way to squeeze in more rods, is to add to the clusters. It is reasonable to expect that the microstructure in Figure 5a would coarsen if the configuration were annealed.

Fig.5b shows wooden rods with an aspect ratio of 25, at the same concentration as the computer-generated configuration of Fig.5a. The wooden rods were scattered at random onto a substrate and gently vibrated until all lay flat on the surface. The rods that were originally stacked on top of others tended to "push" their way onto the surface, thereby displacing rods that were already laying flat. Therefore, some limited rod movement was allowed during the development of this configuration. It is evident that rods in some of the resulting clusters tend to be more perfectly aligned, with somewhat larger vacant spaces between clusters, than in Fig.5a. Due to the limited motion allowed, the wooden rods have begun the transition to a minimum free energy (coarsened and more perfect) aligned phase.

In summary, the developers of composite materials should be aware that fibers or whiskers will inevitably form clusters even when no inter-rod attractive forces are present. Average cluster size will increase as the concentration of rods is increased. Above the critical concentration at which random alignment disappears, predicted by the phase diagram for the aspect ratio in question, the microstructure will tend to coarsen and the degree of alignment within clusters will increase. The degree of transformation attained will be governed by the extent of mechanical agitation used and by the properties of the matrix phase. Previously reported "maximum packing fractions" represent process-dependent kinetic barriers which will be surpassed for processes utilizing a high degree of mechanical agitation. These findings should apply to three-dimensional configurations as well, although the phase boundaries will occur at higher rod fractions. Mechanical models for fiber- and whisker-reinforced composites currently assume a simpler scenario in which the rods are independently as well as randomly oriented; the effect of clustering at high concentration has not been taken into account.

ACKNOWLEDGMENTS

REFERENCES

1. J.V. Milewski, *Advanced Ceramic Materials* 1(1), 36 (1986).
2. K.E. Evans and A.G. Gibson, *Composites Science and Tech.* 25, 149 (1986).
3. P.J. Flory, *Proc. Royal Soc.* A234, 73 (1956).
4. P.J. Flory and G. Ronca, *Molec. Cryst. and Liquid Cryst.* 54, 289 (1979).
5. H. Okamoto, *J. Chem. Phys.* 64(6), 2686 (1976).
6. F.L. McCrackin, *J. Chem. Phys.* 69(12), 5419 (1978).
7. A. Baumgartner, *J. Chem. Phys.* 84(3), 1905 (1985).
8. L.A. Chick, C. Viney, and I.A. Aksay, in *Rigid Rod Polymers*, edited by W.W. Adams, R.K. Eby and D.E. McLemore (Mater. Res. Soc., Pittsburgh, PA) in press.

FIGURE CAPTIONS

Figure 1
Comparison of Milewski's data for wooden rods and glass fibers[1] with the boundary of the pure random phase from Flory and Ronca's model for rigid-rod liquid crystals[4].

Figure 2
Clustering caused by mechanical vibration of wooden rods (axial ratio of 16) in a beaker.

Figure 3
Phase diagrams for rodlike particles. Solid lines enclose two-phase region for rods in two dimensions, from our analysis. Broken lines enclose two-phase region for rods in three dimensions, from the model of Flory and Ronca[4].

Figure 4
Computer-generated rod configurations for an axial ratio of 25:
a) Randomly oriented phase at maximum (equilibrium) rod concentration (area fraction of 0.158).
b) Normally distributed aligned phase in equilibrium with the random phase (area fraction of 0.192; standard deviation of 12.5°).

Figure 5
Metastable rod configurations at high concentration (area fraction of 0.263; axial ratio of 25).
a) Randomly oriented, computer-generated configuration obtained by running Monte Carlo for an extended period.
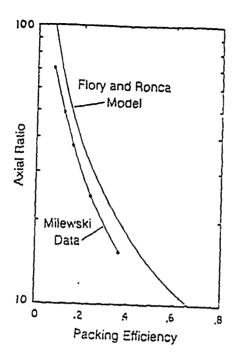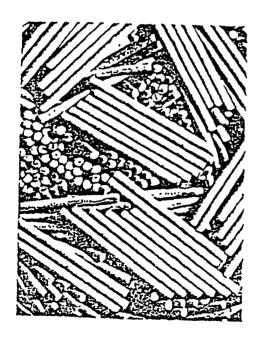b) Photograph of wooden rods vibrated until all lay flat on a horizontal substrate.
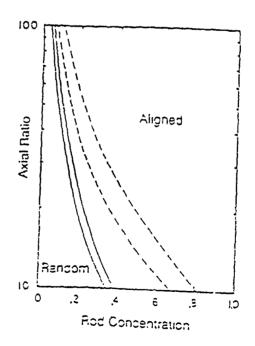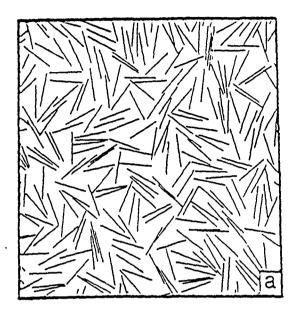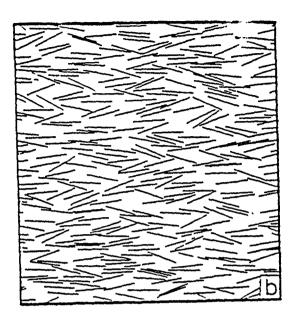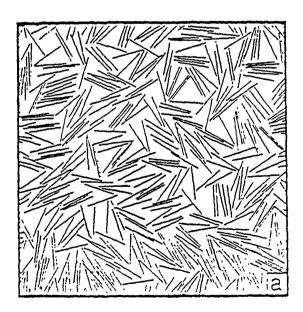
Figure 1.

Figure 2.

Figure 3.

Figure 4.

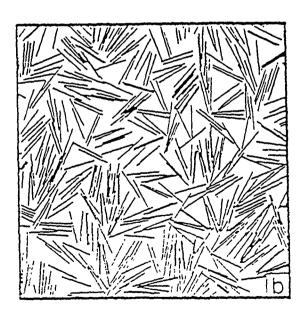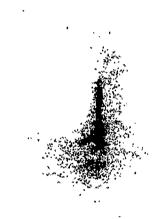
Figure 5.

APPENDIX XIII

ABSTRACTS OF PAPERS IN PREPARATION

1. Laoui, T., M. Sarikaya, D. L. Milius, and I. A. Aksay, "Phase Identification in B-C-Al Ternary System," *J. Am. Ceram. Soc.* (to be submitted, 1989).

Transmission electron microscopy imaging, diffraction, and spectroscopy techniques were used to identify the morphology, crystallography and composition of a new phase which forms in the Al-B-C ternary. The new phase, the so called XI phase, is a major second phase which forms during the processing of B_4C-Al metal-ceramic composite under controlled conditions. It spatially depletes the Al phase and replaces it around the B_4C particulates. The XI phase has a hcp crystal structure with lattice parameters; $a_o = 3.520$ A, and $c_o = 5.820$ A ($c/a = 1.61$), as determined by X-ray diffraction and convergent beam electron diffraction. Its composition may be given by the formula Al_4BC, as determined by electron energy loss spectroscopy.

2. Kim, G. H., M. Sarikaya, D. L. Milius, and I. A. Aksay, "Microstructural and Fractographic Characterization of B_4C-Al Alloy Cermets," *J. Am. Ceram. Soc.* (to be submitted, 1989).

Microstructural and fractographic characterization were performed on B_4C-Al 7075 alloy cermets. The composites were prepared by an infiltration technique where metal constituted up to 50% by volume. The distribution of the primary phases and the reaction products as well as their associated defects were analyzed to determine their effects on the fracture and strength properties. By profiling the crack paths on the matching fracture surfaces, the presence of the residual stress was recorded. The response of the microstructure to

the fracture of B_4C-Al 7075 alloy cermets which were subjected to high strain rate was studied by fracture surface replication and by thin foil TEM techniques.

3. Pyzik, A. J. and I. A. Aksay, "Relations Between Microstructure and Some Mechanical Properties in the B_4C-Al Composites," in *Ultrastructure Processing of Ceramics,* D. Uhlman, D. R. Ulrich, (eds.), John Wiley, (in preparation, 1990).

The dependence between the microstructure, the fracture toughness and the fracture strength of B_4C-Al has been characterized. It was found that mechanical properties of this system depend on the amount of metal present, the type and distribution of the secondary phases which form and a continuity factor. Materials have been obtained with a combination of 645 MPa strength and 9.7 MPa-m$^{1/2}$ toughness and 545 MPa strength and 14.4 MPa-m$^{1/2}$ toughness.

4. Pyzik, A. J. and I. A. Aksay, "Microdesigning of B_4C/AL Cermets," in (in preparation, 1989).

The B_4C/Al cermet combines a ceramic's high hardness, stiffness, and low density with a metal's ability to dissipate tensile stress. Early attempts to fabricate fully dense boron carbide/aluminum composites were mostly unsuccessful for two key reasons: (i) chemical reactions during processing proceed .aster than densification, thereby resulting in porous materials, and (ii) B_4C is not readily wet by Al unless process conditions are accurately controlled. In this paper, application of the infiltration technque leading to fully dense B_4C/Al cermets with tailorable microstructures is discussed. Control of the mixing, densification and post-heat treatment processes results in multi-ceramic composites with a reacted metal or in composites with the metal retained in desired amount. The primary advantage of the infiltration approach is that the distribution, the geometry, and the chemistry of both the ceramic and metal phases can be altered separately.

5. Stangle, G. C. and I. A. Aksay, "Simultaneous Momentum, Heat and Mass Transfer with Chemical Reaction in a Disordered Porous Medium: Application to Binder Removal from a Ceramic Green Body," *Chem. Eng. Sci.* (submitted, 1989).

A theoretical model has been developed to describe simultaneous momentum and heat and mass transfer phenomena in disordered porous materials. The model can be applied to a wide variety of engineering-related fields, e.g., the drying and/or burnout of processing aids

Abstracts

in the colloidal processing of advanced ceramic materials. Simulations based on the model predict the local temperature and mass distribution of the porous body as a function of time and position. This information can then be coupled with known mechanical properties of the body to preduct internal stresses generated during removal of liquid from the body. The theoretical model has potential applications to many engineering problems, e.g., to optimize processing conditions in the design of an improved binder removal process. The model is evaluated using experimental data on binder removal from a ceramic green compact consisting of submicron α-Al_2O_3 powder disposed in a paraffin wax; the agreement between the simulated and experimental results is good.

6. Stangle, G. C. and I. A. Aksay, "Spinnability Criteria for Ceramic Precursor Fluids," *J. Am. Ceram. Soc.* (to be submitted, 1989).

A theoretical model has been developed that outlines the important parameters involved in the successful fabrication of ceramic fibers from precursor solutions or suspensions. All relevant transport phenomena were described mathematically in the form of continuity equations for fiber components. This information was coupled with the appropriate constitutive relationship for the fluid. A parametric study of process variables was conducted in order to identify and quantify those parameters required for successful ceramic fiber fabrication.